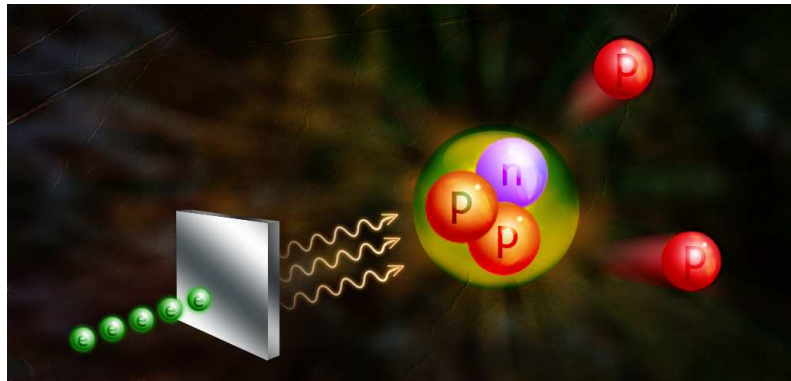


HARD PHOTO-DISINTEGRATION OF PROTON PAIRS IN ^3He
NUCLEI

Thesis submitted towards the degree of
Doctor of Philosophy

By

Ishay Pomerantz



Submitted to the Senate of the Tel Aviv University
September 2011

This work was carried out under the supervision of
Professor Eli Piasetzky

Dedicated to Daphne, by the father who had nothing but protons to bring her from work.

CONTENTS

ACKNOWLEDGMENTS	v
LIST OF TABLES	ix
LIST OF FIGURES	xi
ABSTRACT	xvi
CHAPTER	
1 Introduction	1
1.1 Overview	1
1.2 Photodisintegration of a Nucleon Pair	2
1.3 Dimensional Scaling Rule	3
1.4 Photodisintegration of the Deuteron	5
1.5 Theoretical Approaches	6
1.5.1 The Reduced Nuclear Amplitude (RNA)	6
1.5.2 The Quark-Gluon String Model (QGS)	8
1.5.3 The Hard Rescattering Model (HRM)	9
1.5.4 Theoretical Predictions for the ${}^3\text{He}(\gamma, pp)n$ Reaction	11
2 Experimental Setup	14
2.1 The Electron Beam	14
2.1.1 The Continuous Electron Beam Facility	14
2.1.2 Beam Energy Measurement	15
2.1.3 Beam Position Measurement	17
2.1.4 Beam Current Measurement	17

2.1.5	Beam Rastering System	18
2.2	The Photon Radiator	19
2.3	The Cryogenic Target	20
2.4	The High Resolution Spectrometers (HRSs)	21
2.4.1	Vertical Drift Chambers (VDCs)	23
2.4.2	Scintillators	24
2.4.3	Event triggers	26
2.5	Data Acquisition System	28
3	Data Analysis	30
3.1	Overview	30
3.2	Event Selection	31
3.2.1	Coincidence Between HRS-L and HRS-R	32
3.2.2	Particle Identification	33
3.2.3	Nominal Detection Phase-Space	34
3.2.4	Vertex Position at the Target	36
3.2.5	Kinematic Reconstruction	37
3.3	The Differential Cross Section	39
3.3.1	Calculation of the Laboratory Differential Cross Section	41
3.3.2	Subtraction of the Electro-Production Background	42
3.3.3	Event Simulation Using MCEEP	45
3.3.4	Comparing Data and Simulation	49
3.3.5	Jacobian $\frac{d\Omega_{cm}}{dt}$	50
3.3.6	Jacobian $\frac{d\Omega_{lab}}{d\Omega_{cm}}$	52
3.4	Efficiency Corrections and Experimental Uncertainties	53
3.4.1	Detection Inefficiencies	53
3.4.2	Overview of the Systematic Uncertainties	54

3.4.3	The Uncertainty of the Simulated Acceptance	57
3.4.4	Target Density	58
4	Results	60
4.1	The $\theta_{cm} = 90^\circ$ Differential Cross Section	60
4.2	Comparison with World Data and Theory	61
4.2.1	Low Energy pp Breakup	62
4.2.2	Transition Region	63
4.2.3	Scaling Region	65
4.3	Outlook	66
5	The Two-Body Breakup of ^3He into a Proton-Deuteron Pair	68
5.1	Overview	68
5.2	Experimental Setup and Data analysis	68
5.3	Experiment E93-044 in Hall B	71
5.4	Results and Discussion	74
APPENDIX A		
	Reconstructed photon energy resolution	78
BIBLIOGRAPHY		81

Acknowledgments

It is a pleasure to thank the many people who made this dissertation possible.

It is difficult to overstate my gratitude to my Ph.D. supervisor, Eli Piasetzky. Few of Eli's qualities which I learned to admire were evident from our first meeting: His enthusiasm for his research, his excellent presentation skills and his eye-level attitude to students. I was amazed by the comprehensive sales-presentation that was prepared for me only 24 hours after I first knocked on Eli's door. I came out of that meeting feeling that I understand very little of the subject, but that Eli is a very exciting person to tie my fate with. I thank him for always being willing to meet me whenever I barged into his office, and I'm hoping for many years of future collaboration.

I am indebted to my de-facto co-supervisor, Ron Gilman. I was privileged to become the next link of a long chain of students studying high energy photo-reactions under Ron's supervision. Time after time I found myself spending days trying and miserably failing in finding his intuition wrong. I learned to appreciate Ron's commitment to his students both from his willingness to help advance my personal career, and from his honest feedback to weaknesses in my work.

The two other fathers of the experiment leading to this dissertation are Douglas Higinbotham and Steffen Strauch. I'm in gratitude for Doug's hospitality at my visits to Jefferson lab which greatly eased my way in getting into this new field. Steffen's high standards for good scientific work often balanced my eagerness for advancing too quickly. My special appreciation for his willingness to read proof this dissertation, bringing valuable inputs ranging from profound rational weaknesses to

noting a wrong type of hyphen.

Particular thanks and gratitude go to Yordanka Ilieva whom I enjoyed collaborating with in the past year to combine our two data sets. I'm thankful to Stan Brodsky and Misak Sargsian for the close theoretical guidance they provided, often crossing the line and helping us with the experimental side as well. Further thanks should also go to Shalev Gilad for his guidance and help in making future career choices.

There are many I should thank for the pleasant and productive time I had working at Tel-Aviv University. I am grateful to the administrative and technical support given by Riki Cohen and Moshe Zilka. To the fellow students in our group, Nati Bubis, Or Hen, Igor Korover, Avi Malki and Ran Shneor for pleasant discussions about nuclear physics and everything else.

My special thanks to Guy Ron. Guy's excellent skills as a physicist are evident to anyone who has worked with him, but his kindness and willingness to help a friend was strongly felt when time after time I found myself following in his still-wet footsteps.

Many thanks to Halina Abramovich, Sarah Beck and Cobi Sonnenschein, whom I was privileged to work under as a teaching assistant.

This work could not have been possible without the love and support of my family, which got extended a couple of times during these years. First and foremost to my wife Yael, who've been a wonderful companion to share the path of doctoral studies. She supported, encouraged, understood, shared with me the frustrations and joys of research, loved me at every moment, and I am intellectually indebted to her ideas and our conversations. I will be forever grateful for her brave handling of my long trips abroad, and most of all for having together our daughter Daphne. None of this could have happened without Yael. I owe my greatest gratitude to my parents, Sarit and Itsic, and to my sister and brothers for the support and love that

they have always shown to me. And finally to my daughter Daphne, for motivating me to work harder to finish the day earlier and come home.

LIST OF TABLES

1.1	Values of some kinematic variables for 90° cm angle scattering at two photon energies in the energy range of experiment E03-101.	3
1.2	Scaling of hard exclusive hadronic and nuclear reactions that have been measured to date.	4
2.1	General characteristics of the HRS in Hall A. The horizontal angle is also called the in-plane angle, while the vertical angle is called the out-of-plane angle. The transverse target length is the projection of the target length onto the direction perpendicular to the spectrometer.	22
3.1	Cuts on momentum and angles for the event selection of this analysis.	36
3.2	Photo-production to electro-production ratio.	46
3.3	The calculation steps of the event kinematics in MCEEP.	48
3.4	Absorbances of materials in the HRS and target. Values for these materials are taken from [61]. X is the material's areal density, and λ is the mean free path defined as $\lambda = \frac{\rho}{N_A \sigma}$ where ρ is the density in grams per mole, N_A is Avogadro's number and σ is the cross section for a scattering event to occur.	54
3.5	Total systematic uncertainty in the invariant cross section calculation.	56
4.1	Kinematic settings used for the ${}^3\text{He}(\gamma, pp)n$ measurements. The HRSs were set symmetrically on both sides of the beam with the same central momentum. The values listed for p_{HRS} and θ_{HRS} are the center values of the HRSs acceptance.	60

4.2	The invariant cross section for ${}^3\text{He}(\gamma,pp)n$ at $\theta_{cm} = 90^\circ$. $Y_{\gamma-pp}$ is the yield after electro-disintegration background subtraction. $s^{11} \frac{d\sigma}{dt}$ is scaled with the average value of s for all events in the bin. The uncertainties in $s^{11} \frac{d\Omega_{cm}}{dt}$ are statistical only.	61
5.1	Kinematic settings used for the ${}^3\text{He}(\gamma,pd)$ measurements. The HRSs were set symmetrically on both sides of the beam with equal central momentum settings. The values listed for p_{HRS} and θ_{HRS} are the center values of the HRSs acceptance.	68

LIST OF FIGURES

1.1	In this diagram, two particles come in with momenta p_1 and p_2 , they interact, and then two particles with different momentum (p_3 and p_4) leave. The Mandelstam variables are defined as: $s = (p_1 + p_2)^2 = (p_3 + p_4)^2$, $t = (p_1 - p_3)^2 = (p_2 - p_4)^2$ and $u = (p_1 - p_4)^2 = (p_2 - p_3)^2$.	1
1.2	A typical Feynman diagram for the $\gamma NN \rightarrow NN$ process	3
1.3	Invariant cross section scaled by s^{11} for $d(\gamma,p)n$ taken from previous measurements [9–16] Only the statistical uncertainty is shown. The theoretical curves presented are discussed in the text.	6
1.4	Energy dependence of the predicted $\gamma \text{}^3\text{He} \rightarrow pp + n$ cross section multiplied by s^{11} , compared with the measured energy dependence of the $pp \rightarrow pp$ cross section multiplied by s^{10} and rescaled by an overall constant, to emphasize the similarity in the energy dependences. The horizontal scale is the square of the total c.m. energy (s) for the γpp and pp systems; the photon energy scale is also shown. The different angles for the two reactions are chosen to match the momentum transfers, as discussed in the text. The shaded band is the HRM prediction based on the pp elastic data.	12
1.5	Predictions for $\gamma \text{}^3\text{He} \rightarrow pp + n$ at $\theta_{\text{c.m.}} = 90^\circ$. The horizontal scale is the square of the total c.m. energy (s) for the γpp system; the photon energy scale is also shown. The theoretical curves presented are discussed in the text.	13
2.1	A schematic layout of CEBAF.	15
2.2	Schematics of the CEBAF 12 GeV upgrade.	16
2.3	Schematic layout of the Arc energy measurement system.	17
2.4	The comparison of Tiefenback energy with Arc energy measurement based on data taken from 1999 to 2002. The pass number is the number of times that the electrons were circulated in the accelerator.	18

2.5	Schematic layout of the BCM system in Hall A.	19
2.6	The copper radiator mounted inside the cryotarget cell block. RTD stands for Resistance Temperature Detector.	20
2.7	The racetrack target cell used in the experiment, before installation on the target ladder.	21
2.8	Schematic layout of a HRS device, showing the geometrical configuration of the three quadrupole and the dipole magnets. Distances are indicated in meters. Also shown is the location of the first VDC tracking detector.	23
2.9	Schematic view of the experimental setup for E03-101. Not shown in this drawing are the Cerenkov and lead-glass counters of the HRSs which were not used in this experiment.	24
2.10	Schematic layout of the VDCs in Hall A.	25
2.11	β vs momentum spectrum in HRS-L, the data is taken from the $E_{Beam} = 1.1$ GeV measurement. The top plot displays the spectrum before the TDC offset calibration, the bottom one shows it after.	27
3.1	Schematic of the data analysis work flow.	31
3.2	A typical coincidence time distribution. The time difference between the trigger time of HRS-L and HRS-R is plotted in black for data taken at $E_\gamma = 0.8$ GeV kinematics. The selections cuts are indicated in red.	32
3.3	A typical vertex-z distribution, for events which passed the coincidence time cut. The difference between the reconstructed vertex z coordinate at the target from HRS-L and HRS-R is plotted in black for data taken at $E_\gamma = 0.8$ GeV kinematics. The selections cuts are indicated in red.	33

3.4	A typical β -distributions from HRS-L (top) and HRS-R (bottom) are plotted in black for coincidence events taken at $E_\gamma = 0.8$ GeV kinematics. The coincidence time and vertex-z cuts are specified in Sec. 3.2.1. The two clear peaks are identified as deuterons and protons, as described in the text. The selections cuts set for protons identification are indicated in red. The narrower distribution of HRS-R is due to its better timing resolution which results from the larger number of paddles of smaller size each in its s2m plane	34
3.5	A typical phase space distribution, momentum vs. ϕ (in-plane angle). The spectrum is for the two proton coincidence events. The data are for HRS-R at $E_\gamma = 1.7$ GeV kinematics. The nominal acceptance is indicated in red and the cuts chosen to select events are in blue. . . .	35
3.6	A typical target vertex distribution. The spectrum of the z coordinate of the reconstructed vertex by HRS-L is plotted in black for data taken at $E_\gamma = 0.8$ GeV kinematics. The selections cuts are the central 10 cm of the target indicated in blue. The position of the target walls are indicated in red.	36
3.7	A typical photon energy distribution for two proton coincidence events at beam energy of 1.655 GeV. Solid line represents reconstructed photon energy for the photodisintegration events, dashed line the simulation results. The calculated bremsstrahlung spectrum is shown as a solid blue line. All results are normalized to the measured yield. The cut for photon energy above the 140 MeV pion production threshold is indicated in red.	38
3.8	A typical neutron momentum distribution. The spectrum of the reconstructed neutron momentum for events with two protons in coincidence is plotted in black for data taken at $E_\gamma = 1.7$ GeV kinematics. The selections cut for neutrons with momentum smaller than 100 MeV/c is shown in red.	39
3.9	$\lambda_{\gamma/e}$ (defined in Eq. 3.16) as a function of photon energy. Polynomial fits with 2 and 3 fit parameters are shown with their respective χ^2 . The area between the linear and quadratic fits is shaded.	44
3.10	R_{in}/R_{out} as a function of photon energy.	45
3.11	A block diagram of the simulation Monte-Carlo program "MCEEP". The orange blocks are the subroutines modified for this analysis. . . .	47

3.12	Comparison of various reaction variables - Data (red) vs. Simulation (black). This data set was taken at $E_e=1.7$ GeV kinematics.	50
3.13	Two-body scattering kinematics.	51
3.14	Calculated and measured neutron momentum in ${}^3\text{He}$ distribution. The integral of each distribution up to 100 MeV/c are normalized to 1.	57
3.15	Uncertainty in the target density evaluation. (A) Shows the density as a function of temperature and pressure, and the results of a fit to a quadratic form. (B) Shows a scatter plot of the temperature vs. pressure as recorded for each run. (C) Shows the density calculated for each run according to its pressure and temperature, as a function of the run number. (D) Shows a densities distribution for all runs.	59
4.1	Invariant cross section scaled by s^{11} for ${}^3\text{He}(\gamma,pp)n$. The ${}^3\text{He}(\gamma,pp)n$ events were selected with $p_n < 100$ MeV/c. Up to 2.1 GeV, the photon energy bins are 70 MeV, and above 140 MeV. Only the statistical uncertainties are shown. The preliminary Hall B/CLAS data are taken from [65]. Model predictions are from [29, 66]. RNA is divided by a factor of 200 and QGS by a factor of 5 to be shown on this scale.	62
4.2	The ${}^3\text{He}$ photodisintegration cross sections of a pn pair (upper) and pp pair (lower) [69]. The full line curves are calculation including three-body mechanisms.	63
4.3	A diagram illustration of pp photodisintegration by neutral meson exchange.	64
4.4	$\gamma n \rightarrow \pi^- p$ scaled differential cross section $s^7 \frac{d\sigma}{dt}$ versus center of mass energy \sqrt{s} from [72].	64
5.1	The mass distribution of particles detected in coincidence by the two HRS, normalized by the proton's mass, m_p	69

5.2	Simulated detection acceptance of a proton and a deuteron in coincidence plotted as a function of the photon energy, for $\gamma^3He \rightarrow pd$ and $\gamma^3He \rightarrow pd\pi$. The detector settings and the applied cuts for the analysis are described in the text. The acceptance ratio $\frac{\gamma^3He \rightarrow pd\pi}{\gamma^3He \rightarrow pd}$ is 1.2 %.	71
5.3	Event distributions of the $^3He(\gamma,p)d$ missing-mass reconstructed from the detected proton, MM^2 for proton detected at c.m. angle of 90° with the kinematic cuts (solid blue line), over the background (dashed red line). Events from pd final state are clearly identified as the peak. Accidental and multi-pion events give rise to smooth background under the deuteron peak that can be estimated by the background shape outside of the peak.	73
5.4	The invariant cross section $d\sigma/dt$ multiplied by s^{17} to remove the expected energy dependence. The DAPHNE data is taken from [87].	74

ABSTRACT

Extensive studies of high-energy deuteron photodisintegration over the past two decades have probed the limits of meson-baryon descriptions of nuclei and nuclear reactions. At high energies, photodisintegration cross sections have been shown to scale as a power law in s (the total cm energy squared), which suggests that quarks are the relevant degrees of freedom.

In an attempt to more clearly identify the underlying dynamics at play, JLab/Hall A experiment 03-101 measured the hard photodisintegration of ${}^3\text{He}$ into p-p and p-d pairs at $\theta_{c.m.} = 90^\circ$ and $E_\gamma = 0.8 - 4.7$ GeV. The basic idea is that the measurement should be able to test theoretical predictions for the relative size of pp versus pn disintegrations.

This document presents data for the energy dependence of the high energy 90° c.m. photodisintegration of ${}^3\text{He}$:

$$\frac{d\sigma}{dt}(\gamma + {}^3\text{He} \rightarrow p + p + n_{spectator}),$$

and

$$\frac{d\sigma}{dt}(\gamma + {}^3\text{He} \rightarrow p + d).$$

The cross sections were observed to scale as a function of s^{-n} where n was found to be 11.1 ± 0.1 and 17.4 ± 0.5 for the two reactions respectively. The degree of scaling found for $\frac{d\sigma}{dt}(\gamma + {}^3\text{He} \rightarrow p + d)$ is the highest degree of scaling ever observed in a nuclear process. The onset of the observed scaling are at photon energy of 2.2 GeV for the pp breakup and 0.7 GeV for the pd breakup.

The magnitude of the invariant cross section for pp pair breakup was found to be dramatically lower than for the breakup of pn pairs and theoretical predictions. At energies below the scaling region, the scaled cross section was found to present a strong energy-dependent structure not observed in the pn breakup. The data indicate a transition from three-nucleon hadronic photodisintegration processes at low energies to two-nucleon quark-dominated photodisintegration processes at high energies.

CHAPTER 1

Introduction

1.1 Overview

We define the hard photodisintegration of a nucleon pair as a process in which a high energy photon is absorbed by a nucleon pair leading to pair disintegration into two nucleons with transverse (with respect to the incident photon direction) momenta greater than about 1 GeV/c. In this process the Mandelstam parameters s , $-t$ and $-u$ (see Fig. 1.1) are large. s is the square of the total energy in the c.m. frame, and $t \approx u$, are the four-momentum transfers from the photon to the nucleons. With s above the resonance region, and $-t, -u \geq 1 \text{ GeV}^2$, the kinematics are in the transition region, in which the short distance scales probed might make it appropriate to formulate the theory in terms of quark and gluon rather than hadronic degrees of freedom.

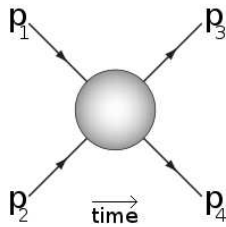


Figure 1.1: In this diagram, two particles come in with momenta p_1 and p_2 , they interact, and then two particles with different momentum (p_3 and p_4) leave. The Mandelstam variables are defined as: $s = (p_1 + p_2)^2 = (p_3 + p_4)^2$, $t = (p_1 - p_3)^2 = (p_2 - p_4)^2$ and $u = (p_1 - p_4)^2 = (p_2 - p_3)^2$.

This chapter describes the motivation for studying hard process in general, and the study of hard pp photo-disintegration in particular. Chapter 2 gives an overview of the experimental setup. Chapter 3 describes how the raw data are processed to calculate the differential cross sections. In chapter 4 we present results for

the ${}^3\text{He}(\gamma,pp)n$, $\theta_{cm} = 90^\circ$ invariant cross sections and discuss their interpretation. Chapter 5 describes an additional reaction channel: the two-body breakup of ${}^3\text{He}$ into a Proton and a Deuteron at $\theta_{cm} = 90^\circ$.

1.2 Photodisintegration of a Nucleon Pair

A common problem in describing quantum mechanical systems is identifying the relevant degrees of freedom needed to efficiently describe the underlying reaction dynamics. Conventional nuclear physics descriptions use meson-baryon degrees of freedom, and it is an ongoing challenge of modern nuclear physics to identify phenomena in which the underlying quark-gluon degrees of freedom are important for their description. Hard two-body processes are natural candidates to reflect the quark substructure of the hadrons and nuclei, since they involve short distance scales.

Disintegrating a nucleon pair at rest using a high-energy photon (E_γ) provides an efficient way to reach the hard regime. s is related to the incident photon energy by

$$s_{\gamma NN} = 4m_N^2 + 4E_\gamma \cdot m_N \approx 4(E_\gamma + 1). \quad (1.1)$$

To obtain the same s in a NN scattering experiment, one needs an incident nucleon energy (E) about a factor of two larger than that of the photon:

$$s_{NN} = 2m_N^2 + 2E \cdot m_N \approx 2(E + 1). \quad (1.2)$$

Table 1.1 lists the values for s , $-t$ and p_T (the transverse momentum) for 90° cm angle scattering as a function of the photon energies, in the range of our experiment.

E_γ (GeV)	s (GeV ²)	$-t$ (GeV ²)	p_T (GeV/c)
2	12	4	1.5
5	24	10	2.5

Table 1.1: Values of some kinematic variables for 90° cm angle scattering at two photon energies in the energy range of experiment E03-101.

1.3 Dimensional Scaling Rule

The dimensional scaling rule (also called constituent counting rule) states that

$$\frac{d\sigma}{dt}_{AB \rightarrow CD} \sim s^{-(n-2)} f(\theta_{cm}) \quad (1.3)$$

for exclusive reactions at the $s \rightarrow \infty$ limit. Here n is the total number of elementary fields (quarks, leptons or photons) which carry finite fractions of momentum. It predicts a scaling behavior of cross sections and form factors at fixed center-of-mass angle θ_{cm} and large s .

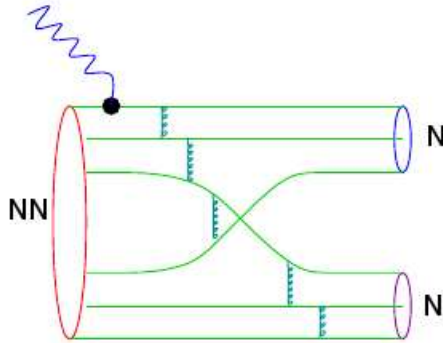


Figure 1.2: A typical Feynman diagram for the $\gamma NN \rightarrow NN$ process

The dimensional scaling rule was originally derived from simple dimensional counting by Brodsky and Farrar [1], and simultaneously by Matveev et. al. [2] in 1973. We will take the Brodsky and Farrar approach for NN photodisintegra-

tion process $\gamma NN \rightarrow NN$. Assuming that the process is dominated by the Feynman diagrams similar to Fig. 1.2, the dimension of the invariant amplitude can be counted by using Feynman's rules and the normalization of the spinors $u^\dagger u = 2E$. Each external fermion line contributes a dimension of energy $E^{\frac{1}{2}}$ to the invariant amplitude, while each external boson line contributes a dimension of E^0 . A fermion propagator contributes a dimension of E^{-1} , while a boson propagator contributes a dimension of E^{-2} . So the dimension of the invariant amplitude M is $(E^{\frac{1}{2}})^{12} \cdot (E^0)^1 \cdot (E^{-1})^5 \cdot (E^{-2})^5 = E^{-9}$. If the only energy at large s and fixed θ_{cm} is the center-of-mass energy \sqrt{s} , then $M \sim s^{-9/2}$ and $(d\sigma/dt)_{\gamma NN \rightarrow NN} \sim s^{-2} M^2 \sim s^{-11}$. This result is in agreement with Eq. 1.3: the total number of elementary fields in the initial and final state is $n = 13$ (1(photon) + 6(deuteron) + 3(N) +3(N)) and thus $-(n - 2) = -11$.

Reaction	s GeV ²	$\theta_{c.m.}$ deg.	n Predicted	n Measured	Reference
$pp \rightarrow pp$	15-60	38-90	-10	-9.7 ± 0.5	[3]
$p\pi^- \rightarrow p\pi^-$	14-19	90	-8	-8.3 ± 0.3	[4]
$\gamma p \rightarrow \gamma p$	7-12	70-120	-6	-8.2 ± 0.5	[5]
$\gamma p \rightarrow \rho^0 p$	6-10	80-120	-7	-7.9 ± 0.3	[6]
$\gamma p \rightarrow p\pi^0$	8-10	90	-7	-7.6 ± 0.7	[7]
$\gamma p \rightarrow n\pi^+$	1-20	90	-7	-7.3 ± 0.4	[8]
$\gamma d \rightarrow pn$	1-4	50-90	-11	-11.1 ± 0.3	[9-16]
$\gamma pp \rightarrow pp$	2-5	90	-11	-11.1 ± 0.1	[17] (this work)
$\gamma^3 He \rightarrow pd$	11-15.5	90	-17	-17.4 ± 0.5	[18] (this work)

Table 1.2: Scaling of hard exclusive hadronic and nuclear reactions that have been measured to date.

Currently, there is a strong experimental evidence for the success of the scaling laws (see Table 1.2 for a list of exclusive reactions that have been measured to date). However, the interpretation of the observed scaling has stirred a lot of controversy which, despite more than 30 years of efforts, is not yet settled. The controversy arises from the fact that the scaling laws, being derived from pQCD [1], are naturally expected to be valid in the dynamical regime of pQCD. However, the data show

evidence for dimensional scaling at momentum transfers as low as $1 \text{ (GeV}/c)^2$. At such low momentum transfers, other tests of pQCD predictions, such as hadron-helicity conservation failed.

The good agreement of the data with the prediction of dimensional scaling contrasts with observations [19–21] that pQCD dramatically underestimates cross sections for intermediate energy photo-reactions – examples include the deuteron elastic form factor [22], meson photoproduction [23] and real Compton scattering [24]. Thus, it seems that although the observation of the scaling in a given reaction indicates the onset of the quark-gluon degrees of freedom, the appropriate underlying physics has a mixture of perturbative and nonperturbative QCD aspects. The question then arises: If dimensional scaling cannot be interpreted as evidence for applicability of pQCD, how else can it be interpreted at such low energies? The controversy in the meaning of experimentally observed scaling has been difficult to resolve due to the complexity of the non-perturbative reaction dynamics at such low momentum transfers and the difficulties modeling it which vary from process to process. To date there is no common model or a theory that can describe all the data listed in Table 1.2 in a consistent manner.

1.4 Photodisintegration of the Deuteron

Deuteron photodisintegration cross sections were measured for photon energies up to 5 GeV (but only 4 GeV at $\theta_{\text{c.m.}} = 90^\circ$) [9–13, 15] For energies up to 2.5 GeV, “complete” angular distributions [14, 16] and proton recoil polarizations [25] were also measured. Fig. 1.3 shows the measured energy dependence of $s^{11} \frac{d\sigma}{dt}$ for 90° c.m. The dimensional scaling prediction [1, 26, 27], that this quantity becomes independent of energy, is observed clearly. High-energy deuteron photodisintegration cross sections at other angles are also in good agreement with scaling once $p_T \geq 1.3 \text{ GeV}/c$.

A variety of theoretical models exists for deuteron photodisintegration which explicitly account for quark-gluon degrees of freedom in the reaction with an attempt to incorporate nonperturbative QCD effects.¹

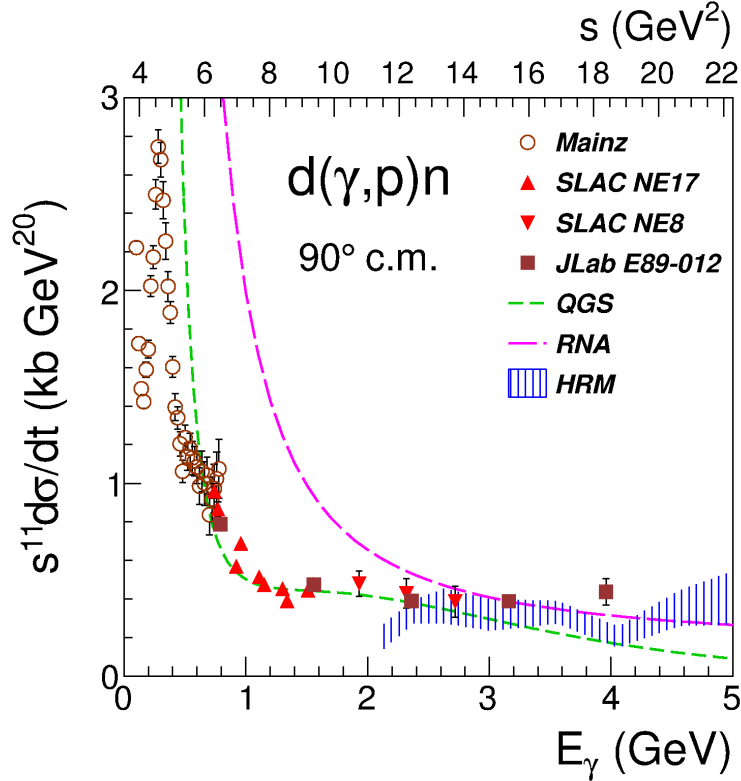


Figure 1.3: Invariant cross section scaled by s^{11} for $d(\gamma,p)n$ taken from previous measurements [9–16]. Only the statistical uncertainty is shown. The theoretical curves presented are discussed in the text.

1.5 Theoretical Approaches

1.5.1 The Reduced Nuclear Amplitude (RNA)

The reduced nuclear amplitude (RNA) formalism [29, 30] attempts to incorporate some of the soft physics not described by pQCD by using experimentally determined nucleon form factors to describe the gluon exchanges within the nucleons. It neglects diagrams in which gluon exchanges between the nucleons lead to

¹Note that to date there are no successful meson-baryon calculations for the high energy data. See review [28].

non-color singlet intermediate “nucleon” states, diagrams which might be important in pQCD calculations. The RNA calculation should be normalized to the cross section scaling behavior at asymptotic energies. In practice, it is normalized to the data at the highest available energy. An estimate of the minimal photon lab energy in which this model is valid is obtained by requiring the momentum transfer to each nucleon to be above 1 GeV/c, which yields [31]

$$\frac{1}{2}M_d E_\gamma \left[1 - \sqrt{\frac{2E_\gamma}{M_d + 2E_\gamma} |\cos \theta_{\text{c.m.}}|} \right] \geq 1 \text{ GeV}^2. \quad (1.4)$$

The minimal energy requirement is at 90° , where $E_\gamma \geq 1 \text{ GeV}$.

In the RNA approach [29,30], the differential cross section is proportional to the squares of form factors, one for each nucleon, evaluated at the momentum transfer for that nucleon in the weak-binding limit. The remainder, the “reduced” cross section, is assumed to be independent of the substructure of the nucleons. This gives

$$\frac{d\sigma}{dt} \simeq F_{N_1}^2(-t_1) F_{N_2}^2(-t_2) \left. \frac{d\sigma}{dt} \right|_{\text{reduced}}, \quad (1.5)$$

for the process $\gamma(N_1 N_2) \rightarrow N_1 N_2$, where t_i is the square of the four-momentum transfer to nucleon N_i . The ratio of cross sections for $\gamma(pp) \rightarrow pp$ and $\gamma(pn) \rightarrow pn$ is then given by the ratio of nucleon form factors squared, $F_p^2(-t_N)/F_n^2(-t_N)$ ($t_N \approx \frac{t}{2}$), times the ratio of the reduced cross sections. The ratio of form factors can be obtained from data for G_M and G_E [32]; we use the leading twist form factor F_1 for each nucleon, for which the ratio F_{1p}/F_{1n} is approximately -2. The ratio of reduced cross sections is taken to be 4, the square of the charge ratio. These estimations yield $\gamma(pp) \rightarrow pp$ cross section approximately 16 times larger than the RNA prediction for $\gamma d \rightarrow pn$ cross section. The absolute normalization for the $\sigma_{RNA}(\gamma(pp) \rightarrow pp)$ can be obtained from comparison of $\sigma_{RNA}(\gamma d \rightarrow pn)$ with available data.

To estimate the cross section of $\gamma \text{}^3\text{He} \rightarrow pp + n$ with a spectator neutron, we multiply the above cross section $\sigma_{RNA}(\gamma(pp) \rightarrow pp)$, with the probability of finding

a correlated pp pair and a low momentum neutron in the ${}^3\text{He}$ wave function. Note that no new normalization to the experimental data is needed, since we use the normalization factors obtained from the comparison of the $\sigma_{RNA}(\gamma d \rightarrow pn)$ cross sections with the data.

To estimate this factor we observe that in RNA the amplitude results from the pp wave function at small separations. Therefore, as a simple estimate, we use the parameter $a_2(A)$ which characterizes the probability of two-nucleon correlations in the nuclear wave function – $a_2(A = 3) \approx 2$ [33, 34] – multiplied by $1/3$, which accounts for the relative abundance of pp pairs in the two-nucleon short-range correlation. The integration of the neutron momentum up to $100 \text{ MeV}/c$ leads to an additional factor of $1/2$. Thus, these estimations yield an overall factor of $\approx 1/3$ by which $\sigma(\gamma(pp) \rightarrow pp)$ should be scaled in order for it to correspond to the $\gamma {}^3\text{He} \rightarrow pp + n$ cross section. The overall factor of $1/3$ is a conservative estimate; the inclusion of three-nucleon correlations in ${}^3\text{He}$ would increase this factor. Thus, in the RNA approach, $d\sigma(\gamma {}^3\text{He} \rightarrow pp + n) / d\sigma(\gamma d \rightarrow pn) \approx 16/3$.

1.5.2 The Quark-Gluon String Model (QGS)

The quark-gluon string model (QGS) [35] views the reaction as proceeding through three-quark exchange, with an arbitrary number of gluon exchanges. The cross section is evaluated using Regge theory techniques, and is sensitive to the Regge trajectory used. While Regge theory has been shown to be an efficient description of high-energy, small- t reactions, it has not typically been applied to the large momentum transfers being discussed here. The best fit of the data is obtained in a calculation that uses a nonlinear trajectory, as opposed to the more familiar linear trajectory.

Since the Regge trajectories for $\sigma(\gamma(pn) \rightarrow pn)$ and $\sigma(\gamma(pp) \rightarrow pp)$ are similar, the QGS model predicts that the cross sections are of similar magnitude [29]. We

assume that this is multiplied by the same ^3He correction factor of 1/3 that apply to the RNA model.

1.5.3 The Hard Rescattering Model (HRM)

The QCD hard rescattering model (HRM) [36] assumes that the photon is absorbed by a quark in one nucleon, followed by a high momentum transfer interaction with a quark in the other nucleon leading to high relative momentum between the two nucleons. Summing the relevant quark rescattering diagrams demonstrates that the nuclear scattering amplitude can be expressed as a convolution of the large angle pn scattering amplitude, the hard photon-quark interaction vertex and the low-momentum nuclear wave function. Since the pn hard scattering amplitude can be taken from large angle pn scattering data, the HRM model allows calculation of the absolute cross section of the $\gamma d \rightarrow pn$ reactions using no adjustable parameters.

The $\gamma^3\text{He} \rightarrow pp + n$ differential cross section within the HRM model is [37]:

$$\frac{d\sigma}{dt d^3p_n} = \left(\frac{14}{15}\right)^2 \frac{8\pi^4 \alpha_{EM}}{s - M_{^3\text{He}}^2} \frac{d\sigma^{pp}(s_{pp}, t_N)}{dt} \times \frac{1}{2} \left| \sum_{spins} \int \Psi^{^3\text{He}}(p_1, p_2, p_n) \sqrt{M_N} \frac{d^2 p_{2T}}{(2\pi)^2} \right|^2, \quad (1.6)$$

where $s = (P_\gamma + P_{^3\text{He}})^2$, $t = (P_p - P_\gamma)^2$, $s_{pp} = (P_\gamma + P_{^3\text{He}} - P_n)^2$, and $t_N \approx \frac{1}{2}t$. The pp elastic cross section is $d\sigma^{pp}/dt$. The momentum of the recoil neutron is p_n . In the argument of the ^3He nuclear wave function, $\vec{p}_1 = -\vec{p}_2 - \vec{p}_n$ and $p_{1z} \approx p_{2z} \approx -\frac{p_{nz}}{2}$ near $\theta_{c.m.} = 90^\circ$. The pp scattering cross section was obtained from a fit to the existing pp data [38]. The overall factor $(\frac{14}{15})$ is obtained using the quark-interchange model of hard NN scattering with $SU(6)$ wave function of the nucleons, which introduces an uncertainty in the estimates of the cross section at the level of 10 – 20%. The ^3He wave function is that of Ref. [33], obtained by solving the Faddeev equation with a realistic NN potential. The predicted single differential cross section is obtained by integrating over neutron momentum, up to 100 MeV/c.

The possibility that the final-state high- p_T proton pair is formed due to the hard interaction of the two outgoing protons should produce oscillations in the energy dependence of the invariant cross section, as observed in the pp cross section [3]. The quark counting rule predicts $\frac{d\sigma}{dt} \sim s^{-10}$ for high-energy, large-angle $pp \rightarrow pp$ elastic scattering. The pp elastic cross sections are globally consistent over many orders of magnitude with this power law [38, 39]. However, it was already noted in 1974 [3] that a more detailed examination of the data indicated significant deviations from scaling. The deviations are known as “oscillations” and were interpreted as resulting from interference between the pQCD amplitude and an additional nonperturbative component.

Ralston and Pire [40] suggested that the interference is between a small size configuration pQCD scattering and an independent scattering of **all** valence quarks (discussed by Landshoff [41]) governed by the so-called chromo-Coulomb phase. Brodsky and deTera mond [42] suggested that the oscillations are due to the presence of two broad resonances (or threshold enhancements) which interfere with the standard pQCD amplitude. For a review of wide-angle processes, see [43].

Whatever is the correct interpretation of the oscillation, if the hard two-body break-up reaction proceeds through the hard interaction of two protons, similar oscillations could be seen in the $\gamma \ ^3\text{He} \rightarrow pp + n$ cross section, normalized by a factor of s^{11} , as a function of the incident photon energy, in the same region of s where pp oscillations are observed. Fig. 1.4 compares the energy dependence of pp cross section with that of $\gamma \ ^3\text{He} \rightarrow pp + n$ cross section at $90^\circ \ \gamma - (pp)$ center of mass scattering ($-\frac{t}{s_{pp}} \approx \frac{1}{2}$), calculated within the HRM model, which assumes the dominance of the contribution of hard pp rescattering in the photodisintegration reaction. Note that according to Eq.(1.6) the pp cross section that enters in the $\gamma + \ ^3\text{He} \rightarrow pp + n$ cross section is defined at s_{pp} and $t_N \approx \frac{t}{2}$. As a result, in Fig. 1.4 one compares with pp cross sections defined at $\approx 60^\circ$ ($-\frac{t_N}{s} \approx \frac{1}{4}$) [38]. In contrast to

the situation displayed in Fig. 1.4, the precision of the pn and the $\gamma d \rightarrow pn$ data is insufficient to show if oscillations are indeed present for those reactions.

1.5.4 Theoretical Predictions for the ${}^3\text{He}(\gamma, pp)n$ Reaction

Fig. 1.5 shows predictions based on the models considered above for 90° two-body break-up kinematics. The $\gamma {}^3\text{He} \rightarrow pp + n$ cross section has been integrated over the neutron momentum up to 100 MeV/c.

It is important to note that the models considered above predict a sizable cross section for the break up of the pp pair, larger than that for the pn pair, for two of the three models shown. This prediction is rather striking since at low energies the photodisintegration of the pp system is suppressed as compared to pn [44].

Within a mesonic description of the interaction, the 90° break up of a pp pair will be significantly suppressed as compared to pn since for the pp pair the exchanged mesons are neutral and do not couple to the photon. In a quark-gluon picture, the exchanged particles are quarks, and the suppression will be absent. As a result an experimental observation of a larger cross section for the pp break-up reaction can be an indication of the quark-gluon dynamics dominance in the reaction. These theoretical predictions are compared to the measurements in Chapter 4.

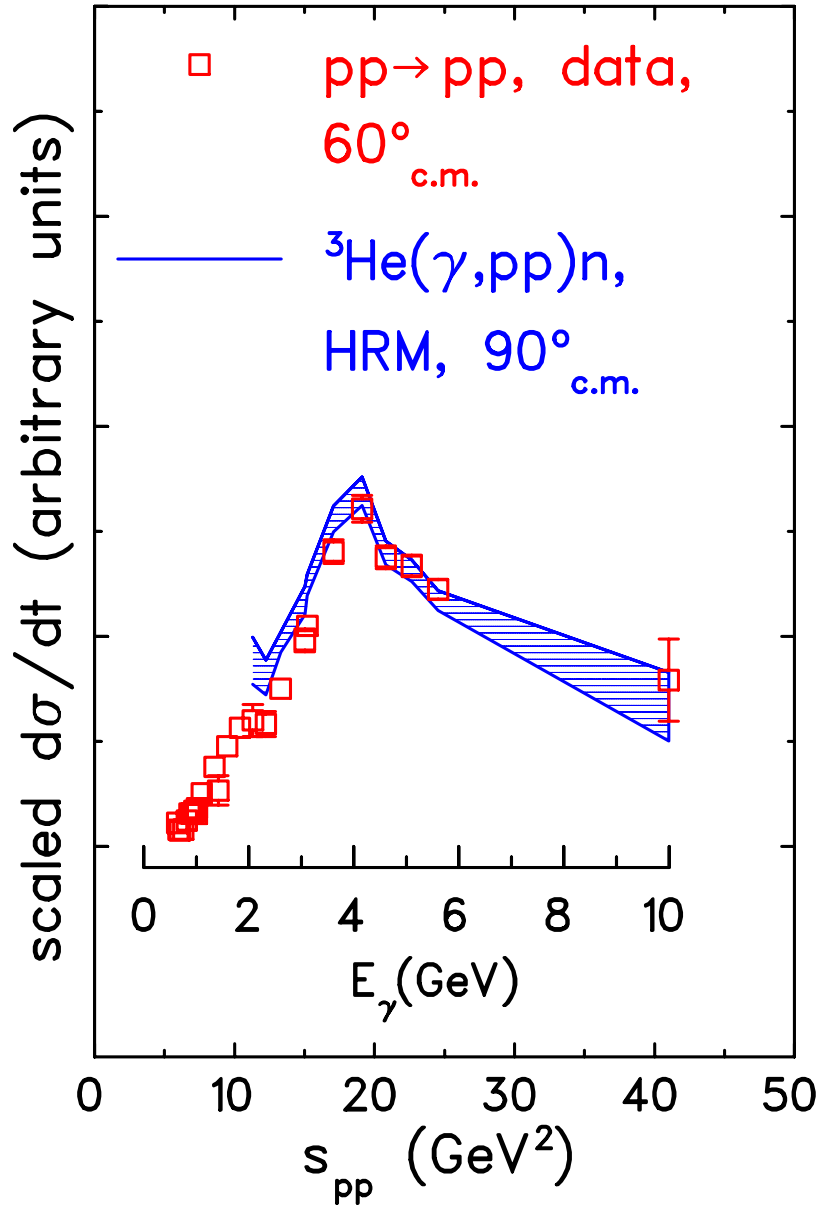


Figure 1.4: Energy dependence of the predicted γ ${}^3\text{He} \rightarrow pp + n$ cross section multiplied by s^{11} , compared with the measured energy dependence of the $pp \rightarrow pp$ cross section multiplied by s^{10} and rescaled by an overall constant, to emphasize the similarity in the energy dependences. The horizontal scale is the square of the total c.m. energy (s) for the γpp and pp systems; the photon energy scale is also shown. The different angles for the two reactions are chosen to match the momentum transfers, as discussed in the text. The shaded band is the HRM prediction based on the pp elastic data.

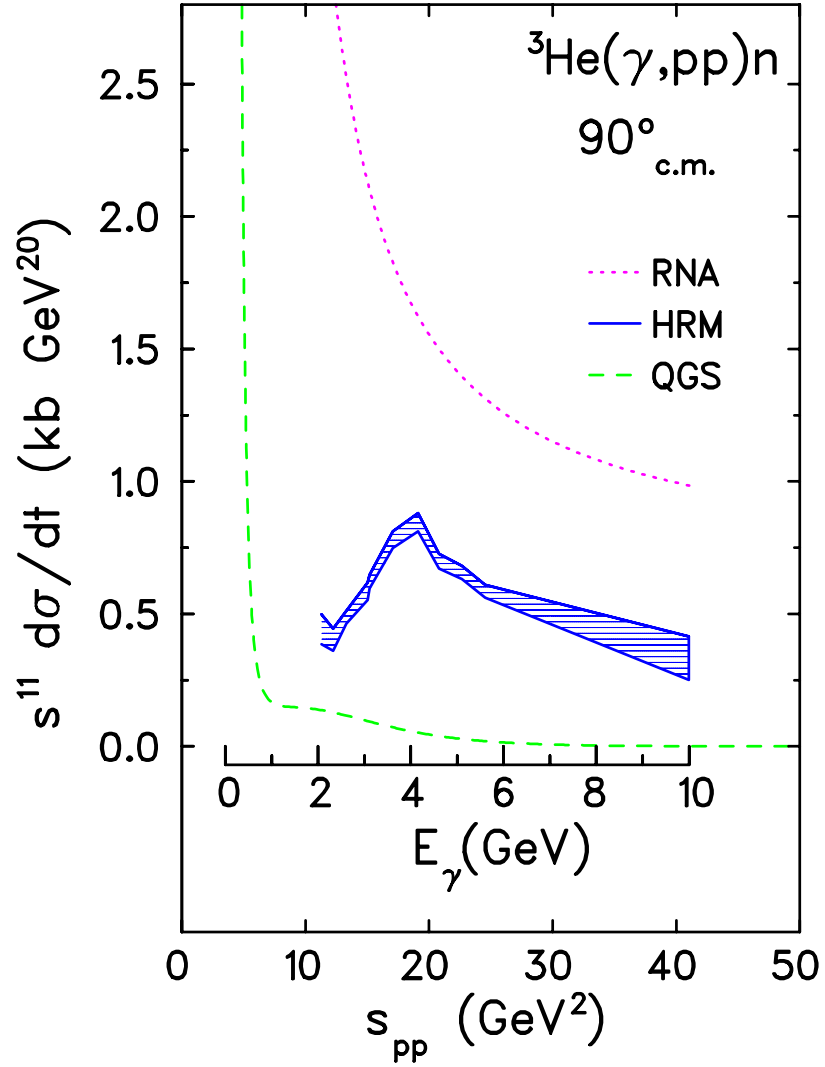


Figure 1.5: Predictions for $\gamma {}^3\text{He} \rightarrow pp + n$ at $\theta_{\text{c.m.}} = 90^\circ$. The horizontal scale is the square of the total c.m. energy (s) for the γpp system; the photon energy scale is also shown. The theoretical curves presented are discussed in the text.

CHAPTER 2

Experimental Setup

2.1 The Electron Beam

2.1.1 The Continuous Electron Beam Facility

JLab's Continuous Electron Beam Accelerator Facility (CEBAF) provide multi-GeV polarized electron beams. As a user facility for scientists worldwide, the primary mission of JLab is to conduct basic research that builds a comprehensive understanding of nuclei and nucleons. JLab also conducts applied research based on the technology developed for physics experiments, such as the Free Electron Laser (FEL) project.

CEBAF is the first large-scale application of superconducting radio-frequency electron accelerating technology. It can deliver a high-quality, continuous, polarized ($>75\%$) electron beam with currents up to $200 \mu\text{A}$ and energy up to 6 GeV. It consists of a pair of anti-parallel superconducting linacs connected by two 180° bending arcs with a radius of 80 meters, in a racetrack shape shown in Fig. 2.1 [45].

Three interlaced 499 MHz electron beams are injected from a state-of-the-art photocathode gun system that is capable of delivering beams of high polarization and high currents to Hall A and Hall C ($1 - 150 \mu\text{A}$) while maintaining the high polarization and low current beam to Hall B ($1-100 \text{ nA}$). Each linac consists of a series of 20 cryomodules or 160 superconducting radio-frequency niobium cavities with 2 K helium coolant. Each niobium cavity contains the electric field that accelerates the electrons. The electrons can be circulated up to five times in the accelerator, gaining up to 1.2 GeV for each pass.

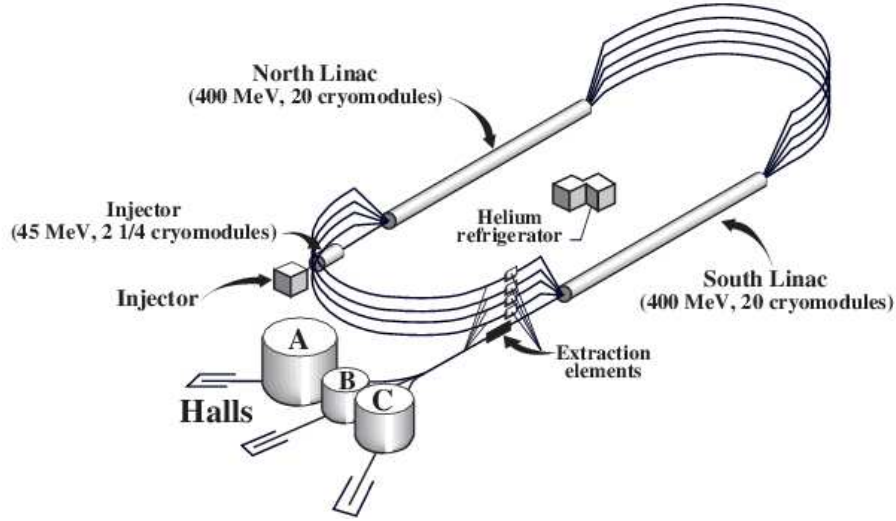


Figure 2.1: A schematic layout of CEBAF.

Jefferson lab is currently undergoing a major upgrade which will double the beam energy. The major changes of this upgrade are illustrated in Fig 2.2. For the upgrade, a new hall (Hall D) will be built at the end of the accelerator opposite the present Halls A, B and C. There, experimenters will use collimated beams of linearly polarized photons at 8-9 GeV, produced by coherent bremsstrahlung from 12.1 GeV electrons. To send a beam of that energy to that location requires a sixth acceleration pass through one of the linacs. This means adding a recirculation beamline to one of the arcs, and also requires augmenting the accelerator's present 20 cryomodules with 10 new, higher-performing ones. Maximum energy for five passes will rise to 11 GeV for the three original halls, with experimental equipment upgraded in each. The 2 K helium refrigeration plant will be upgraded to 10.1 kW from the present 4.8 kW.

2.1.2 Beam Energy Measurement

The Arc energy measurement determines the beam momentum p from the bend angle θ of the electrons and the integral of the magnetic field $\int Bdl$ in the arc section

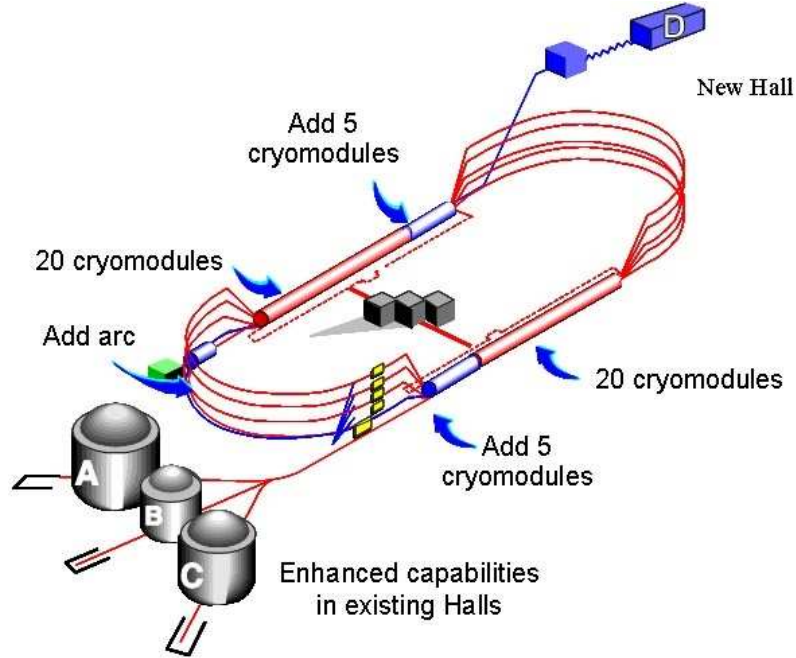


Figure 2.2: Schematics of the CEBAF 12 GeV upgrade.

of the beam line, according to [46]

$$p = k \frac{\int Bdl}{\theta} \quad (2.1)$$

where $k = 0.2999792 \text{ GeV rad T}^{-1} \text{ m}^{-1}/c$. The bend angle is obtained by measuring the beam positions at the entrance and exit of the arc with four wire scanners (SuperHarps), as shown in Fig.2.3 [47]. The magnetic field integral measurement is determined by measuring the field of a reference magnet, powered in series with the eight dipoles in the arc vacuum that are inaccessible to a field measurement.

The beam energy can be determined from the Arc integral measurement alone by assuming the nominal bend angle of 34.2918° . The Arc integral measurement can be used as an approximation to the Arc energy measurement when the beam position measurement in the dispersive mode is not available.

The beam energy can also be determined from the current value of the field integral and the nominal bend angle, which is called the Tiefenback energy. The Tiefenback energy is written into the data stream for each run. As shown in Fig.2.4

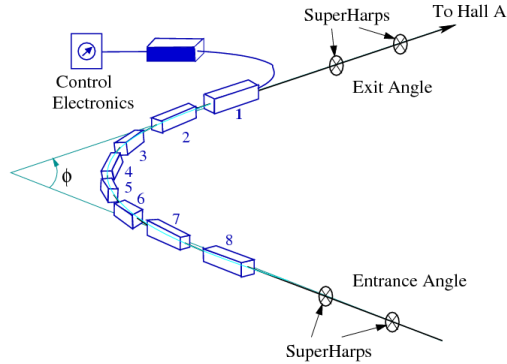


Figure 2.3: Schematic layout of the Arc energy measurement system.

[48], Tiefenback energy agrees with Arc energy measurement with the uncertainty of 0.05% for beam energy above 1 GeV.

2.1.3 Beam Position Measurement

Two beam position monitors (BPMs), 7.516 m and 2.378 m upstream from the target, are used to determine the position and direction of the beam on the target. Each BPM is a cavity with a 4-wire antenna in one plane tuned to the RF frequency of the beam (1497 MHz). The standard difference-over-sum technique is used to compare the distances of the beam to the wires and hence determine the beam position in the plane. The combination of two BPMs gives the direction of the beam. The BPM measurement is non-destructive and can be used to monitor the beam continuously. The average of the beam position from the BPMs integrated over 0.3 second is injected into the data stream every few seconds.

2.1.4 Beam Current Measurement

The beam current is measured by two beam current monitors (BCMs), schematically shown in Fig. 2.5 [49]. The BCMs, cylindrical waveguides tuned to the frequency of the beam (1497 MHz), are used to continuously monitor the beam. When the electron beam passes, it excites the resonant transverse magnetic mode TM_{010} .

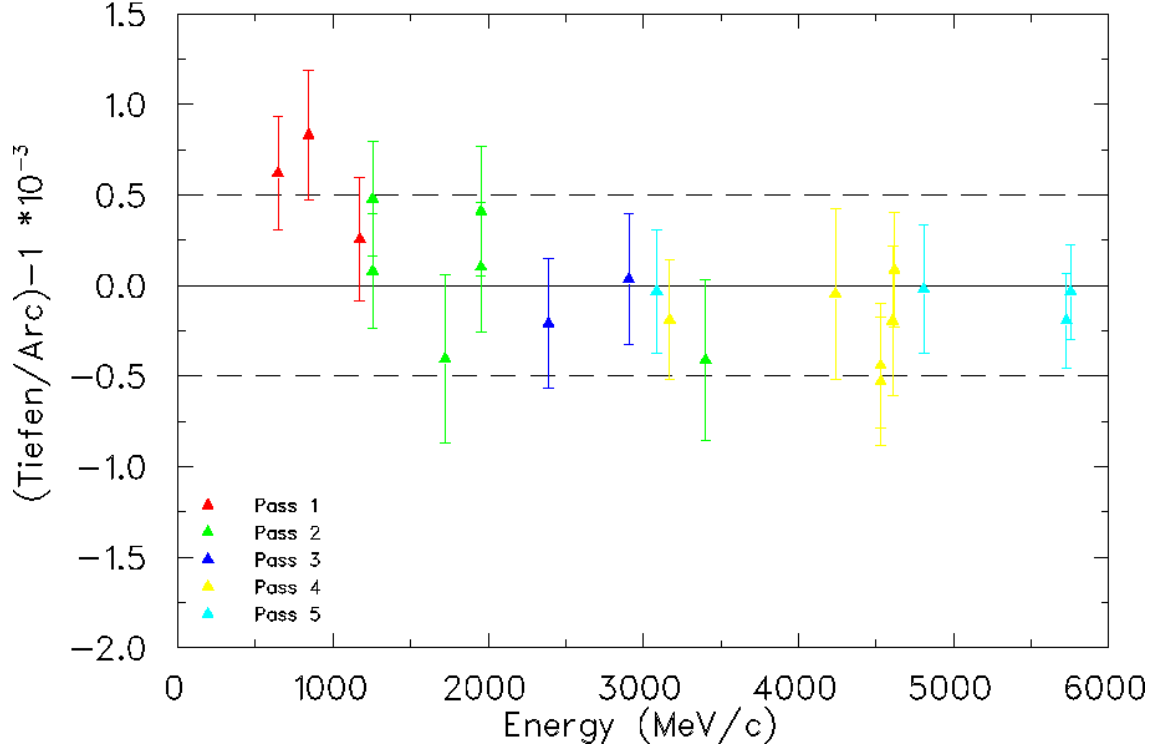


Figure 2.4: The comparison of Tiefenback energy with Arc energy measurement based on data taken from 1999 to 2002. The pass number is the number of times that the electrons were circulated in the accelerator.

The BCM output, proportional to the beam current, undergoes a series of digital conversions described in [46]. until finally the signal is fed into a scaler, who's reading is proportional to the integrated charge.

2.1.5 Beam Rastering System

The size of the beam at the target is typically a few hundred micrometers in both horizontal and vertical directions. To prevent the target from being overheated locally, a beam raster is used for beam currents greater than several microamperes.

The raster in Hall A is driven by a pair of horizontal and vertical aircore dipoles located 23 meters upstream of the target. Both rectangular and circular patterns can be generated. The rectangular pattern, with a typical dimension of 2.5 mm \times 2.5 mm (at the target), was used for beam rastering in experiment E03-101.

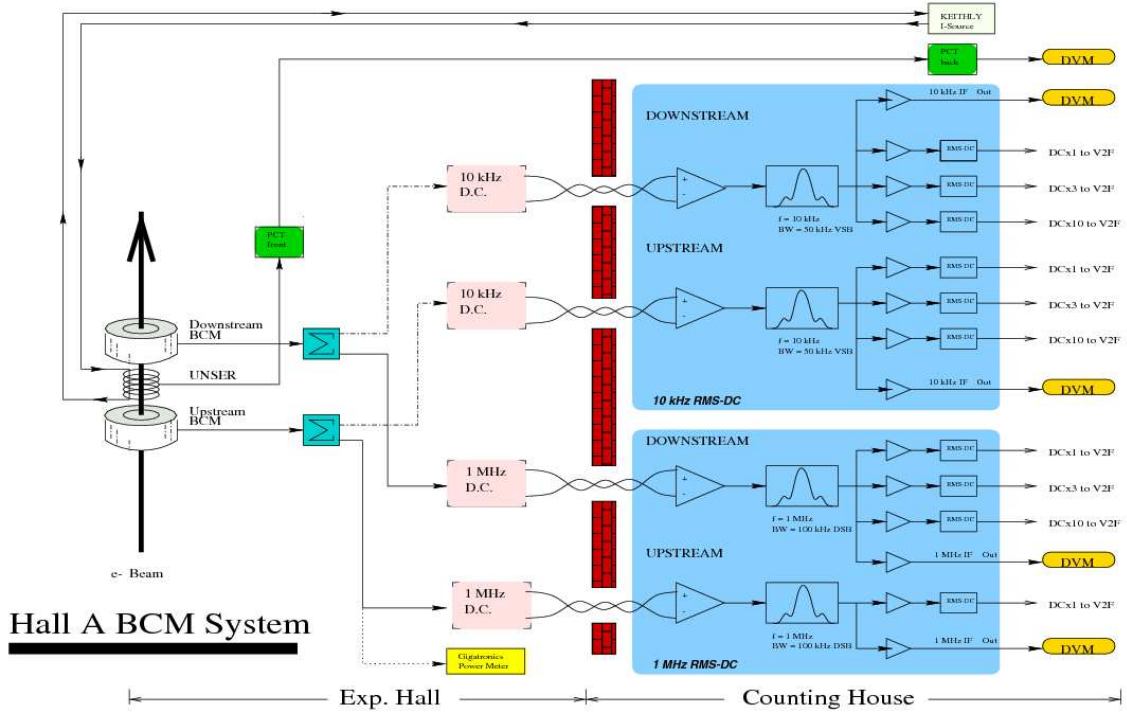


Figure 2.5: Schematic layout of the BCM system in Hall A.

2.2 The Photon Radiator

The untagged real photon beam is generated by electrons impinging on a copper bremsstrahlung radiator [50], which was mounted inside the cryotarget cell block (see Fig. 2.6), about 15 cm upstream of the center of the target. The photon energy is determined by kinematical reconstruction (described in Sec. 3.2.5) and the photon yield is determined based on theoretical calculations (see Sec. 3.3.3). The electrodisintegration background is measured with the radiator removed from the beam (described in Sec. 3.3.2). The photon radiator in Hall A was previously used for deuteron photodisintegration [51] and pion photoproduction experiments [13].

The photon radiator is a U-shaped ladder with six available positions to mount foils. One position was empty, and the remaining five were occupied by copper foils of different thickness, i.e. 2.04%, 3.06%, 4.08%, 5.10% and 6.12% of a radiation length. Each foil is 6.35 cm wide and 3.175 cm high. The 6.12% foil, which is \sim

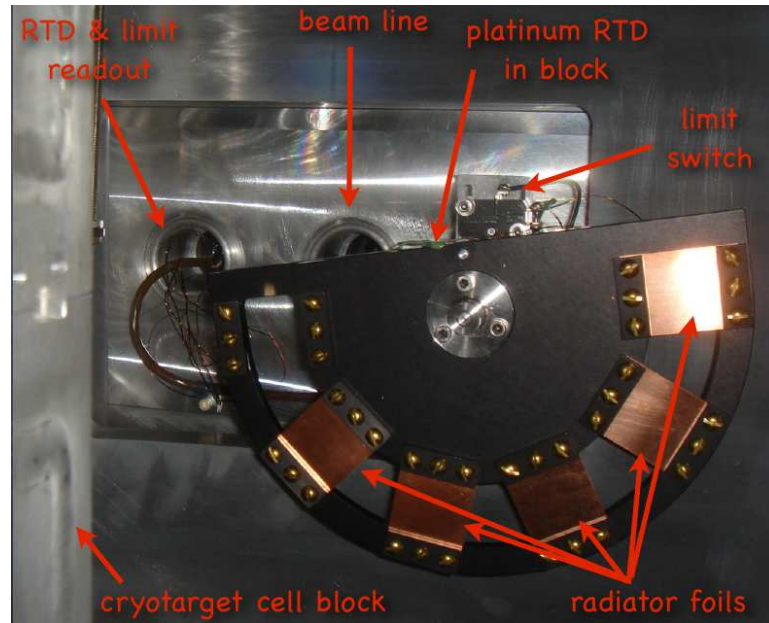


Figure 2.6: The copper radiator mounted inside the cryotarget cell block. RTD stands for Resistance Temperature Detector.

1 mm thick, was used for the production data of E03-101. The foils were directly cooled by the cryotarget.

2.3 The Cryogenic Target

The cryogenic target system [46] is mounted inside the scattering chamber at the center of the hall. To reduce the amount of detected events which originates from the target's walls, a 20 cm long “racetrack” shaped cell was used as the primary ^3He target for the experiment. The target cell, shown in Fig. 2.7, is made of Al and is 2 cm in diameter. The sidewalls of the cell are $137\ \mu\text{m}$ thick with entrance and exit windows $178\ \mu\text{m}$ and $71\ \mu\text{m}$ thick respectively. The target cell was mounted on the Hall A target ladder assembly inside an evacuated ($\sim 10^{-6}$ Torr) scattering chamber.

The Hall A target ladder assembly consists of three cryogenic loops and several solid targets used for optics and background measurements. For E03-101, only loop 1 was used, installed with the racetrack target, and supplied with ^3He gas

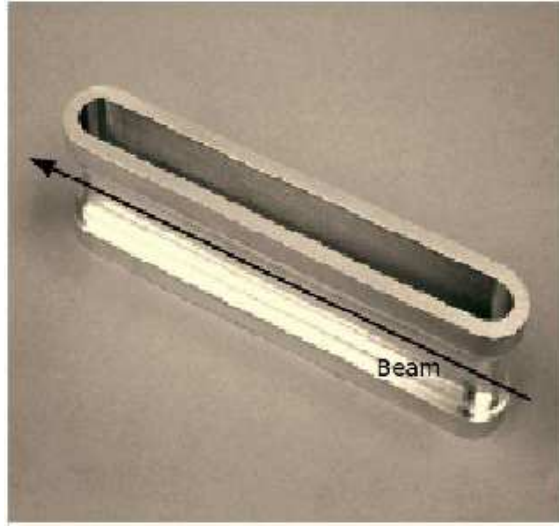


Figure 2.7: The racetrack target cell used in the experiment, before installation on the target ladder.

at a temperature of ~ 7 K and pressure of ~ 25 psi, giving target density of ~ 0.079 g/cm³ (see sec. 3.4.4 for exact target density evaluation procedure).

2.4 The High Resolution Spectrometers (HRSs)

The core of the hall A equipment is a pair of nearly identical 4 GeV/c spectrometers capable of determining the momentum and angles of charged particles with high resolution. The general characteristics are summarized in Tab. 2.1 [46, 52].

The configuration of the superconducting magnet system is QQD_nQ (Q:quadrupole; D:dipole) with a vertical bend, as shown in Fig. 2.8 [46]. The dipole magnet includes additional focusing from a field gradient, n , which simplifies the overall design of the spectrometer. The vertical bend decouples, to first order, the reconstruction of vertex position along the target from that of the momentum reconstruction. The quadrupole after the dipole makes it possible to have reasonably good horizontal position and angular resolution simultaneously. The bend angle of 45° is a compromise between cost and performance. The magnetic fields in both dipoles are measured continuously with two arrays of three NMR field probes to the precision of 10⁻⁵.

Magnet Configuration	QQD _n Q
Bend Angle	45° vertical
Optical Length	23.4 m
Momentum Range for the Left Spectrometer	0.3 ~ 4.0 GeV/c
Momentum Range for the Right Spectrometer	0.3 ~ 3.16 GeV/c
Momentum Acceptance	± 4.5%
Momentum Resolution	1 × 10 ⁻⁴
Scattering Angular Range	12.5° ~ 165°
Horizontal Angular Acceptance	± 30 mr
Vertical Angular Acceptance	± 60 mr
Horizontal Angular Resolution (FWHM)	± 0.5 mr
Vertical Angular Resolution (FWHM)	± 1.0 mr
Solid Angle	~ 6 msr
Transverse Target Length Acceptance	± 50 mm
Transverse Position Accuracy	± 0.3 mm
Transverse Position Resolution (FWHM)	4.0 mm

Table 2.1: General characteristics of the HRS in Hall A. The horizontal angle is also called the in-plane angle, while the vertical angle is called the out-of-plane angle. The transverse target length is the projection of the target length onto the direction perpendicular to the spectrometer.

The magnetic fields of the quadrupoles are monitored using Hall probes that are not very stable and reproducible over a long term, so the fields of the quadrupoles are set by their currents. Due to hysteresis effects, the quadrupoles Q2 and Q3 require cycling when their momenta are raised, staying at a maximum current for a few minutes before being set to the desired value. The hysteresis effect of Q1 and dipole is so small that no cycling is necessary.

The detector packages for both spectrometers are shown in Fig. 2.9. When a particle goes through either spectrometer, the hit pattern in the Vertical Drift Chambers (VDCs) is used to reconstruct its track, which can be used to determine its momentum, scattering angle and reaction vertex at the target. The scintillator planes (S1/S2) provide timing information and generate triggers. The following is a description of all the detectors in more detail.

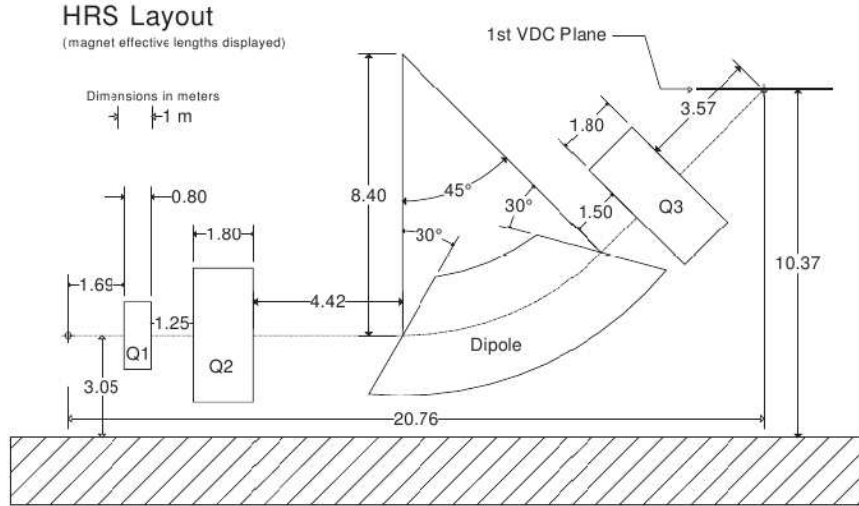


Figure 2.8: Schematic layout of a HRS device, showing the geometrical configuration of the three quadrupole and the dipole magnets. Distances are indicated in meters. Also shown is the location of the first VDC tracking detector.

2.4.1 Vertical Drift Chambers (VDCs)

The trajectory of the charged particle is recorded by two VDCs. The concept of VDCs fits well into the scheme of a spectrometer with small acceptance, allowing a simple analysis algorithm and high efficiency. As shown in Fig. 2.10 [46], two parallel VDCs are separated by 335 mm, and each VDC is composed of two wire planes in a standard UV configuration, i.e. the 368 sense wires in one plane are orthogonal to those in the other plane. The VDCs are inclined at an angle of 45° with respect to the nominal particle trajectory. The lower horizontal VDC coincides with the spectrometer focal plane.

The VDCs, filled with a gas mixture of Argon (62%) and Ethane (38%), are operated at a high voltage of 4.0 kV. When a charged particle passes through the VDC, the gas along its trajectory will be ionized and electrons will drift along the electric field line towards the wires. Normally five to six adjacent wires will produce signals. From the shortest drift time to the wires in each plane, the spatial coordinates and the trajectory can be determined.

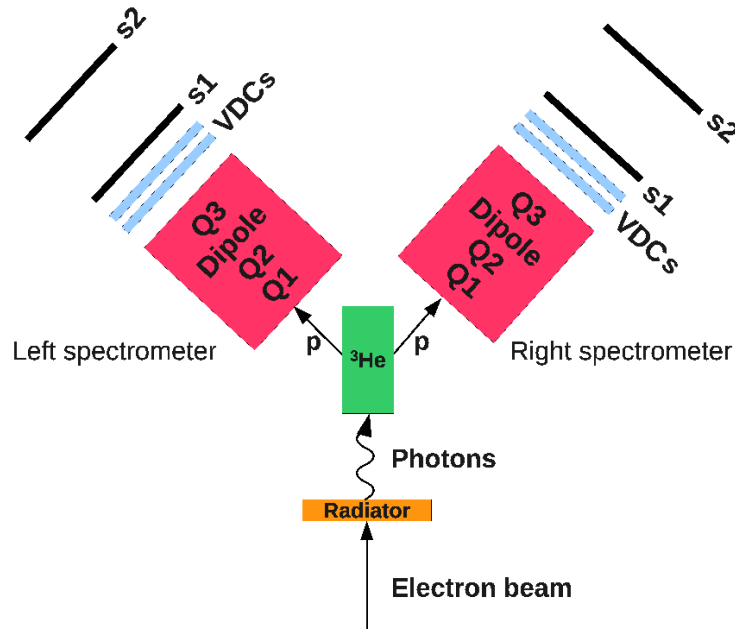


Figure 2.9: Schematic view of the experimental setup for E03-101. Not shown in this drawing are the Cerenkov and lead-glass counters of the HRSs which were not used in this experiment.

2.4.2 Scintillators

The trigger and timing information are provided by two primary scintillator planes (S1 and S2) in each spectrometer, separated by a distance of about 2 meters. The $S1_{HRS-L}$, $S2_{HRS-L}$ and $S1_{HRS-R}$ planes are composed of six thin (5 mm) overlapping paddles made of plastic scintillator (BICON 408). For $S2_{HRS-R}$, a slightly modified scintillator plane was used (called S2m), which consisted of 16 paddles. The photons produced by the ionizing particle passing through the scintillator are collected by two Photo-Multiplier tubes (PMTs) (2 inch Burle 8575) at the end of each paddle.

TDC Offset Calibration

The particle's time-of-flight (TOF) is determined from time difference between the S1 and S2 planes. The time for each plane is taken as the average of the time

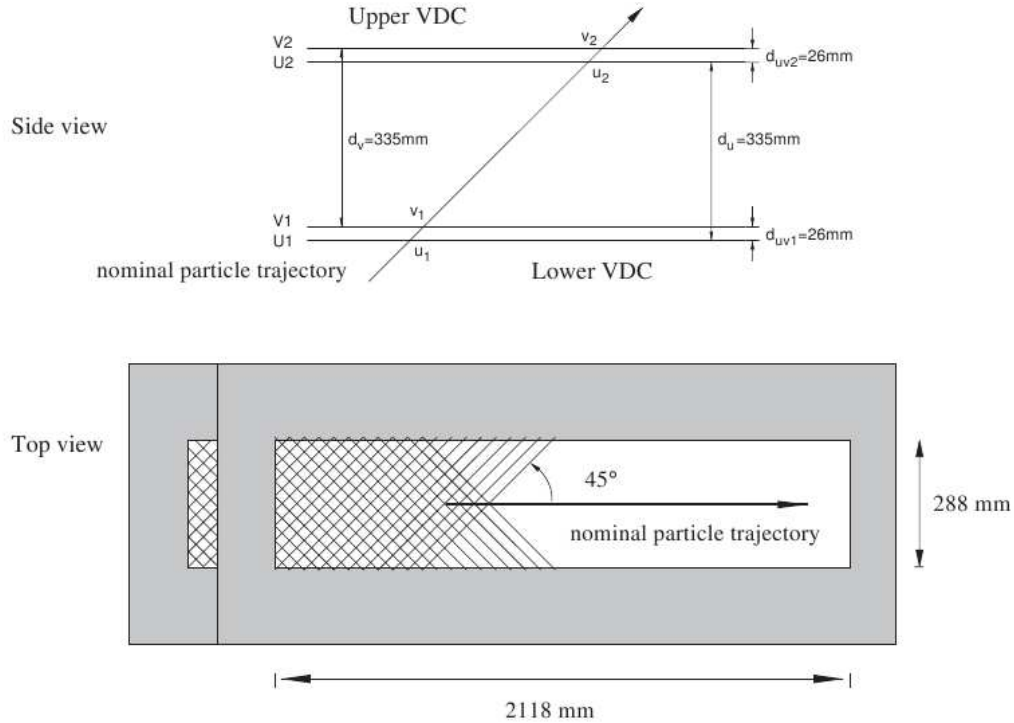


Figure 2.10: Schematic layout of the VDCs in Hall A.

reading of the two TDCs on both ends of the paddle that fired. We calibrated the time offset value of each TDC, to compensate for different time delays due to different cable lengths, electronic delay, etc. The procedure has been done in two steps: First we calibrated the *relative* offset between different paddles in each plane, then we calibrated the *absolute* overall offset for all TDCs of the plane to produce the known TOF.

The relative calibration was done by selecting events in which a particle passed through two neighboring paddles and caused them both to fire simultaneously. To suppress events where two different particles coincidentally passed through the two paddles, a cut on the number of VDC reconstructed tracks was set to be 1. The offsets were calibrated so that there will be no time difference between the two paddles that fired. Once this calibration was done, two peaks could be identified in the β vs. momentum spectrum as proton or deuteron. This allowed us to perform

the absolute time offset calibration between the S1 and S2.

Fig. 2.11 shows the β vs. momentum spectrum in HRS-L, the data is taken from the $E_{Beam} = 1.1$ GeV measurement. The effect of both steps of the calibration procedure can be observed by comparing the “Before” (top plot) to the “After” (bottom plot). On the top plot, the segments seen correspond to the different paddles of S1. On each of these segments, two lines are observed corresponding to protons and deuterons. On the bottom plot, these lines are aligned and their β value at $p = 1.1$ GeV/c for example, is correctly calibrated to:

$$\beta_p = \frac{p_p}{\sqrt{p_p^2 + M_p^2}} = \frac{1.1}{\sqrt{1.1^2 + 0.938^2}} = 0.76 \quad (2.2)$$

$$\beta_d = \frac{p_d}{\sqrt{p_d^2 + M_d^2}} = \frac{1.1}{\sqrt{1.1^2 + 1.876^2}} = 0.51 \quad (2.3)$$

Fig. 3.4 presents the velocity spectrum from the two spectrometers for coincidence events after the TDCs offsets were calibrated. A fit to the proton peak of HRS-L, gives $\frac{\sigma(\beta)}{\beta} = 7\%$, which is the nominal HRS resolution [46]. The resolution of HRS-R is slightly better, since the modified S2 scintillator (s2m) plane was used which consists of a larger number of paddles of smaller size each.

2.4.3 Event triggers

There are five types of triggers generated from the timing information of the scintillators [46]:

- T1: Main right arm trigger
- T2: Loose right arm trigger
- T3: Main left arm trigger
- T4: Loose left arm trigger
- T5: Coincidence of T1 and T3

The required mixture of different triggers for the data collection can be obtained by setting prescale factors, which means that only one out of a given number of events

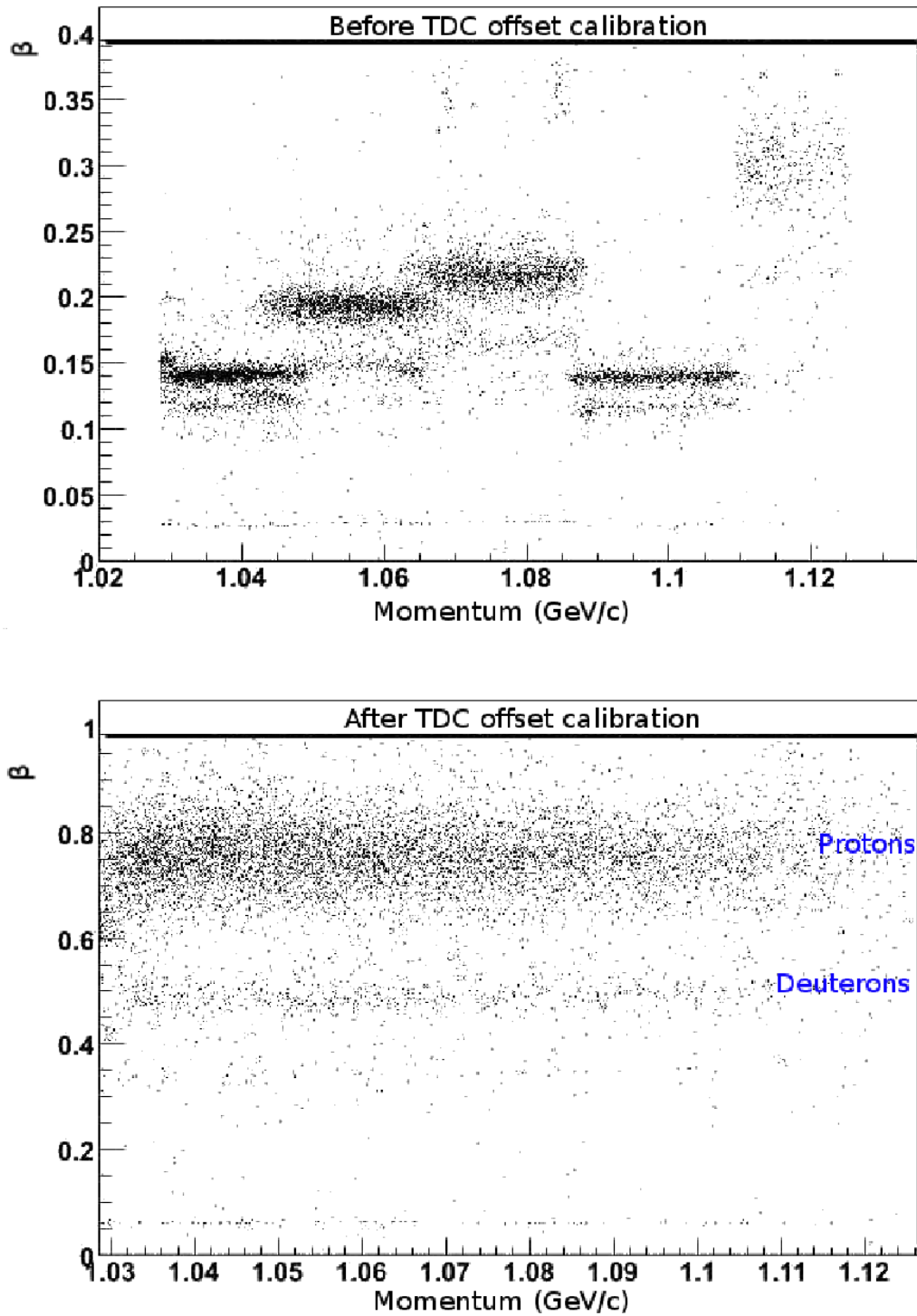


Figure 2.11: β vs momentum spectrum in HRS-L, the data is taken from the $E_{Beam} = 1.1$ GeV measurement. The top plot displays the spectrum before the TDC offset calibration, the bottom one shows it after.

with that type of trigger will enter the data stream. The prescale factors do not change the scaler readings.

The definition of triggers may vary for different experiments. During experiment E03-101, the main triggers for one spectrometer were formed when both scintillator planes (S1 and S2) fired, normally implying that a charged particle passed through the spectrometer. The loose triggers were used to estimate efficiency. They were formed when only one scintillator plane, S1 or S2, fired. Trigger T5 is a coincidence of T1 and T3, normally implying that two particles detected by the two spectrometers were produced at the target simultaneously.

2.5 Data Acquisition System

The data acquisition (DAQ) system in Hall A uses CODA (CEBAF Online Data Acquisition) developed by the JLab data acquisition group [53]. CODA is a toolkit composed of software and hardware from which a data acquisition system can be built to manage the acquisition, monitoring and storage of data. The typical CODA system is constructed from modular component (usually programs) that are spread over a network of processors. These processors may take the form of embedded CAMAC, VME or FASTBUS modules, or PC/Workstation systems. The custom hardware elements include the trigger supervisor (TS) that synchronizes the readout of the front-end crates and handles the dead time logic of the system. The most important custom software components are the readout controller (ROC) running on the front-end crates, the event builder (EB), event recorder (ER), event transfer (ET) and finally RunControl. The RunControl is the graphical user interface from which users can select experimental configurations, start and stop runs, and reset, transfer and monitor CODA components.

For each event with a trigger accepted by the trigger supervisor, data are gathered from the front-end boards by the ROC component, which buffers the data in

memory and sends these buffers via network to the EB running on a workstation. The EB builds events from fragments sent by the various ROCs and passes them to the ER which writes data to a local disk. The data are subsequently written to tapes in the MSS (Mass Storage tape Silo). Through the ET system, various additional pieces of data, from the control system and scalers from example, are inserted into the data stream every few seconds.

The recorded raw data were analyzed during the measurement (online) and carefully again (offline). The details of the analysis are given in Chapter 3.

CHAPTER 3

Data Analysis

3.1 Overview

The raw data from the data acquisition (DAQ) system were replayed by an event-processing program, “The Hall A analyzer” [54] (henceforth called “analyzer”). The analyzer is a C++ based code which uses the CERN ROOT data-analysis framework [55]. A new package called LibGammPP was written for the calculation of ${}^3\text{He}(\gamma,pp)n$ kinematics (see section 3.2.5). The events of interest were extracted by applying cuts on certain variables such as trigger type, particle type, spectrometer acceptance, and reconstructed momentum of the photon and neutron. Next, the event yield was normalized by the recorded beam charge, and the electrodisintegration background was subtracted to extract the *photo-disintegration yield per photon*, using the known bremsstrahlung distribution [56].

To extract the differential cross section, simulations were carried out by using a modified MCEEP (Monte Carlo for (e,e’p)) program [57] written for JLab Hall A. The inputs to the simulation include the spectrometers structures and settings, the beam energy, the bremsstrahlung distribution, and the momentum distribution of the neutron in the ${}^3\text{He}$ target. The differential cross section was calculated by normalizing the simulated yield to the measured photo-disintegration yield.

Major procedures in the data analysis are shown as a flow chart in Fig. 3.1. Details of the analysis from raw data to cross section are given in the following sections of this chapter.

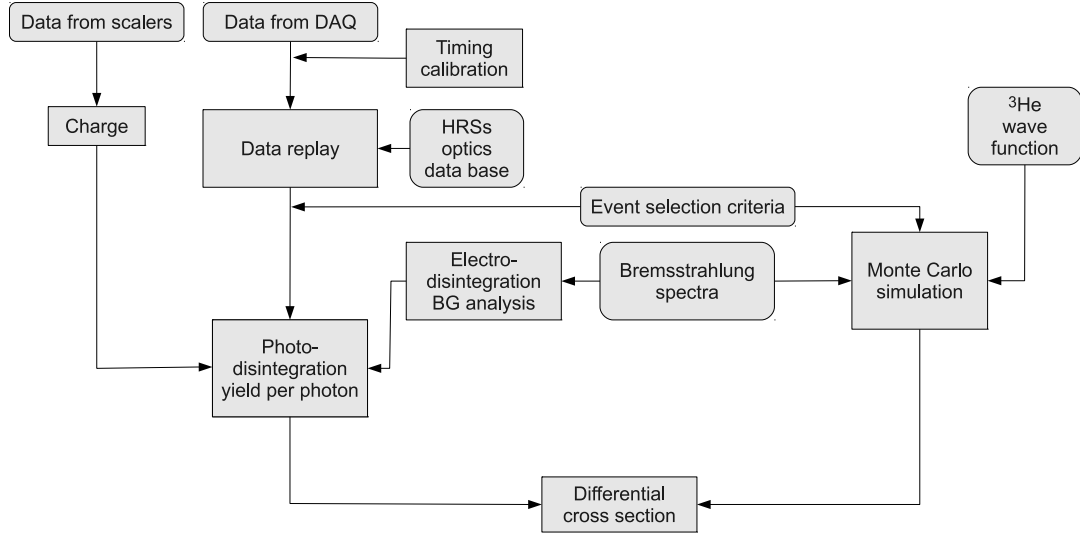


Figure 3.1: Schematic of the data analysis work flow.

3.2 Event Selection

‘‘Perfection is achieved, not when there is nothing more to add, but when there is nothing left to take away.’’ --Antoine de Saint-Exupery

The differential cross section is proportional to the number of measured events, in a given kinematics. It is therefore important to carefully select those events which will be analyzed and verify that they correspond to the kinematical conditions for which the cross section is reported. The reported cross section in this analysis is for ‘‘Photo-disintegration of proton pairs at 90° c.m.’’. The appropriate event selection should verify that:

- The two detected particles are identified as protons,
- The two detected protons emerged from the same nuclei,
- The momentum and angles of the detected protons are within the nominal acceptance of the HRSs, which were centered at $\theta_{cm}=90^\circ$ kinematics,

- There were no extra particles produced in the reaction,
- Spectator-neutron kinematics requirements are fulfilled.

In this experiment, the two HRSs were set for “positive polarity”, which means that the magnetic field of their dipole magnets was set to bend positive charge particles track upwards into the detector stack. As will be evident from various spectra shown below, these settings suppress the detection of almost every process other than ones which originated from the breakup of the ^3He nuclei to protons and deuterons.

3.2.1 Coincidence Between HRS-L and HRS-R

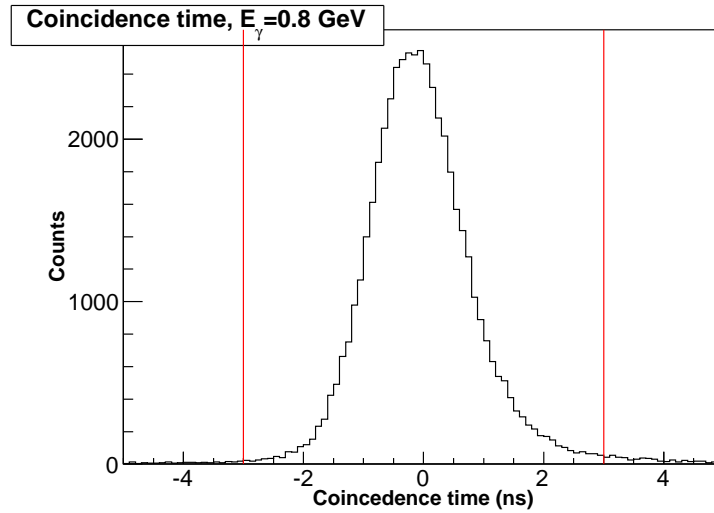


Figure 3.2: A typical coincidence time distribution. The time difference between the trigger time of HRS-L and HRS-R is plotted in black for data taken at $E_\gamma = 0.8$ GeV kinematics. The selections cuts are indicated in red.

An event is recorded when two particles are detected in coincidence by HRS-L and HRS-R. Figure 3.2 shows the distribution of the difference of the recorded detection time between HRS-L and HRS-R. The coincidence time resolution is determined by the individual timing resolution of each HRS. These resolutions are determined by the timing resolution of the two scintillator planes which the particle goes through when it enters and exists the detector package. $\sigma_{plane} = 0.3$ ns [46],

so that $\sigma_{HRS} = \sqrt{2} \cdot \sigma_{plane} = 0.42$ ns and $\sigma_{coinc} = \sqrt{2} \cdot \sigma_{HRS} = 0.59$ ns. This value is comparable with the width of the measured coincidence distribution shown in Figure 3.2 (RMS=0.70 ns). Events that fall within this peak are coincidence events. The red lines indicates the cut on the coincidence time.

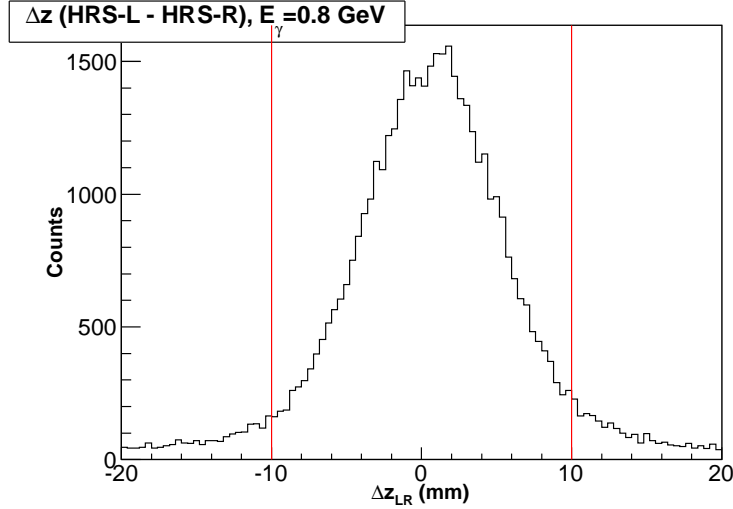


Figure 3.3: A typical vertex-z distribution, for events which passed the coincidence time cut. The difference between the reconstructed vertex z coordinate at the target from HRS-L and HRS-R is plotted in black for data taken at $E_\gamma = 0.8$ GeV kinematics. The selections cuts are indicated in red.

A second measure used to reduce random coincidence events is to apply a cut on the difference between the reconstructed reaction vertices from HRS-L and HRS-R, Δz_{LR} , as shown in Figure 3.3. The “position-at-target” resolution of each HRS is approximately $\Delta z_{HRS} = 1.5$ mm [52]. So that $\Delta z_{LR} = \sqrt{2} \cdot \Delta z_{HRS} = 2.1$ mm. This value is comparable with the width of the measured Δz_{LR} distribution of Figure 3.3 (RMS=3.4 mm). We therefore place an additional cut on Δz_{LR} (indicated in Fig 3.3 in red) for all events that falls within the time coincidence cut.

3.2.2 Particle Identification

The velocity of a particle triggering an event in the HRS is calculated from it’s time-of-flight between two scintillator planes. Once the coincidence cuts are

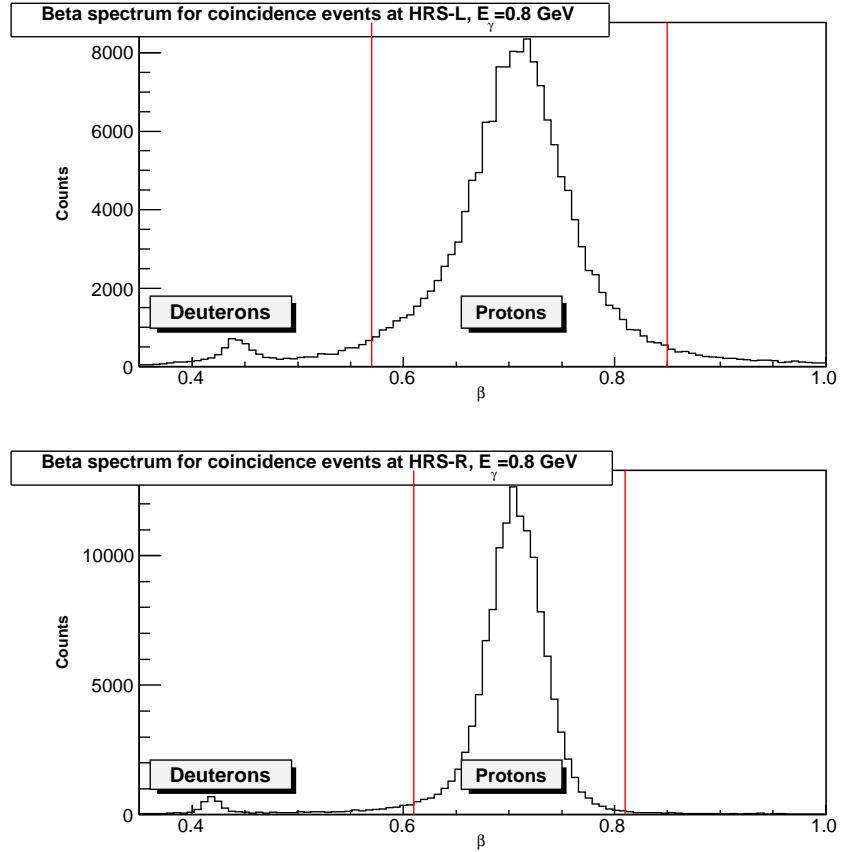


Figure 3.4: A typical β -distributions from HRS-L (top) and HRS-R (bottom) are plotted in black for coincidence events taken at $E_\gamma = 0.8$ GeV kinematics. The coincidence time and vertex- z cuts are specified in Sec. 3.2.1. The two clear peaks are identified as deuterons and protons, as described in the text. The selections cuts set for protons identification are indicated in red. The narrower distribution of HRS-R is due to its better timing resolution which results from the larger number of paddles of smaller size each in its s2m plane

placed, the velocity spectrum presented in Figure 3.4, shows two clear peaks. The momentum for particles detected by the HRS is defined within $\pm 4.5\%$ by the spectrometers acceptance. For these particles, the relation $\beta = \frac{p}{E} = \frac{p}{\sqrt{p^2 + M^2}}$ allows to clearly identify them as either deuterons or protons.

3.2.3 Nominal Detection Phase-Space

A particle passing through the HRS to the detector package, goes through the magnetic fields of a dipole and 3 quadrupoles magnets. The momentum of the particle is determined from our knowledge of its trajectory, which is derived from the

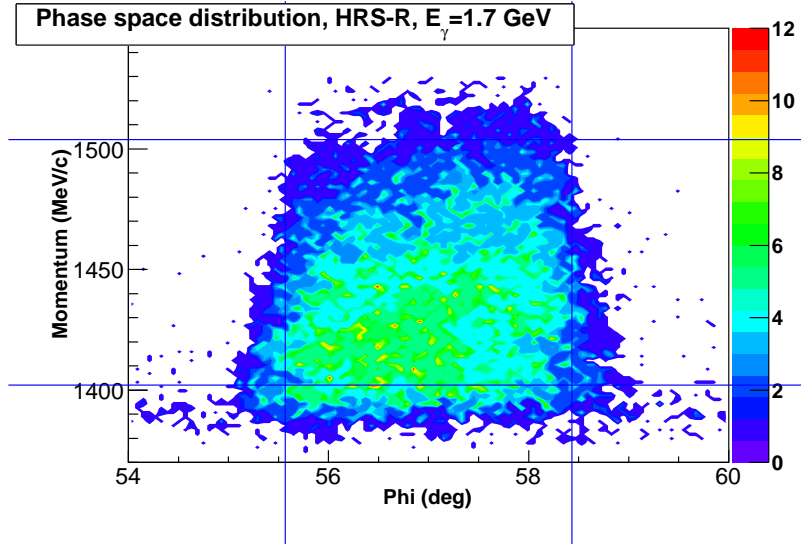


Figure 3.5: A typical phase space distribution, momentum vs. ϕ (in-plane angle). The spectrum is for the two proton coincidence events. The data are for HRS-R at $E_\gamma = 1.7$ GeV kinematics. The nominal acceptance is indicated in red and the cuts chosen to select events are in blue.

hit positions on the VDCs. This is done using data from calibration measurements called “the optics matrix” [51]. This data is collected by measurement of the hit positions of particles with known momentum. The uncertainties involved with this procedure tend to rise for trajectories which are passing close to the edges of the HRS acceptance (in momentum and angle). A simple way to handle this difficulty is to remove events which are close to the acceptance edges. The procedure we used to determine how close to the edges those cuts should be is to calculate the cross section for larger and larger acceptance cuts and pick the largest acceptance in which the cross section value stays constant.

Figure 3.5 shows the phase space distribution of events with two protons in coincidence: momentum vs. ϕ (the in-plane angle). The nominal acceptance of the HRSs, taken from [52], and the selected values for this analysis are listed in Table 3.1.

Nominal acceptance	Cuts selected for this analysis
$\Delta p = \pm 4.5\%$	$\pm 3.5\%$
$\Delta\phi = \pm 28$ mr	± 25 mr
$\Delta\theta = \pm 60$ mr	± 60 mr

Table 3.1: Cuts on momentum and angles for the event selection of this analysis.

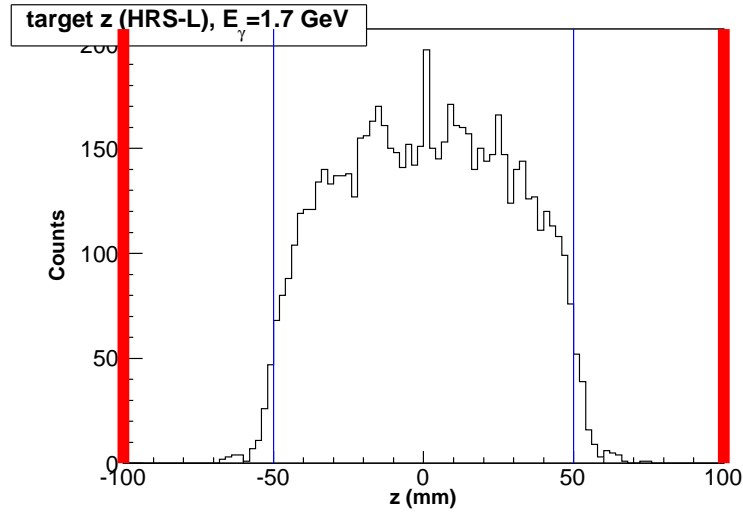


Figure 3.6: A typical target vertex distribution. The spectrum of the z coordinate of the reconstructed vertex by HRS-L is plotted in black for data taken at $E_\gamma = 0.8$ GeV kinematics. The selections cuts are the central 10 cm of the target indicated in blue. The position of the target walls are indicated in red.

3.2.4 Vertex Position at the Target

The central angles of the two HRSs are directed at the target's center. Their acceptance allows the detection of particles originating from approximately ± 5 cm around the center, with somewhat degraded acceptance away from the center. Figure 3.6 shows an example of the reaction vertex distribution as reconstructed by HRS-L. Only events within the central ± 5 cm of the target (cuts are indicated in red) were chosen for this analysis.

3.2.5 Kinematic Reconstruction

A key feature of our experimental method is the ability to fully reconstruct the kinematics of each ${}^3\text{He}(\gamma, \text{pp})\text{n}$ event using the measured momentum of the two outgoing protons. This reconstruction is carried under the assumption that except for the two detected particles, no extra particle was generated in the reaction. This assumption is later validated by selecting events with energy no more than 140 MeV (which is threshold energy for producing a pion) off the Bremsstrahlung energy distribution tip.

The ${}^3\text{He}(\gamma, \text{pp})\text{n}$ two-body events may be described in momentum space by:

$$\vec{p}_{p1}, \vec{p}_{p2}, \vec{p}_n \text{ and } p_{\gamma z}.$$

Where \vec{p}_{p1} , \vec{p}_{p2} and \vec{p}_n are the protons and neutron momentum vectors, and $p_{\gamma z} = E_\gamma$ is the photon's momentum along the z axis (chosen to be the electron beam direction). The demand of momentum and energy conservation:

$$\begin{aligned} E_\gamma + M_t &= E_{p1} + E_{p2} + E_n \\ \vec{p}_\gamma &= \vec{p}_{p1} + \vec{p}_{p2} + \vec{p}_n \end{aligned} \quad (3.1)$$

where E_{p1} and E_{p2} are the protons energies, E_n is the neutron's energy and M_t is target mass, constraints this system to have a unique solution for known \vec{p}_{p1} , \vec{p}_{p2} .

Solving for E_γ :

$$E_\gamma = \frac{1}{2} \frac{m_n^2 - 2m_n(E_{p1} + E_{p2}) + 2m_p^2 + 2E_{p1}E_{p2} - 2|\vec{p}_{p1}||\vec{p}_{p2}|\cos(\theta_{scat})}{E_{p1} + E_{p2} - P_{1z} - P_{2z} - m_n} \quad (3.2)$$

Where θ_{scat} is the opening angle between the two protons and P_{1z} , P_{2z} are the protons momentum projection along the z axis.

Photon Energy

As explained above, events are selected to have no less than 140 MeV below the bremsstrahlung tip ($E_\gamma = E_e$). Figure 3.7 shows a typical photon energy distribution,

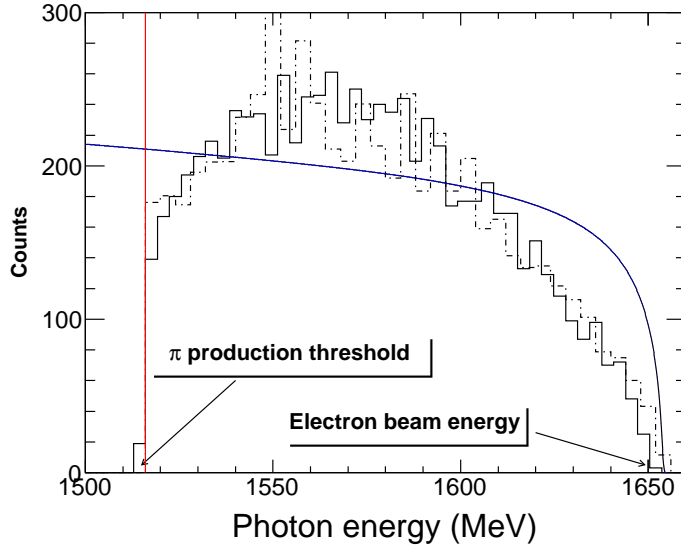


Figure 3.7: A typical photon energy distribution for two proton coincidence events at beam energy of 1.655 GeV. Solid line represents reconstructed photon energy for the photodisintegration events, dashed line the simulation results. The calculated bremsstrahlung spectrum is shown as a solid blue line. All results are normalized to the measured yield. The cut for photon energy above the 140 MeV pion production threshold is indicated in red.

the 140 MeV cut is indicated in red.

Neutron Momentum

As described in section 1, the experiment aims to measure the cross section for the breakup of a proton pair out of ${}^3\text{He}$ under the assumption of a spectator neutron. This assumption corresponds to selection of events with low neutron momentum. Figure 3.8 shows the reconstructed momentum distribution of the neutron for two protons coincidence events. The experimental acceptance is degraded for events with high p_n . The evaluation of the acceptance is not handled analytically, but rather using a MC simulation, as explained in Sec. 3.3.3. The neutron momentum end point of the accepted event distribution varies from one data point to another, and is in the range of 100 – 120 MeV/c. In order to report the cross sections for a fixed range of p_n , which can be compared to theory, a cut is placed both on data and simulation for events with neutron momentum below 100 MeV/c.

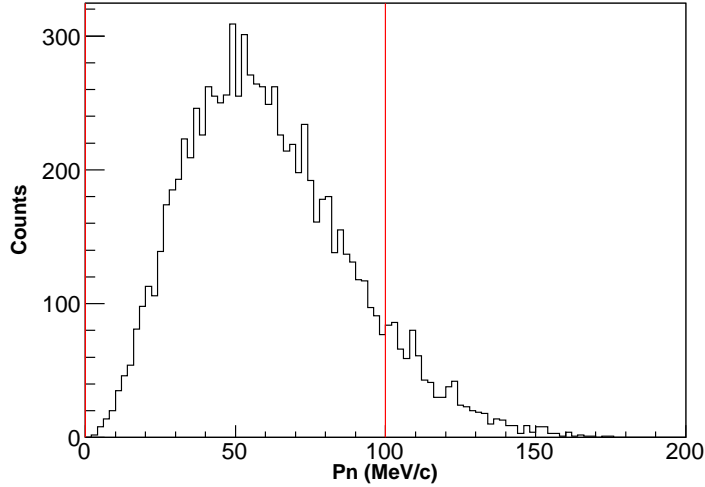


Figure 3.8: A typical neutron momentum distribution. The spectrum of the reconstructed neutron momentum for events with two protons in coincidence is plotted in black for data taken at $E_\gamma = 1.7$ GeV kinematics. The selections cut for neutrons with momentum smaller than 100 MeV/c is shown in red.

3.3 The Differential Cross Section

The observable best suited to link reaction dynamics predicted by theory to scattering experimental results is the “scattering cross section”. The fundamental relation:

$$R_i = L \cdot \sigma, \quad (3.3)$$

aggregates all parameters that govern scattering experiments into three quantities: L , the “luminosity”, is the number of beam particles per unit time times the number of target nuclei per unit area. This quantity is a product of all parameters related to the beam and target used. R_i is the scattering rate. σ , the cross section, expresses the likelihood of interaction between particles. This relation may be differentiated by various parameters. For the experimentalist, one obvious choice is the scattering angle in the lab frame: R_i can be measured for different angles to extract $\frac{d\sigma}{d\Omega_{lab}}$. For theoretical interpretation, a Lorentz-invariant quantity is more appealing and the “invariant cross section”, $\frac{d\sigma}{dt}$, is calculated. The relation between the two may be

given as the product of the two Jacobians:

$$\frac{d\sigma}{dt} = \frac{d\sigma}{d\Omega_{lab}} \frac{d\Omega_{lab}}{d\Omega_{cm}} \frac{d\Omega_{cm}}{dt} \quad (3.4)$$

which translate the cross section differentiated by the scattering angle in the lab frame first to center of mass frame and then to be differentiated by t , the momentum transfer.

Differential Cross Section in the Laboratory Frame

The luminosity is given by

$$L = N_{scatt} \cdot R_{\gamma} \quad (3.5)$$

with N_{scatt} being the number of scatterers in the target and R_{γ} the rate of the incident photon flux. N_{scatt} may be calculated by

$$N_{scat} = \frac{N_A \cdot \rho \cdot l}{A} \quad (3.6)$$

where N_A is Avogadro number, ρ is the target's density, l is the target's length, and A is the mass number of the target nuclei. In our case the photon flux is generated by Bremsstrahlung in a copper radiator, so R_{γ} can be calculated from the well understood Bremsstrahlung spectra [56] by

$$R_{\gamma} = I_e \cdot f_{\gamma/e} \quad (3.7)$$

with I_e is the electron beam current and $f_{\gamma/e}$ is the number of bremsstrahlung photons per electron taken from [56]. We note that R_i is related to the measured yield by

$$R_i = \frac{Y_{\gamma-pp}}{T \cdot D_{eff}} \quad (3.8)$$

where $Y_{\gamma-pp}$ is the yield of photodisintegrated proton pairs measured in coincidence,

T is the time of the measurement, and D_{eff} is the detection efficiency ($0 < D_{eff} < 1$). Combining Eqs. (3.1)-(3.6), and denoting the number of photons $N_\gamma = R_\gamma \cdot T$ we get

$$\sigma = \frac{Y_{\gamma-pp}}{N_\gamma \cdot N_{scat} \cdot D_{eff}} \quad (3.9)$$

For a detector that has small enough solid angle, $\Delta\Omega$, this relation may be differentiated and expressed as

$$\frac{d\sigma}{d\Omega_{lab}} = \frac{\Delta Y_{\gamma-pp}}{N_\gamma \cdot \Delta\Omega \cdot N_{scat} \cdot D_{eff}} \quad (3.10)$$

3.3.1 Calculation of the Laboratory Differential Cross Section

$\Delta Y_{\gamma-pp}$ in Eq. (3.10) is the number of photo-produced proton pairs in the experiment, detected within the phase-space volume which the differential cross section is reported for. This phase-space bin is determined by the θ_{cm} angle, the photon energy, and the maximum momentum we allow the neutron to have (to justify the spectator assumption). The number of photo-produced proton pairs recorded in the experiment, $Y_{\gamma-pp-exp}$ is not equal to $Y_{\gamma-pp}$, since the HRSs acceptance covers this phase-space bin only partly (15 – 60 %). The actual value of this coverage, which we call “coincidence efficiency”, is energy dependent. A proton pair produced by a higher energy photon has greater probability to fall within the HRSs finite acceptance, due to “Kinematic focusing”.

To handle the partial acceptance of the two HRSs, we evaluate $\frac{d\sigma}{dt}$ using the following procedure:

1. Evaluate $Y_{\gamma-pp-exp}$, the number of recorded events that pass the selection cuts

(Sec 3.2) after background subtraction, to be discussed below (Sec 3.3.2).

2. Run a Monte-Carlo simulation of the experiment (Sec 3.3.3), using an arbitrary cross section ¹ $\frac{d\sigma}{d\Omega_{lab0}}$ and arbitrary charge Q_0 and normalize according to the measured yield $Y_{\gamma-pp-exp}$ and charge Q_{exp} :

$$\frac{d\sigma}{d\Omega_{lab}} = \frac{d\sigma}{d\Omega_{lab0}} \cdot \frac{Y_{\gamma-pp-exp}}{Y_{\gamma-pp-MC}} \cdot \frac{Q_0}{Q_{exp}} \quad (3.11)$$

3. Evaluate the average values of $\frac{d\Omega_{lab}}{d\Omega_{cm}}$ and $\frac{d\Omega_{cm}}{dt}$ for each bin (Sec 3.3.5).
4. Calculate $\frac{d\sigma}{dt}$ according to Eq. (3.4).

To validate the assumption made in Eq. 3.10 about the cross section being constant within the selected bin, this procedure was repeated for larger and larger selection of phase-space cuts around the center of the bin, confirming that the resulted cross section value remains stable. ²

3.3.2 Subtraction of the Electro-Production Background

In the experiment, a pair of protons measured in coincidence results from disintegration of the ³He nucleus either by a photon or an electron. The total cross section can be written as:

$$\sigma = \sigma_{\gamma-pp} + \sigma_{e-pp} \quad (3.12)$$

Where σ_{e-pp} is the cross section for electro-disintegration and $\sigma_{\gamma-pp}$ is the cross section for photo-disintegration. In order to extract $\sigma_{\gamma-pp}$, we need to evaluate the electro-production yield and then subtract it from the measured yield. To do so, we also preformed measurements *without* placing the copper radiator in the electron's

¹Since we expect the cross section to scale, a convenient choice for the value of $\frac{d\sigma}{d\Omega_{lab0}}$ is a constant times s_{pp}^{-11} . This is described in detail in Sec. 3.3.3.

²This procedure was possible since the full experimental acceptance forms a very small volume in phase-space. In the general case of scattering experiments, if the cross section varies over the acceptance, this procedure would have been preformed on smaller sub-bins and the calculated cross sections would have been averaged on the reported bin.

way (“radiator-out” runs).

If we denote the ratio of yield to charge, for radiator-in/radiator-out measurement by R:

$$R_{in} = Y_{in}/Q_{in} \quad (3.13)$$

$$R_{out} = Y_{out}/Q_{out} \quad (3.14)$$

Then the photo-disintegration cross section will be proportional to:

$$\sigma_{\gamma-pp} \propto (R_{in} - R_{out}) \quad (3.15)$$

We can define the photo-production to electro-production ratio per photon as:

$$\lambda_{\gamma/e} = \frac{R_{in} - R_{out}}{R_{out}N_{\gamma/e}} \quad (3.16)$$

Where $N_{\gamma/e}$ is the number of photons per electron in the bremsstrahlung spectra. Figure 3.9 shows the measured $\lambda_{\gamma/e}$ as a function of the photon energy.

For the two highest energies, 4.1 GeV and 4.7 GeV, no radiator-out data were taken, due to the very low count rate at those energies. To evaluate the electro-disintegration background at those two energies, we fitted the measured values of $\lambda_{\gamma/e}$ with polynomial curves (displayed in different colors on Figure 3.9):

- 2 fit parameters: linear (red) fit.
- 3 fit parameters: quadratic (green) fit.

We concluded that the linear and quadratic fits have reasonable $\chi^2 \approx 1$ values, and so we pick the range between them (shaded) as the uncertainty in $\lambda_{\gamma/e}$, and the mid value between them as it’s estimated value. Fig. 3.10 shows the yield-to-charge super-ratio, radiator-in over radiator-out: $\lambda_{in/out} = R_{in}/R_{out}$. $\lambda_{in/out}$ as calculated from the data are presented in blue for the 6 lower energies. The ratio calculated

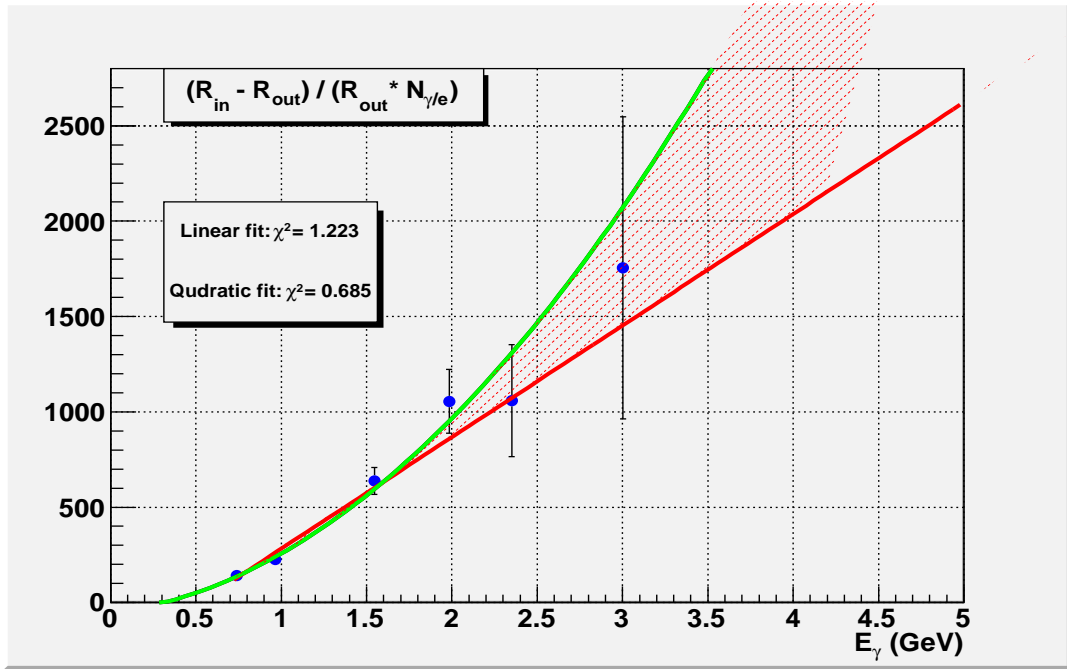


Figure 3.9: $\lambda_{\gamma/e}$ (defined in Eq. 3.16) as a function of photon energy. Polynomial fits with 2 and 3 fit parameters are shown with their respective χ^2 . The area between the linear and quadratic fits is shaded.

from the linear fit is presented in red and from the quadratic fit in green. We use the value of $\lambda_{in/out}$ to evaluate $Y_{\gamma-pp-exp}$ for the cross section calculation using:

$$Y_{\gamma-pp-exp} = Y_{in} \left(1 - \frac{1}{\lambda_{in/out}}\right) = Y_{in} \cdot \Gamma_{\gamma/e} \quad (3.17)$$

Where $\Gamma_{\gamma/e}$ is the fraction of the proton pairs recorded in the experiment which were disintegrated by a photon. Table 3.2 shows the extrapolated values of $\Gamma_{\gamma/e}$, both from the linear and quadratic fit, and the range between them that was used to determine the uncertainties in the analysis.

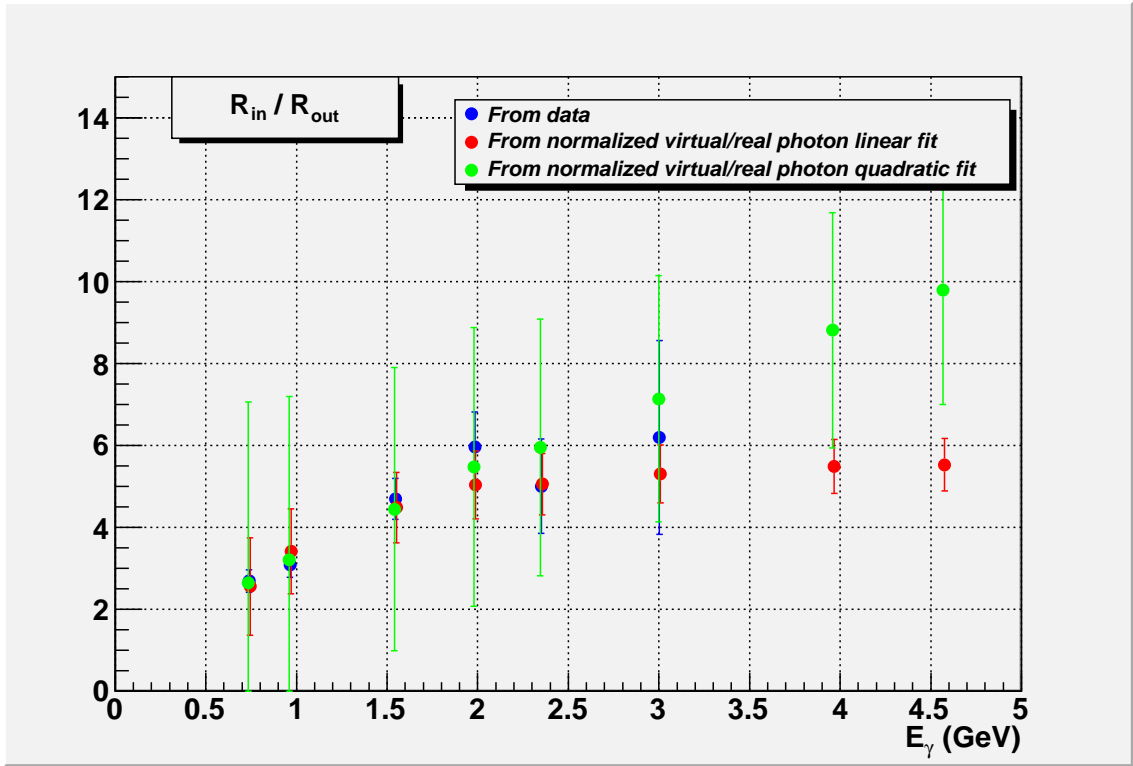


Figure 3.10: R_{in}/R_{out} as a function of photon energy.

3.3.3 Event Simulation Using MCEEP

Overview

The Monte Carlo simulation was done by using MCEEP (Monte Carlo for (e,e'p)) [57], a computer program designed to simulate coincidence (e,e'X) experiments in Hall A. It was modified in the kinematics, cross section, and bremsstrahlung photon yield calculation to simulate the photodisintegration process, following methods previously conducted in Hall A photo-reactions analysis [58].

The MCEEP program employs a uniform random sampling method to populate the experimental acceptance. An event is defined as a combination of variables that completely specifies the reaction in the lab. The cross section is used to weight the event. A block diagram of the MCEEP simulation is shown in Figure 3.11. The

E_e	$\Gamma_{\gamma/e}$ (Data)	Linear Fit	Quadratic Fit	Used for the analysis
0.8	0.667 ± 0.002	0.638	0.656	0.647 ± 0.009 (1.4 %)
1.1	0.680 ± 0.006	0.717	0.697	0.707 ± 0.010 (1.4 %)
1.7	0.790 ± 0.010	0.777	0.773	0.775 ± 0.002 (0.3 %)
2.1	0.835 ± 0.024	0.800	0.816	0.808 ± 0.008 (1.0 %)
2.5	0.807 ± 0.056	0.800	0.832	0.816 ± 0.016 (2.0 %)
3.1	0.810 ± 0.081	0.801	0.862	0.832 ± 0.030 (3.6 %)
4.1	Not measured	0.814	0.890	0.852 ± 0.038 (4.5 %)
4.7	Not measured	0.815	0.902	0.859 ± 0.044 (5.1 %)

Table 3.2: Photo-production to electro-production ratio.

blocks to the right of the thick arrow are subroutines called by the main program MCEEP. Indented subroutines are within the main Monte Carlo event loop. At the start of the Monte Carlo event loop, the lab coordinates for both scattered particle and ejectile at the target are generated randomly and then converted to transport vectors, directly related to the spectrometer optics. The outputs of MCEEP are histograms and ntuples, which are included into a HBOOK file and converted into a “ROOT tree” format that can be read by the analysis software ROOT [55].

For the photodisintegration process ${}^3\text{He}(\gamma,pp)n$, the subroutine PHYS_CHOICE was modified in [58] to include a new option, which was called TWOBODY. The subroutine KINEM_TWOBODY was modified to calculate the corresponding kinematics and cross section. The photon energy was randomly generated by this subroutine, as well as the momentum of the neutron sampled from a ${}^3\text{He}$ wave function [59] input distribution.

Kinematics

The subroutine KINEM_TWOBODY was modified for the ${}^3\text{He}(\gamma,pp)n$ reaction. The modifications are listed below:

- Random generation of the photon energy within a 140 MeV window below the beam energy.

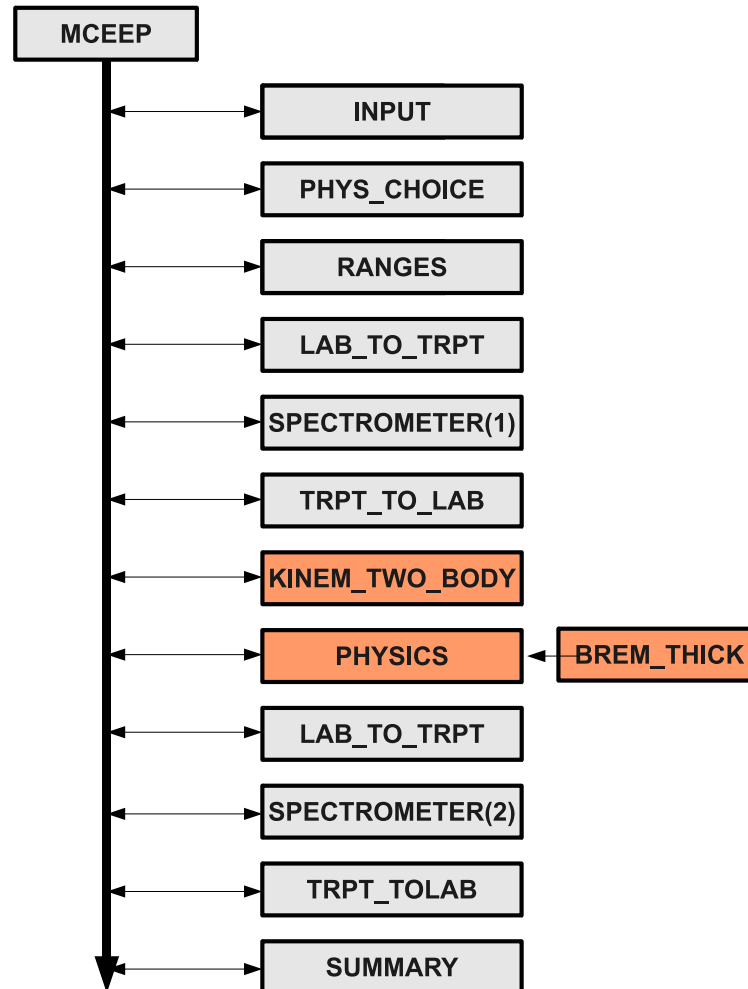


Figure 3.11: A block diagram of the simulation Monte-Carlo program "MCEEP". The orange blocks are the subroutines modified for this analysis.

- Random generation of the neutron momentum based on the ${}^3\text{He}$ wave function taken from [59].
- Added calculation of the light-cone momentum of the neutron (α_n).

The kinematic calculation steps are described in Table 3.3.

Cross Section

An ${}^3\text{He}(\gamma, pp)n$ option was added to the subroutine PHYSICS, which is responsible for assigning the event's weight. The weighted output histograms for the

Step	Subroutine
1 The first proton's angle is randomly sampled in the solid angle acceptance of the HRS	MCEEP
2 A photon energy is sampled from the Bremsstrahlung distribution	KINEM_TWOBODY
3 A neutron momentum vector is sampled up to the momentum cut, using the ^3He wave function	KINEM_TWOBODY
4 The rest of the kinematic variables are calculated from energy and momentum conservation constraints	KINEM_TWOBODY

Table 3.3: The calculation steps of the event kinematics in MCEEP.

various reaction parameters are used for comparing data to simulation as described in section 3.3.4. Each event is weighted by:

$$W = \frac{d\sigma}{d\Omega_0} \cdot f_{brem} \cdot D_{eff} \quad (3.18)$$

Where f_{brem} is the probability for a bremsstrahlung photon being generated, D_{eff} is the overall spectrometers detection efficiency and $\frac{d\sigma}{d\Omega_0}$ is the differential cross section. As described in Sec. 3.3.1, the simulation assumes an arbitrary cross section value. Since the cross section is expected to scale, it is convenient to have $\frac{d\sigma}{d\Omega_0}$ scale with s^{-11} :

$$\frac{d\sigma}{d\Omega_0} = s_{\gamma-pp}^{-11} \cdot A_{s_{\gamma-pp}^{11} \frac{d\sigma}{d\Omega}} \quad (3.19)$$

$s_{\gamma-pp}$ is the cm energy squared in the γ -pp system and $A_{s_{\gamma-pp}^{11} \frac{d\sigma}{d\Omega}}$ is an arbitrarily chosen constant.

Bremsstrahlung Photon Yield

The subroutine BREM_THICK was created to calculate the photon yield from a thick radiator, incorporating code written by Dave Meekins [60] based on reference [56]. This code considers energy losses of the electron beam in the radiator, and was found to have precision of 3% in previous Hall A radiator experiments [58].

Photo-Disintegrated Proton Yield

The simulation produces $Y_{\gamma-pp-MC}$, the photo-disintegration yield, which is used in Eq.(3.11). To evaluate it, the simulation averages the differential cross section over the fraction of iterations that survived the detectors acceptance as well as the applied software cuts. This method may be expressed as:

$$\begin{aligned}
 Y_{\gamma-pp-MC} &= W \cdot N_e \cdot \Delta\Omega \cdot N_{scat} \cdot C_{eff} & (3.20) \\
 &= \frac{d\sigma}{d\Omega_{lab0}} \cdot N_\gamma \cdot \Delta\Omega \cdot N_{scat} \cdot D_{eff} \cdot C_{eff} \\
 &= \frac{1}{N_{iter}} \left(\Delta\Omega \cdot N_{scat} \cdot D_{eff} \cdot \sum_{i \in Accepted}^{N_{iter}} \left(\frac{d\sigma}{d\Omega_{lab0}} \cdot N_\gamma^i \right) \right)
 \end{aligned}$$

where N_{iter} is the number of iterations, D_{eff} is the detection efficiency ($0 < D_{eff} < 1$), and C_{eff} is the ‘‘coincidence efficiency’’ which is the probability for a proton to be detected in the HRS, given that the other proton was detected in the other HRS.

3.3.4 Comparing Data and Simulation

To verify that our simulation reproduces correctly the experimental results, distributions of various reaction parameters were compared between the measured results and the simulation output. These parameters include:

- The In- and Out- of-plane angular distribution and momentum of the protons.
- The reaction vertex at the target.
- The reconstructed photon energy.
- The reconstructed neutron momentum.
- The spatial event distribution at the detectors aperture.

Fig. 3.12 shows a comparison of few parameters from the measurement at $E_e = 1.7$ GeV with the simulation results: The protons momentum at L- and R-HRS, The

out-of-plane angles (ϕ) for both spectrometers, the z- coordinate (along the beam direction) of the reaction vertex, the photon energy, the proton pair cm momentum, and the light-cone momentum of the neutron (α_n). As shown in the Figure, the simulation (black) is in very good agreement with the data (red).

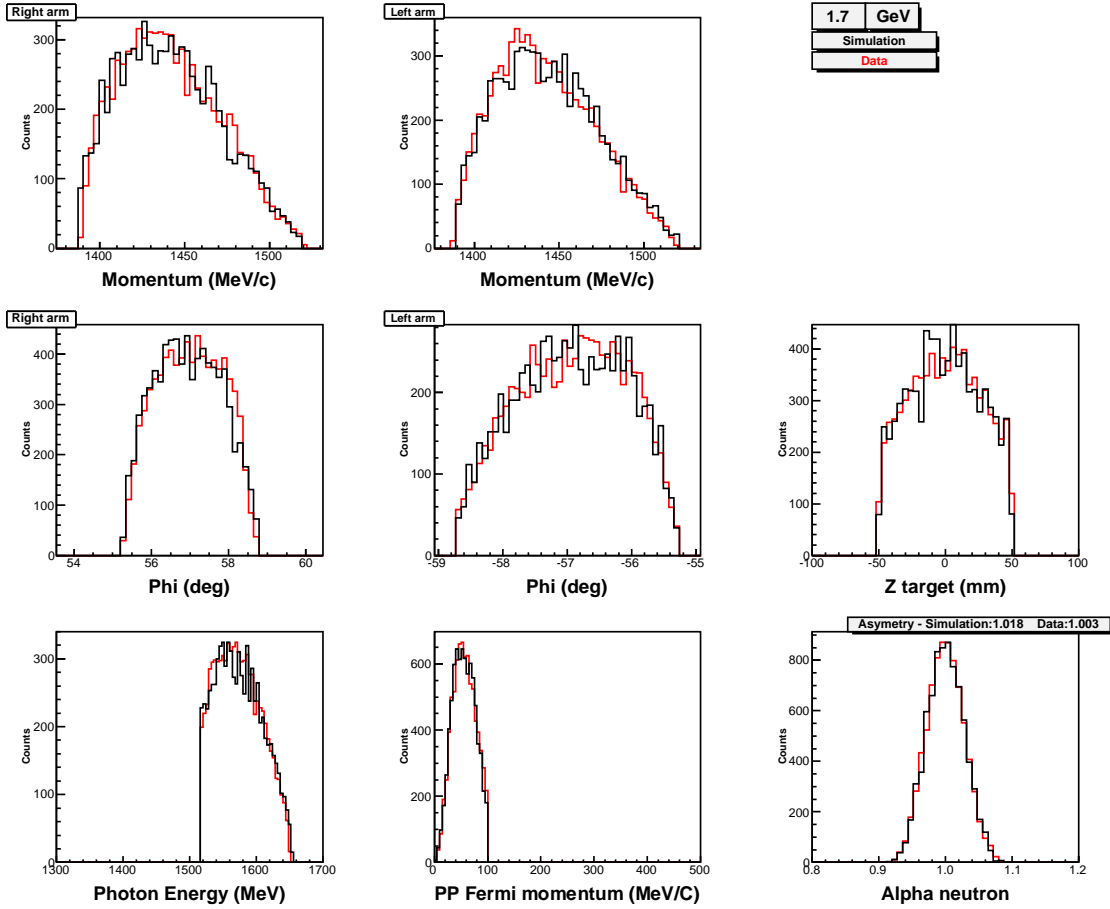
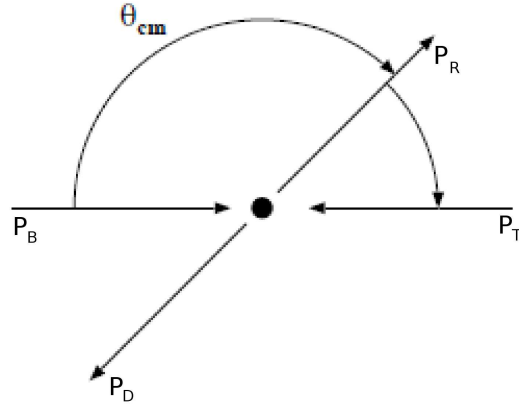


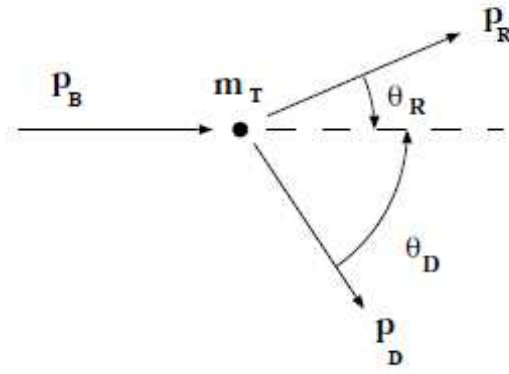
Figure 3.12: Comparison of various reaction variables - Data (red) vs. Simulation (black). This data set was taken at $E_e = 1.7$ GeV kinematics.

3.3.5 Jacobian $\frac{d\Omega_{cm}}{dt}$

Consider two body scattering in the center-of-mass frame as shown in Fig. 3.13(a). B is the beam particle; T is the target particle; and R and D are the detected outgoing particles: $B + T \rightarrow R + D$.



(a) In the center-of-mass frame.



(b) In the laboratory frame.

Figure 3.13: Two-body scattering kinematics.

The Mandelstam variable t is given by

$$t = (p_B^\mu - p_D^\mu)^2 = p_B^2 + p_D^2 - 2p_B^\mu p_{D\mu} \quad (3.21)$$

and $d\Omega_{cm}$ is given by

$$d\Omega_{cm} = 2\pi \sin(\pi - \theta_{cm}) d\theta = -2\pi d[\cos(\pi - \theta_{cm})]. \quad (3.22)$$

The quantity t may be expanded as

$$t = m_B^2 + m_D^2 - 2E_B E_D + 2|\vec{p}_B||\vec{p}_D| \cos(\theta_{cm}) \quad (3.23)$$

or equivalently

$$t = m_B^2 + m_D^2 - 2E_B E_D - 2|\vec{p}_B||\vec{p}_D| \cos(\pi - \theta_{cm}) \quad (3.24)$$

Therefore $\frac{dt}{d\Omega_{cm}}$ is:

$$\frac{dt}{d\Omega_{cm}} = \frac{|\vec{p}_B||\vec{p}_D|}{\pi} \quad (3.25)$$

which implies that the Jacobian is given by:

$$\frac{d\Omega_{cm}}{dt} = \frac{\pi}{|\vec{p}_B||\vec{p}_D|}. \quad (3.26)$$

3.3.6 Jacobian $\frac{d\Omega_{lab}}{d\Omega_{cm}}$

The Jacobian used to transform the cross section in the laboratory (*lab*) to the center-of-mass (*cm*) is used extensively in experimental nuclear and particle physics. The specific Jacobian for two particles in the initial and final states is discussed here. Consider the general process where a beam of particles interacts with a target stationary in the *lab* frame as shown in Fig. 3.13(b). Note that the velocity of the *cm* in the *lab* frame is given by

$$\vec{\beta}_{cm} = \frac{\vec{p}_B}{m_T + E_B} \quad (3.27)$$

which implies that

$$\gamma_{cm} = \frac{E_B + m_T}{E_{cm}} \quad (3.28)$$

Where E_{cm} is the total *cm* energy. The Lorentz transformation of momenta p and energy E from the *lab* to the *cm* is given by

$$\begin{pmatrix} E_{cm} \\ p_{cm} \cos(\theta_{cm}) \end{pmatrix} = \begin{pmatrix} \gamma_{cm} & -\gamma_{cm}\beta_{cm} \\ -\gamma_{cm}\beta_{cm} & \gamma_{cm} \end{pmatrix} \begin{pmatrix} E \\ p \cos(\theta) \end{pmatrix} \quad (3.29)$$

$$p_{cm} \sin(\theta_{cm}) = p \sin(\theta) \quad (3.30)$$

By using the above relations and noting that energy and momentum are conserved, the following equation may be obtained

$$\gamma_{cm}[p_{Dcm} \cos(\theta_{cm}) + \beta_{cm}E_{Dcm}] \tan(\theta) = p_{Dcm} \sin(\theta_{cm}) \quad (3.31)$$

Note that

$$d\Omega = -2\pi d(\cos(\theta)) \quad (3.32)$$

$$\frac{d(\sin(\theta))}{d\Omega} = \frac{\cos(\theta)}{2\pi \sin(\theta)} \quad (3.33)$$

and

$$\frac{d(\tan(\theta))}{d\Omega} = \frac{\sec^2(\theta)}{2\pi \sin(\theta)} \quad (3.34)$$

by differentiating the right hand side of Eq.(3.31) it can be seen that

$$\frac{d}{d\Omega_{cm}}(p_{Dcm} \sin(\theta_{cm})) = p_{Dcm} \frac{\cos(\theta_{cm})}{2\pi \sin(\theta_{cm})} \quad (3.35)$$

and the left hand side of the same equation

$$\begin{aligned} & 2\pi \frac{d}{d\Omega_{cm}} [\gamma_{cm}(p_{Dcm} \cos(\theta_{cm}) + \beta_{cm} E_{Dcm}) \tan(\theta)] \\ &= -\gamma_{cm} p_{Dcm} \tan(\theta) + \gamma_{cm}(p_{Dcm} \cos(\theta_{cm}) + \beta_{cm} E_{Dcm}) \frac{\sec^2(\theta)}{\sin(\theta)} \frac{d\Omega}{d\Omega_{cm}} \end{aligned} \quad (3.36)$$

Solving for $\frac{d\Omega}{d\Omega_{cm}}$ gives:

$$\frac{d\Omega}{d\Omega_{cm}} = \frac{\sin^2(\theta)}{\sin^2(\theta_{cm})} [\cos(\theta_{cm}) \cos(\theta) + \gamma_{cm} \sin(\theta_{cm}) \sin(\theta)]. \quad (3.37)$$

3.4 Efficiency Corrections and Experimental Uncertainties

3.4.1 Detection Inefficiencies

The detection inefficiency is taken into account by the event weighting of MCEEP, according to Eq.(3.18). The inefficiencies considered are:

- Inefficiencies due to poorly reconstructed tracks: Since random coincidence for the measurement of two positive-charge particle in coincidence using the HRSs is negligible, the reconstructed reaction vertex of each HRS should be within the HRS vertex resolution. Therefore, the fraction of events with vertex distance difference larger than the HRSs vertex resolution serve as an indicator for the tracking inefficiency. Using this method it was found to be on a 2% level.

- Computer deadtime: Coincidence event rate was very low, reaching 10^4 Hz at most. The recoded singles rate was scaled down so that computer deadtime was kept below 3%.
- Proton attenuation in the various target and detector parts is described in Table. 3.4. It is estimated to be 2.3% in total.

Absorber	Density (g/cm ³)	Thickness (cm)	λ (g/cm ²)	X (g/cm ²)	X/ λ (x 10 ⁻³)
Al Target Window	2.7	0.01	88.5	0.027	0.31
Al Chamber Window	2.7	0.0030	88.5	0.0892	1.01
Kapton (Spectrometer Entrance)	1.42	0.0254	73.1	0.0361	0.49
Titanium (Spectrometer Exit)	4.54	0.01	102.4	0.0461	0.45
Air (Spectrometer Exit to VDC1)	0.00121	80	75	0.0968	1.27
Mylar (Wire Chamber Windows)	1.36	0.012	72	0.0167	0.23
VDC Wires (effective) 20 μ m W)	19.3	0.0004	147.7	0.0008	0.005
Ar/Ethane (62/38 by weight)	0.00107	20	85	0.002114	0.25
Polystyrene (Scintillator S1)	1.03	0.507	70	0.523	7.45
Air (VDC1 to S2)	0.00121	220.2	75	0.0226	3.5
Polystyrene (Scintillator S2)	1.03	0.52	70	0.537	7.650
Total					22.61

Table 3.4: Absorbances of materials in the HRS and target. Values for these materials are taken from [61]. X is the material’s areal density, and λ is the mean free path defined as $\lambda = \frac{\rho}{N_A \sigma}$ where ρ is the density in grams per mole, N_A is Avogadro’s number and σ is the cross section for a scattering event to occur.

3.4.2 Overview of the Systematic Uncertainties

Following the cross section derivation described in this chapter, we can analyze the systematic uncertainty in determining the value of each ingredient. Eq.(3.4)

gives the invariant differential cross section. Uncertainty propagation yields:

$$\frac{\Delta\left(\frac{d\sigma}{dt}\right)}{\frac{d\sigma}{dt}} = \sqrt{\left(\frac{\Delta\left(\frac{d\sigma}{d\Omega_{lab}}\right)}{\frac{d\sigma}{d\Omega_{lab}}}\right)^2 + \left(\frac{\Delta\left(\frac{d\Omega_{lab}}{d\Omega_{cm}}\right)}{\frac{d\Omega_{lab}}{d\Omega_{cm}}}\right)^2 + \left(\frac{\Delta\left(\frac{d\Omega_{cm}}{dt}\right)}{\frac{d\Omega_{cm}}{dt}}\right)^2} \quad (3.38)$$

Following Eq.(3.11) we evaluate the uncertainty of the first term as:

$$\frac{\Delta\left(\frac{d\sigma}{d\Omega_{lab}}\right)}{\frac{d\sigma}{d\Omega_{lab}}} = \sqrt{\left(\frac{\Delta(Y_{\gamma-pp-exp})}{Y_{\gamma-pp-exp}}\right)^2 + \left(\frac{\Delta(Y_{\gamma-pp-MC})}{Y_{\gamma-pp-MC}}\right)^2 + \left(\frac{\Delta(Q_{exp})}{Q_{exp}}\right)^2} \quad (3.39)$$

The electro-disintegration background subtraction for the data points at $E_e = 4.1$ GeV and 4.7 GeV, is done by the extrapolation procedure described in Sec. 3.3.2.

This introduces an additional uncertainty according to Eq. (3.17) in the form of:

$$\frac{\Delta(Y_{\gamma-pp-exp})}{Y_{\gamma-pp-exp}} = \frac{\Delta(\Gamma_{\gamma/e})}{\Gamma_{\gamma/e}} \quad (3.40)$$

According to Eq.(3.21), the uncertainty in the photo-disintegration yield calculated by MCEEP can be expressed as:

$$\frac{\Delta(Y_{\gamma-pp-MC})}{Y_{\gamma-pp-MC}} = \sqrt{\left(\frac{\Delta(f_A)}{f_A}\right)^2 + \left(\frac{\Delta(N_\gamma)}{N_\gamma}\right)^2 + \left(\frac{\Delta(\Delta\Omega)}{\Delta\Omega}\right)^2 + \left(\frac{\Delta(N_{scat})}{N_{scat}}\right)^2} \quad (3.41)$$

where f_A express the simulated acceptance (i.e. the fraction of events that passed the simulation cuts). The uncertainty in the number of scatterers may be calculated according to Eq.(3.6)

$$\frac{\Delta(N_{scat})}{N_{scat}} = \frac{\Delta(\rho)}{\rho} \quad (3.42)$$

The uncertainty in $\frac{d\Omega_{cm}}{dt}$ may be determined according to eq.(3.26):

$$\frac{\Delta\left(\frac{d\Omega_{cm}}{dt}\right)}{\frac{d\Omega_{cm}}{dt}} = \sqrt{\left(\frac{\Delta(E_\gamma)}{E_\gamma}\right)^2 + \left(\frac{\Delta(p_{HRS})}{p_{HRS}}\right)^2} \quad (3.43)$$

A summary of the evaluation of these uncertainties is listed here:

- The value for $\frac{\Delta(Q_{exp})}{Q_{exp}}$ is taken from Ref. [46] to be 0.5%.
- The values of $\frac{\Delta(\Gamma_{\gamma/e})}{\Gamma_{\gamma/e}}$ are taken from Table 3.2.

Photon energy (GeV)	0.8	1.1	1.7	2.1	2.5	3.1	4.1	4.7
Systematic uncertainty in $\frac{d\sigma}{dt}$	10%	5%	5%	5%	6%	6%	7%	7%

Table 3.5: Total systematic uncertainty in the invariant cross section calculation.

- The uncertainty in the bremsstrahlung flux calculation, N_γ is of the order of 3% [56].
- The uncertainty in the HRS solid angle is taken from Ref. [46] to be 2%.
- The uncertainty of in f_A is studied in Sec. 3.4.3. It's value is found to be 3% – 9%.
- The study of $\frac{\Delta(\rho)}{\rho}$ is discussed in Sec. 3.4.4. It's value was found to be 0.6%.
- The HRSs resolutions are taken from [46] as: $\frac{\Delta(p_{HRS})}{p_{HRS}} = 2 \cdot 10^{-4}$ and $\frac{d\theta_{HRS}}{\theta_{HRS}} = 0.033$.
- Mathematica code for the uncertainty propagation of the reconstructed photon energy is shown in Appendix A. The results are $\frac{\Delta(E_\gamma)}{E_\gamma} = 0.02\% - 0.5\%$.

The results of combining all of those uncertainty sources into the differential cross section calculation are listed in Table 3.5. At low energy, the systematic error dominates with the major contribution due to the large number of $\theta_{c.m.} = 90^\circ$ proton pairs not detected by the spectrometers. This acceptance limitation is handled by the simulation, but introduces a larger systematic uncertainty. At high energy the systematic uncertainty is dominated by the ^3He electro-disintegration subtraction (due to the extrapolation from lower energies).

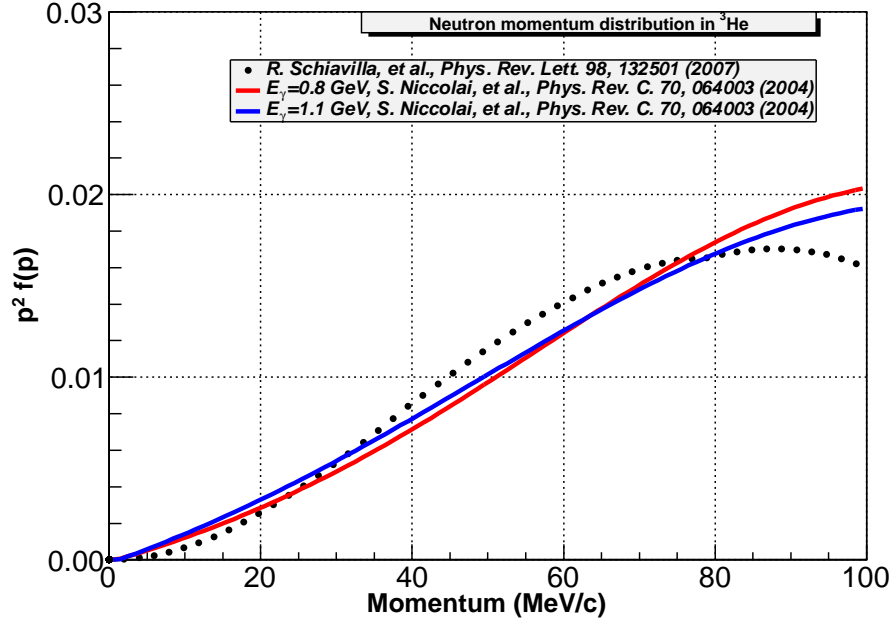


Figure 3.14: Calculated and measured neutron momentum in ${}^3\text{He}$ distribution. The integral of each distribution up to 100 MeV/c are normalized to 1.

3.4.3 The Uncertainty of the Simulated Acceptance

Event generation in MCEEP depends on one input taken from theory: The neutron momentum distribution in ${}^3\text{He}$. The distribution is sampled up to 100 MeV/c³, as described in Sec. 3.3.3, where the ${}^3\text{He}$ wave function is reasonably understood [59]. To evaluate the sensitivity of MCEEP’s yield to this input distribution, we used different momentum distributions for the neutron taken from measured ${}^3\text{He}$ 3-body photo-disintegration of CLAS [62]. The different momentum distributions, up to $p_n = 100$ MeV/c are plotted in Figure 3.14. Running the simulation with these measured distributions yields a 9% difference in yield for $E_e = 0.8$ GeV, and 3% for $E_e = 1.1$ GeV. The sensitivity of MCEEP’s results to the input distribution decreases with energy, due to the kinematic focusing described in Sec. 3.3.1. We use

³The reconstructed neutron momentum resolution in the data is at a 10^{-4} level, therefore we can neglect the uncertainty involved with sampling of the neutron momentum distribution with a poorly identified momentum value.

3% as a conservative evaluation of the uncertainty for all measurements above $E_\gamma = 1.1$ GeV.

As described in Sec. 3.2.3 – 3.2.5, the nominal phase-space cuts were selected to form the largest acceptance in which the calculated cross sections values remain constant. The sensitivity of the MCEEP’s results to variations about these values of choice, were found to be negligible in comparison to the 3% uncertainty described above.

3.4.4 Target Density

The pressure and temperature of the target system were monitored in real time and written to the data stream. The target’s density is evaluated using ^3He equation of state data taken from [63], using the recorded temperature and pressure values as inputs. To estimate the uncertainty in the target density, the following procedure was taken: ^3He density values were taken from [63] also for pressure and temperature values in the vicinity of the experiment’s pressure and temperature values (shown in Fig. 3.15A). These density values were fitted to a quadratic form as a function of temperature and pressure. Fig. 3.15B shows the density for each run which was evaluated from the fit with the recorded temperature and pressure values. Note that the runs with measured pressure $P \sim 189$ psi were taken during a malfunction in the target that caused a pressure drop and were omitted from the analysis. The horizontal clusters results from the discretization of the recorded temperature values. Figure 3.15C shows the density for each run as a function of the run number, the uniform distribution indicates that the target conditions were stable. A histogram of these values is shown in Fig. 3.15D, fitted to a Gaussian. The density value chosen for this analysis and its uncertainty are evaluated from this fit: $\rho = 0.07956 \pm 0.00006$ g/cm³.

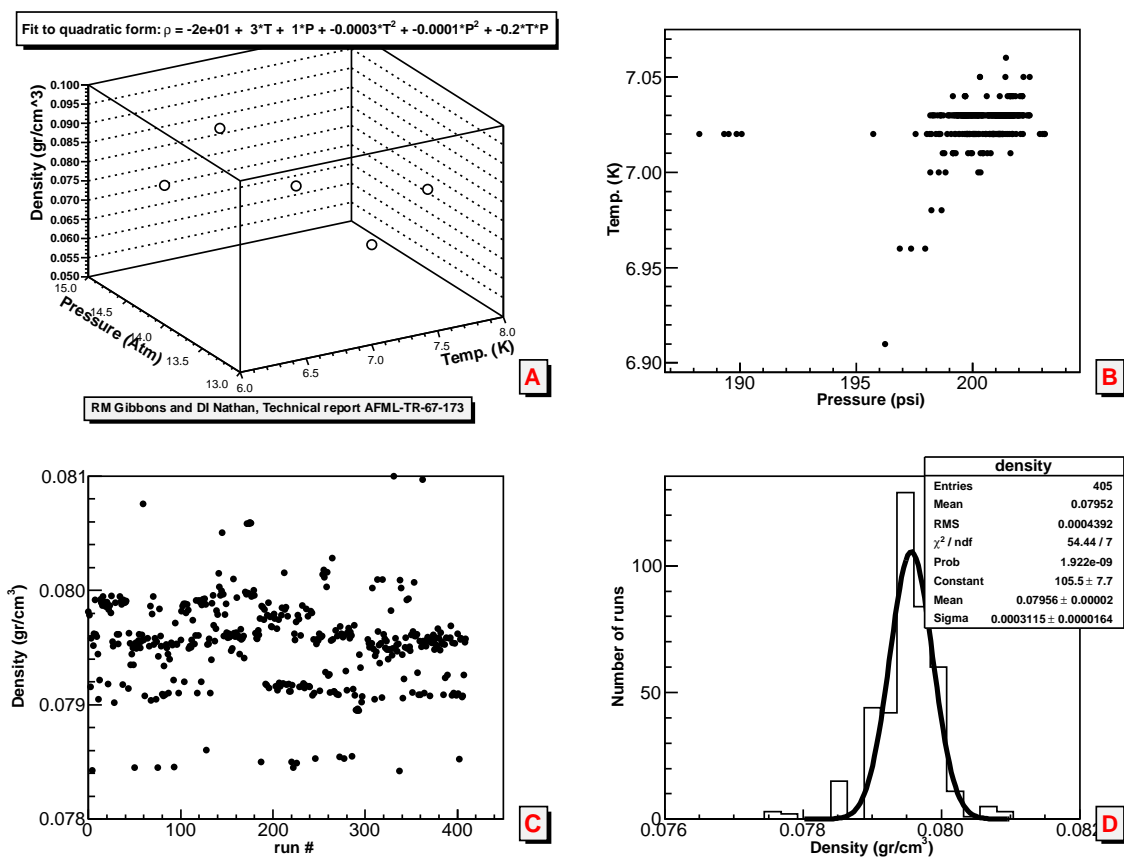


Figure 3.15: Uncertainty in the target density evaluation. (A) Shows the density as a function of temperature and pressure, and the results of a fit to a quadratic form. (B) Shows a scatter plot of the temperature vs. pressure as recorded for each run. (C) Shows the density calculated for each run according to its pressure and temperature, as a function of the run number. (D) Shows a densities distribution for all runs.

CHAPTER 4

Results

4.1 The $\theta_{cm} = 90^\circ$ Differential Cross Section

The $\theta_{cm} = 90^\circ$ invariant cross sections for ${}^3\text{He}(\gamma,pp)n$ with neutron momentum up to 100 MeV/c were calculated as described in Chapter 3. The detector settings are listed in Tab. 4.1. The results are displayed in Table 4.2. For energies up to 2.1 GeV, statistics were high enough to allow binning of the data into two 70 MeV bins in photon energy. Above 2.4 GeV, a single 140 MeV bin is used.

	E_e GeV	p_{HRS} GeV/c	θ_{HRS} deg
1	0.849	0.943	65.32
2	1.075	1.073	62.62
3	1.656	1.453	57.00
4	2.094	1.711	53.69
5	2.461	1.913	51.43
6	3.114	2.275	47.98
7	4.072	2.781	44.11
8	4.711	3.124	41.94

Table 4.1: Kinematic settings used for the ${}^3\text{He}(\gamma,pp)n$ measurements. The HRSs were set symmetrically on both sides of the beam with the same central momentum. The values listed for p_{HRS} and θ_{HRS} are the center values of the HRSs acceptance.

The invariant cross section scaled with s^{11} is plotted in Fig. 4.1. The photo-disintegration of ${}^3\text{He}$ has also been measured with the Hall B/CLAS detector [64] at Jefferson Lab, using tagged photons of 0.35 to 1.55 GeV [62]. The large acceptance of the spectrometer allowed detection of the two outgoing protons over a wide range of momentum and angles. Events corresponding to $\theta_{c.m.} = 90^\circ$ break-up to a

E_γ bin center (GeV)	E_γ bin width (MeV)	$Y_{\gamma-pp}$	$\frac{d\sigma}{d\Omega_{lab}}$ ($\frac{nb}{sr}$)	$\frac{d\Omega_{lab}}{d\Omega_{cm}}$	$\frac{d\Omega_{cm}}{dt}$ ($\frac{sr}{GeV^2}$)	$\frac{d\sigma}{dt}$ ($\frac{nb}{GeV^2}$)	$s^{11} \frac{d\sigma}{dt}$ (kb GeV ²⁰)
0.744	70	15600	10.7	0.786	6.57	55.4	0.0502 ± 0.000402
0.814	70	25700	13.6	0.785	6.16	65.6	0.0595 ± 0.000371
0.97	70	6260	3.66	0.748	4.85	13.3	0.0693 ± 0.000876
1.04	70	1570	4.52	0.746	4.55	15.3	0.0801 ± 0.00202
1.55	70	4270	0.544	0.663	2.74	0.989	0.0883 ± 0.00135
1.62	70	2380	0.528	0.661	2.62	0.915	0.0817 ± 0.00168
1.99	70	277	0.0988	0.612	2.05	0.124	0.0523 ± 0.00314
2.06	70	120	0.0716	0.609	1.97	0.0858	0.0362 ± 0.00331
2.39	140	110	0.00577	0.574	1.68	0.00557	0.00916 ± 0.000873
3.04	140	60	0.00178	0.522	1.27	0.00118	0.0114 ± 0.00147
4.00	140	12	0.000317	0.453	0.935	0.000134	0.0148 ± 0.00423
4.64	140	2	7.22e-05	0.427	0.787	2.43e-05	0.00921 ± 0.00588

Table 4.2: The invariant cross section for ${}^3\text{He}(\gamma,pp)n$ at $\theta_{cm} = 90^\circ$. $Y_{\gamma-pp}$ is the yield after electro-disintegration background subtraction. $s^{11} \frac{d\sigma}{dt}$ is scaled with the average value of s for all events in the bin. The uncertainties in $s^{11} \frac{d\Omega_{cm}}{dt}$ are statistical only.

proton pair were selected with various cuts on neutron momentum. Preliminary yet unpublished single differential cross-section results from CLAS [65] are also shown in the Figure.

The RNA and QGS model predictions are plotted as they appear in [29] divided by 200 and 5 respectively to be shown with the selected scale. The HRM curve is taken from an updated calculation [66] published after our data was available.

4.2 Comparison with World Data and Theory

Our new data along with previous low-energy data indicate that the ${}^3\text{He}$ two-proton disintegration can be divided into three energy regions. A *low* photon energies region (below $E_\gamma \approx 1$ GeV), where the dynamics is governed by hadron and meson degrees of freedom. A *transition* region ($1 \text{ GeV} < E_\gamma < 2.2 \text{ GeV}$)

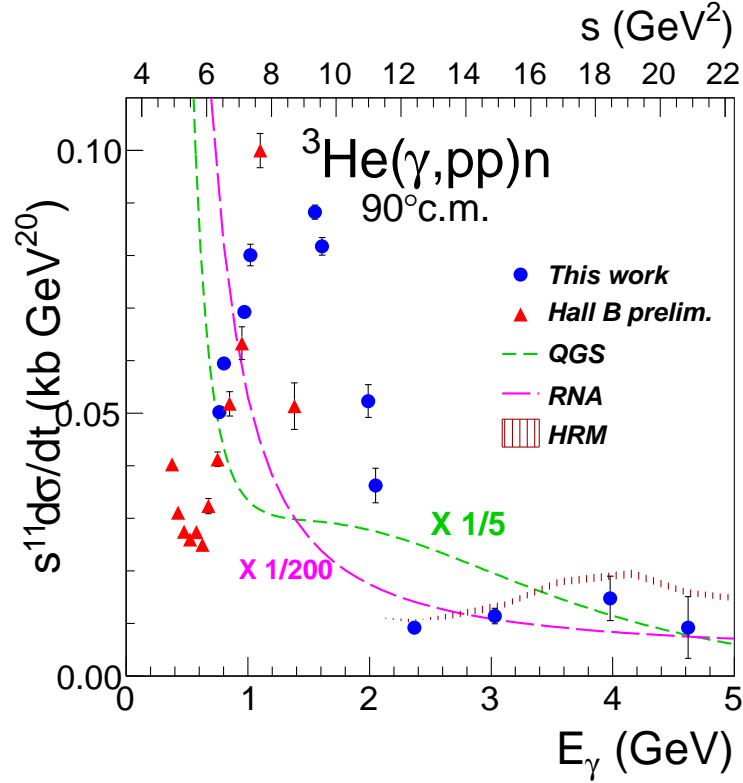


Figure 4.1: Invariant cross section scaled by s^{11} for ${}^3\text{He}(\gamma, pp)n$. The ${}^3\text{He}(\gamma, pp)n$ events were selected with $p_n < 100$ MeV/c. Up to 2.1 GeV, the photon energy bins are 70 MeV, and above 140 MeV. Only the statistical uncertainties are shown. The preliminary Hall B/CLAS data are taken from [65]. Model predictions are from [29, 66]. RNA is divided by a factor of 200 and QGS by a factor of 5 to be shown on this scale.

where the scaled cross section for deuteron (pn pairs) breakup is flat while for pp pairs from ${}^3\text{He}$ a significant structure is observed. A *scaling* region (above $E_\gamma \approx 2.2$ GeV) where the cross section for both deuteron (pn) and pp breakup scales in agreement with the constituent counting rule [1, 26, 27]. In the following sections, we will discuss each region in detail.

4.2.1 Low Energy pp Breakup

Our lowest energy ${}^3\text{He}(\gamma, pp)n$ measurement is at $E_\gamma = 0.8$ GeV. The data are extended down to ~ 0.3 GeV by CLAS [65] and further down to ~ 0.2 GeV by older measurements from Saclay [67]. Figure 4.2 shows the Saclay data with

calculations [68] for the pp and pn breakup cross sections. The pp to pn cross section ratio is about 1%. The low energy dynamics is governed by meson exchange,

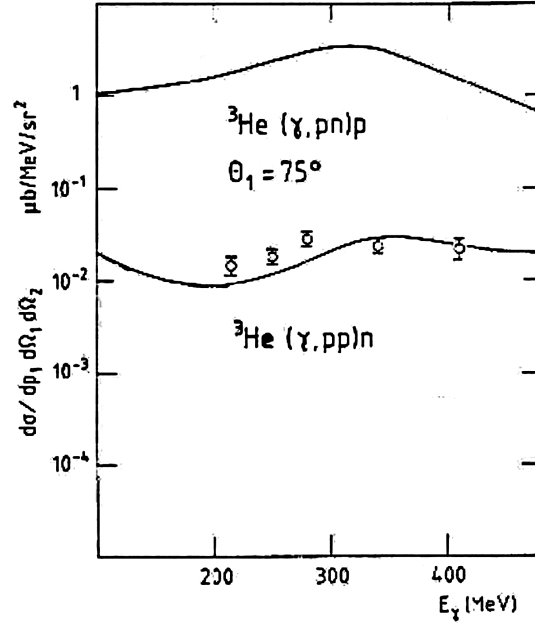


Figure 4.2: The ${}^3\text{He}$ photodisintegration cross sections of a pn pair (upper) and pp pair (lower) [69]. The full line curves are calculation including three-body mechanisms.

schematically illustrated in Fig. 4.3. The low cross section ratio is explained by two-body mechanisms which contribute to pn breakup but are suppressed for pp due to the following considerations:

- A pp pair has no dipole moment to couple with,
- the charge-exchange currents are neutral for pp and their contribution is small compared with those of np ,
- the formation of Δ as an intermediate state is forbidden, since the $J^\pi = 1^+ p\Delta^+$ S-wave cannot decay to the pp channel.

4.2.2 Transition Region

The structure observed at $1 \text{ GeV} < E_\gamma < 2.2 \text{ GeV}$ may be the result of resonances in the γN or γNN systems. The energy dependence in the transition

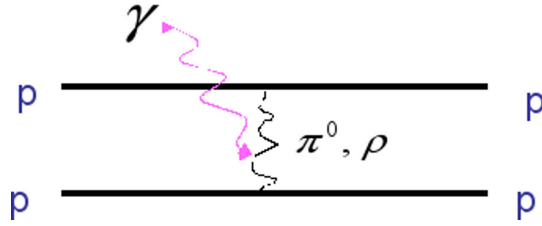


Figure 4.3: A diagram illustration of pp photodisintegration by neutral meson exchange.

region more closely resembles the energy behavior of the photo-induced pion production [70–72]. As can be seen in Fig. 4.4, the scaled differential cross section for $\gamma n \rightarrow \pi^- p$ (which scales with s^{-7}) presents a wide “bump” before the onset of scaling, same as in our data. It has been suggested that the structure might result from a meson photo-produced on a proton and then absorbed on a pn pair [73].

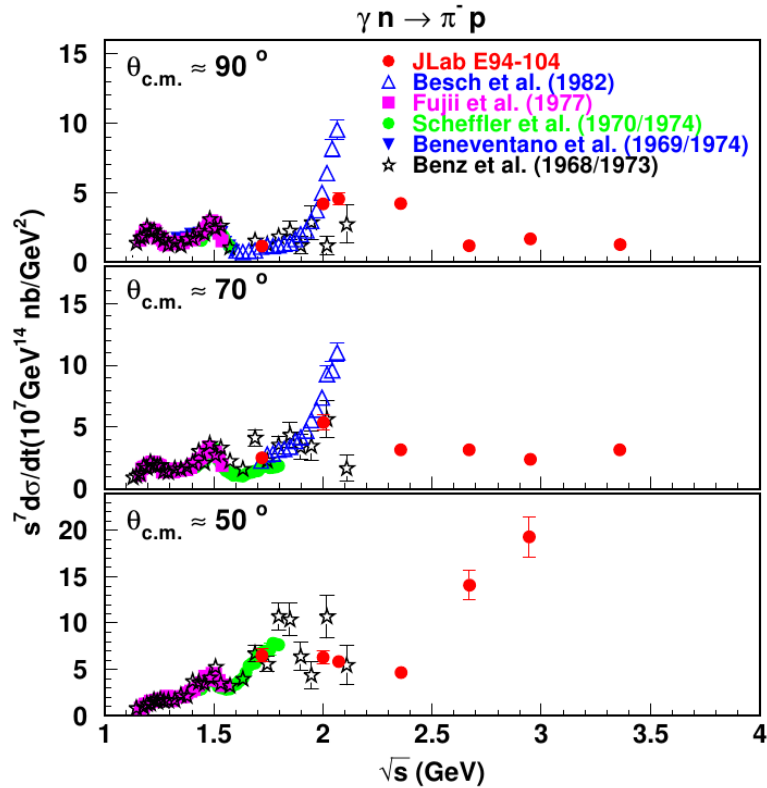


Figure 4.4: $\gamma n \rightarrow \pi^- p$ scaled differential cross section $s^7 \frac{d\sigma}{dt}$ versus center of mass energy \sqrt{s} from [72].

4.2.3 Scaling Region

For $\theta_{c.m.} = 90^\circ$ proton-pair breakup, the onset of scaling is at $E_\gamma \approx 2.2$ GeV, while for deuteron (pn pair) scaling commences at $E_\gamma \approx 1$ GeV [14]. The scaling in the ${}^3\text{He}$ case indicates that in this regime the two-body process is dominant. It further suggests (in a relatively model-independent way) that the relevant degrees of freedom that govern the dynamics are quarks. In a hadronic picture, two-body/one-step processes are strongly suppressed since no charge can be exchanged between the protons.

The reduced nuclear amplitude (RNA) formalism [30] after normalization to the deuteron data [29] yields cross sections that are about 200 times larger than the present data. The quark-gluon string model (QGS) [35, 74], as estimated in [29], predicts cross sections about a factor of 5 larger than measured. The QCD hard re-scattering model (HRM) [36] allows an absolute calculation of the cross sections for both pn and pp pair photodisintegration from nucleon-nucleon measured cross sections without adjustable parameters. It reproduces reasonably well the deuteron data and the proton pair cross section.

An explanation for the low magnitude of the scaled cross section of proton-pair breakup is given in the HRM [66] by a cancellation caused by opposite sign of the NN helicity amplitudes ϕ_3 and ϕ_4 in the pp breakup ¹. The energy dependence predicted by the HRM in the scaling region agrees well with the data. Therefore, hard re-scattering is a plausible explanation for the origin of the large transverse momenta. The amount of pp pairs produced in a spectator neutron kinematics by a three-body/two-step processes is evaluated in [66] to be 2% of the number of two-body re-scattered proton pairs. Models that hold compact NN pairs in the initial state to be the reason for the large transverse momenta [30] would have to assume

¹ ϕ_3 and ϕ_4 are the NN elastic scattering helicity amplitudes that connect zero helicity in the initial states to zero helicity in the final state. ϕ_3 does it with no helicity exchange. ϕ_4 exchanges helicity between the scattered nucleons. This cancellation of ϕ_3 and ϕ_4 was not recognized in [29].

either a fairly low abundance of pp pairs within the ${}^3\text{He}$ wave function or the same type of nuclear amplitude cancellation in order to explain the low magnitude of the pp break-up scaled cross section.

Another possible explanation for the cross-section magnitude may lie in tensor correlations [59, 75, 76]. These nucleon-nucleon correlations cause the ratio of pp to np pairs to be $\sim 5\%$ in the relative momentum range of 300-600 MeV/ c for both high-energy electron and proton scattering [77–79]. Starting with such a pair and final state re-scattering might lead to the observed relative transverse momentum and would explain the relatively small cross sections.

4.3 Outlook

The results presented in this chapter, along with the Deuteron photo-disintegration data of previous experiments [9–16], indicate unambiguously the onset of quark-constituent dynamics in the hard photodisintegration process, making it one of the few nuclear reactions which lies beyond the limits of description within the meson-baryon framework of strong interactions.

The existing data and theory, however, are insufficient to determine if the large transverse momentum final state nucleons are due to break-up of a pre-existing, highly correlated, two-baryon system, or if they are formed due to hard scattering in the final state of the reaction. Identifying the source of the large transverse momentum nucleons from nuclei is the main motivation for the next generation of hard-break-up experiments.

These experiments will envision comparative studies of pn and pp breakup from the $A = 3$ nucleus, measurement of light-cone and transverse momentum distribution of the center of mass of the two large- p_T nucleons, extension of the measurements to large energies, and probing different polarization observables of hard photodisintegration. A new generation of experiments will extend the measurements to hard-

photodisintegration of two nucleons into two non-nucleonic baryons as well as to the virtual photon sector, which can be used for reconstruction of the impact-parameter picture of the hard break-up processes.

As a first step in this process, we proposed a new JLab experiment [80], in which we intend to extend our recent measurements. In particular, we propose comparative measurements of pp and pn photodisintegration of ${}^3\text{He}$ at large center of mass angles, with identification of the third low-momentum nucleon as a spectator to the hard reaction. Within this setup we propose to carry out:

1. Measurement of the light-cone (α_n) momentum distribution as a function of the transverse momentum (p_{Tn}) of the spectator neutron and as a function of the transverse momentum (p_{Tp}) (or equivalently c.m. angle) of the proton in the hard ${}^3\text{He}(\gamma, pp)n$ photodisintegration reaction. These measurements will enable us to determine whether the high transverse momentum originates from *initial-state correlations* or *final-state hard rescattering*, and how this distribution varies with kinematics.
2. Measurements of the cross sections of both $\gamma{}^3\text{He} \rightarrow pp(n)$ and $\gamma{}^3\text{He} \rightarrow pn(p)$ reactions will address the issue of the small measured cross section ratio of $\gamma{}^3\text{He} \rightarrow pp(n)$ to $\gamma d \rightarrow pn$. The understanding of the source of this suppression will provide additional constraints on the determination of the origin of high- p_T nucleons in the photodisintegration process.

CHAPTER 5

The Two-Body Breakup of ${}^3\text{He}$ into a Proton-Deuteron Pair

5.1 Overview

The primary objective of Experiment E03-101 was to measure the $\theta_{c.m.} = 90^\circ$ energy dependence of the ${}^3\text{He}(\gamma, pp)n_{spectator}$ reaction [17]. At an incident energy of 1.656 GeV we also took data at two kinematical setups which did not match the $\theta_{c.m.} = 90^\circ$ conditions for that reaction. In these two kinematics, listed in Tab. 5.1, we could identify two-body photodisintegration of the ${}^3\text{He}$ into a proton and a deuteron at angles corresponding to $\theta_{p.c.m.} = 85^\circ$. Figure 5.1 shows the mass distribution of the two particles detected in coincidence, normalized by m_p . One clearly sees proton and deuterons in coincidence, with no visible background. In this chapter we review the analysis of this reaction.

	E_e	p_{HRS}	θ_{HRS}
	GeV	GeV/c	deg
1	1.655	1.421	63.16
2	1.656	1.387	65.82

Table 5.1: Kinematic settings used for the ${}^3\text{He}(\gamma, pd)$ measurements. The HRSs were set symmetrically on both sides of the beam with equal central momentum settings. The values listed for p_{HRS} and θ_{HRS} are the center values of the HRSs acceptance.

5.2 Experimental Setup and Data analysis

Protons and deuterons from the target were detected in coincidence using the HRSs with the method described in Chapter 2. The two spectrometers were set

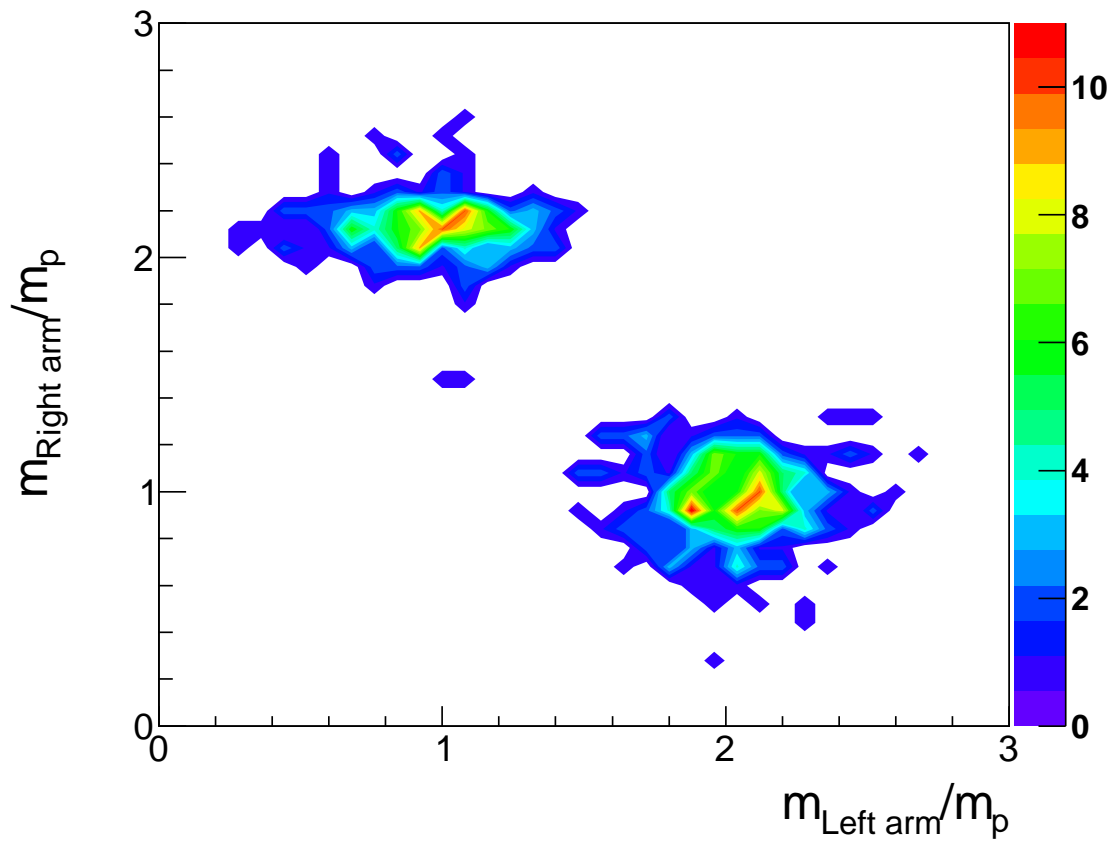


Figure 5.1: The mass distribution of particles detected in coincidence by the two HRS, normalized by the proton's mass, m_p .

symmetrically on the two sides of the beam line in two kinematical settings corresponding to central momenta of 1.421 GeV/ c at a laboratory scattering angle of 63.16° and 1.389 GeV/ c at a scattering angle of 65.82°.

The incident photon energy was reconstructed event by event from the momentum and angles of the scattered particles under the assumption of two-body pd final-state kinematics. In order to assure the validity of this assumption and reduce backgrounds from pion producing reactions, the analysis is limited to events that fulfill two energy and momentum constraints:

1. $p_{T\text{ missing}} \equiv p_{T(p)} + p_{T(d)} < 5 \text{ MeV}/c$
2. $\alpha_{\text{missing}} \equiv \alpha_d + \alpha_p - \alpha_{3\text{He}} - \alpha_\gamma < 5 \cdot 10^{-3}$

We use here the light-cone variable α defined as:

$$\alpha = A \frac{E^N - p_z^N}{E^A - p_z^A} \approx \frac{E_N - p_z^N}{m_N}, \quad (5.1)$$

where E^N and p^N are the nucleon's energy and momentum respectively, E^A and p^A are the nuclei energy and momentum, and the z direction is the direction of the incident photon beam. With the above definitions, α for the incident photon is zero, while α for the ^3He target is 3.

A simulation was used to evaluate the experimental acceptance for events where an extra pion is produced using the cuts specified above. The results, presented in Fig. 5.2, shows that the amount of accepted $\gamma^3\text{He} \rightarrow pd\pi$ (background) events is negligible compared to the accepted $\gamma^3\text{He} \rightarrow pd$ (signal) events (accepted ratio $\sim 1\%$).

We also took data with the radiator out of the beam, and extracted the electro-produced pd background using the method described in Sec. 3.3.2.

Event selection cuts on the target vertex and coincidence between the two spectrometers were applied using the procedure described in Sec. 3.2.1 and 3.2.4.

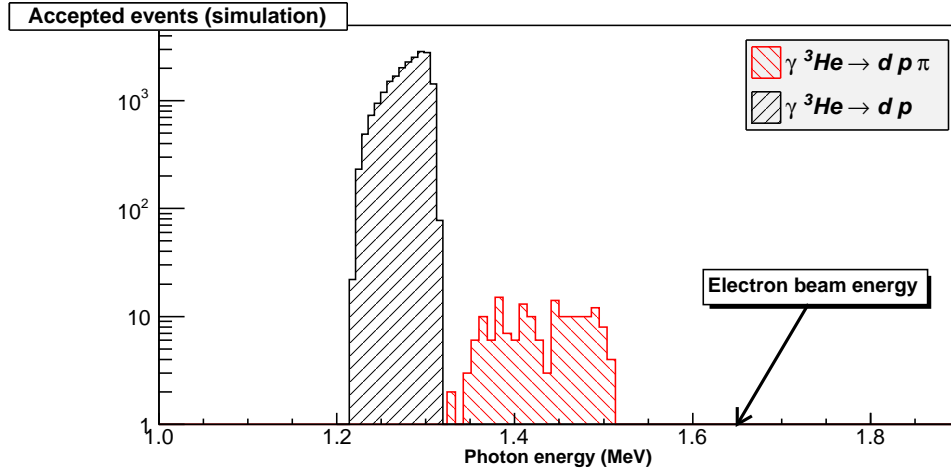


Figure 5.2: Simulated detection acceptance of a proton and a deuteron in coincidence plotted as a function of the photon energy, for $\gamma^3\text{He} \rightarrow pd$ and $\gamma^3\text{He} \rightarrow pd\pi$. The detector settings and the applied cuts for the analysis are described in the text. The acceptance ratio $\frac{\gamma^3\text{He} \rightarrow pd\pi}{\gamma^3\text{He} \rightarrow pd}$ is 1.2 %.

The finite acceptance correction was determined using the standard Hall A Monte-Carlo simulation software MCEEP [57] as described in Sec 3.3.3. The sources for the systematic uncertainties for E03-101 are described in Sec. 3.4.2.

5.3 Experiment E93-044 in Hall B

The experiment E93-044 in Hall B at Jefferson Lab used the CEBAF Large Acceptance Spectrometer (CLAS) to measure various photoproduction reactions on ^3He and ^4He targets. A collimated, tagged, real-photon beam was produced using the bremsstrahlung tagging facility in Hall B [81]. Photons with energies between 0.35 and 1.55 GeV were incident on 18-cm long cryogenic ^3He target positioned in the center of CLAS. The outgoing protons and deuterons were tracked in the six toroidal magnetic spectrometers (sectors) of CLAS. Their trajectories were measured by three layers of drift chambers surrounding the target. The particles' time of flight was measured by 6×48 scintillators (TOF) enclosing CLAS outside of the magnetic field. CLAS covers a polar angular range from 8° to 142° and the nearly the entire range in azimuthal angle. More details about CLAS and experiment E93-044 can

be found in [64] and [62], respectively.

In the analysis of data from E93-044, events with exactly two positively-charged tracks were considered only. The mass of the particle producing the track was obtained from momentum and time-of-flight measurements and was used to identify the particle as either a proton or deuteron. Only events with a proton and a deuteron were used for further analysis. Both particles must have originated from the target and been detected within the fiducial volume of CLAS. Remaining accidental and physics background were further reduced by applying kinematic cuts making use of the constraints provided by two-body kinematics when both final-state particles are detected. For example, the c.m. momenta of the proton and deuteron had to be consistent with each other within the detector resolution, the z -component of the beam momentum had to match the z -component of the total momentum in the final state, the c.m. angles of the deuteron and the proton had to add up to $\sim 180^\circ$, *etc.* A detailed discussion of the selection cuts can be found in [82]. Figure 5.3 demonstrates the effect of the kinematic cuts on the proton missing-mass-squared distribution at proton c.m. angle of 90° . Event distributions with and without the kinematic cuts are shown. The background distribution is smooth outside of the peak which allow to extract a reliable estimate to its amount over the deuteron peak. We estimate an uncertainty of the yield extraction due to background events as $(2.30 \pm 0.63)\%$ and an uncertainty due to good events rejected by our selection cuts as $(0.331 \pm 0.035)\%$. CLAS acceptance for the reaction $\gamma^3\text{He} \rightarrow pd$ was evaluated by generating 2×10^7 phase-space events and processing them with GSIM [83], a GEANT-3 program that simulates CLAS. The simulated data were then analyzed with the same analysis software as the real data. Selection cuts based on the same criteria used for the real data, were determined and applied. CLAS acceptance for pd events at c.m. angle of 90° is $\sim 71\%$. We estimated the uncertainty of CLAS acceptance to be $< 10\%$. The photon flux was calculated using the standard CLAS

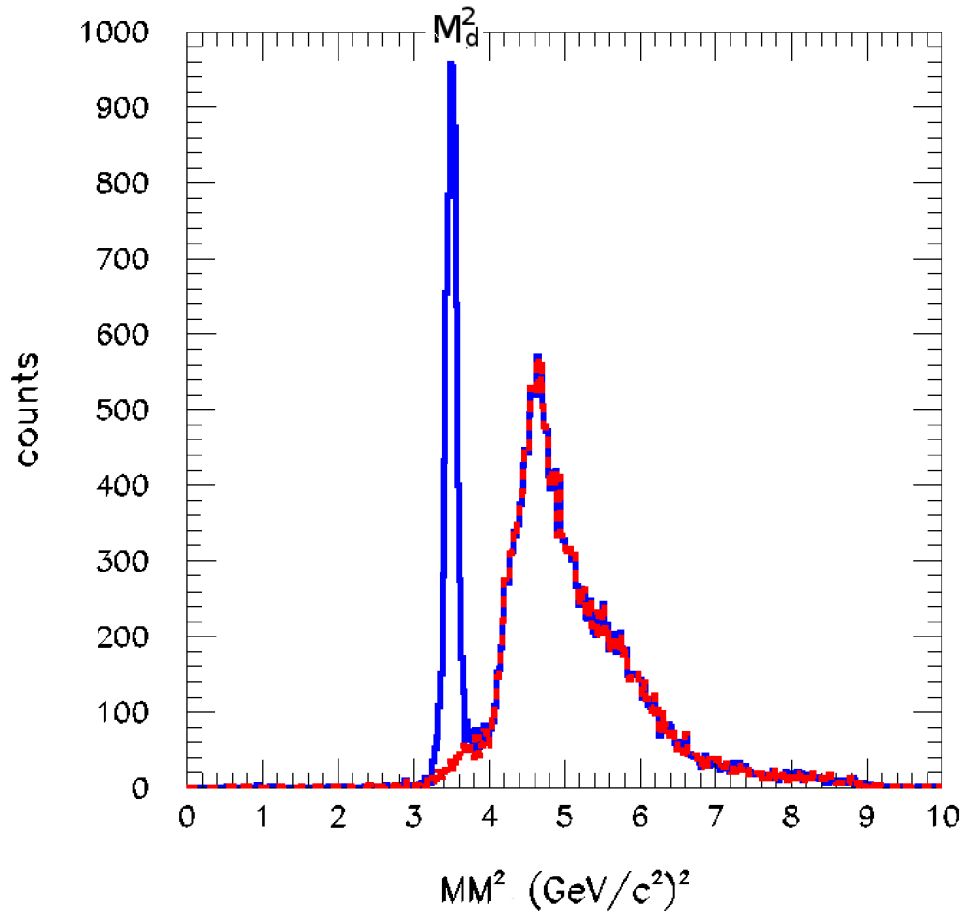


Figure 5.3: Event distributions of the ${}^3\text{He}(\gamma,p)d$ missing-mass reconstructed from the detected proton, MM^2 for proton detected at c.m. angle of 90° with the kinematic cuts (solid blue line), over the background (dashed red line). Events from pd final state are clearly identified as the peak. Accidental and multi-pion events give rise to smooth background under the deuteron peak that can be estimated by the background shape outside of the peak.

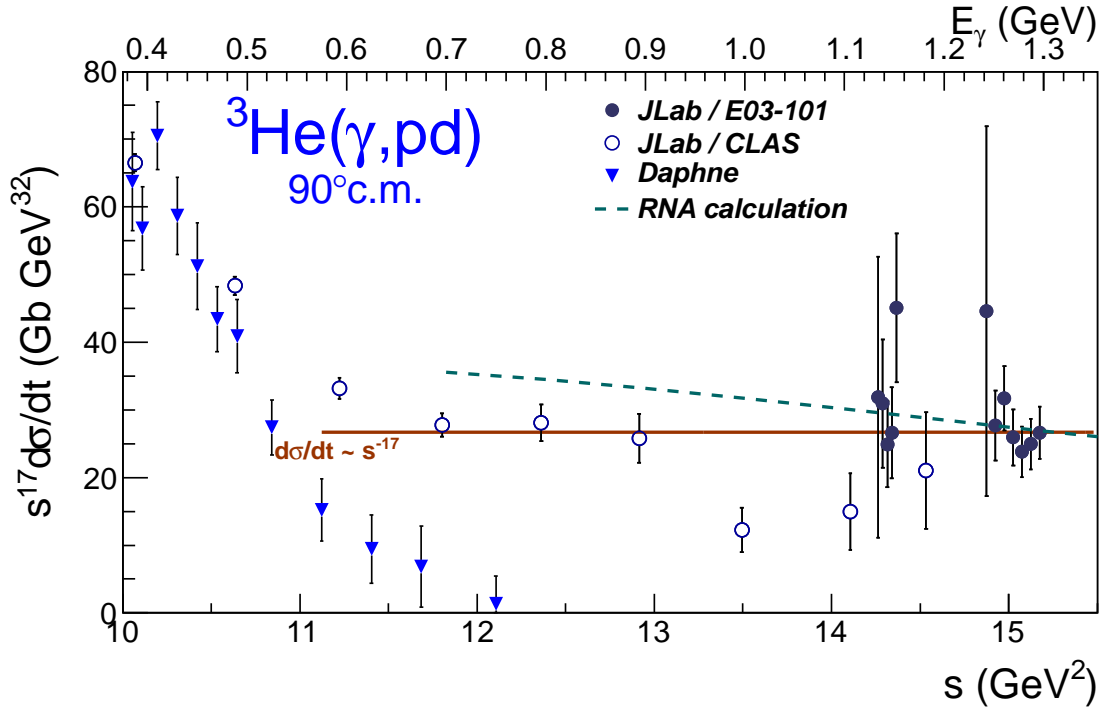


Figure 5.4: The invariant cross section $d\sigma/dt$ multiplied by s^{17} to remove the expected energy dependence. The DAPHNE data is taken from [87].

software [84]. The uncertainty of the photon flux was determined to be 4.5% [85]. The uncertainty of the target length and density is 2% [62]. The uncertainty of fiducial cuts was estimated to be negligible [86]. The total systematic uncertainty of CLAS cross sections is $< 11.2\%$. The statistical uncertainties range from 2% to 40% for different energy bins.

5.4 Results and Discussion

Figure 5.4 shows the measured cross sections from JLab Halls A and B compared to previously published data [87] for $s > 10 \text{ GeV}^2$. Above $s = 11.5 \text{ GeV}^2$, the consistency of the scaled cross sections with being constant can be seen. In the range of $s = 11.5 - 15 \text{ GeV}^2$, the cross section falls by two orders of magnitude. The falloff of both data sets in this range is fit as $s^{-17 \pm 1}$, which is consistent with

the expected scaling value of $n = -17$. This is the first observation of a high-energy cross section scaling for an $A > 2$ system. CLAS data at other kinematics show indications that in the energy range above 0.7 GeV the quark-counting scaling may also be obeyed at other c.m. angles.

Starting at threshold, the scaled invariant cross section decreases smoothly to 0.7 GeV where it levels out, a transition not similar to meson photoproduction [8] or pp breakup [17], where "resonance"-like structures are observed. Since our data are taken in the resonance region, this suggests that two- and three nucleon mechanisms dominate the reaction dynamics or resonance contributions are strongly suppressed.

The scaled cross section of $\sim 30 \text{ Gb} \cdot \text{GeV}^{32}$ for $\gamma \text{ } ^3\text{He} \rightarrow pd$ corresponds to an invariant cross section of $d\sigma/dt \sim 0.4 \text{ nb/GeV}^2$ for $E_\gamma \sim 1.3 \text{ GeV}$. The corresponding cross section for $\gamma d \rightarrow pn$ at this energy is about 30 nb/GeV^2 , i.e. about two orders of magnitude larger, while the scaled cross section for $\gamma \text{ } ^3\text{He} \rightarrow pp + n_{\text{spectator}}$ at this energy is about 13 nb/GeV^2 , i.e. about 30 times larger. If one adopts the view that large momentum transfer reactions select initial states in which all the quarks and nucleons are close together, it is much more likely that there is a short-range, and thus high-momentum, pn pair than pp pair. This is what has been found in recent studies for nucleons above the Fermi surface that have momenta of several hundred MeV/c [78, 79].

The reduced nuclear amplitudes (RNA) prescription [30] was developed as a way of extending the applicability of pQCD to lower energy and momentum scales, by factoring out non-perturbative dynamics related to hadron structure through phenomenologically determined hadronic form factors. The RNA prescription for $\gamma \text{ } ^3\text{He} \rightarrow pd$ is:

$$\frac{d\sigma}{dt} \propto \frac{1}{(s - m_{^3\text{He}}^2)^2} F_p^2(\hat{t}_p) F_d^2(\hat{t}_d) \frac{1}{p_T^2} f^2(\theta_{c.m.}). \quad (5.2)$$

Here p_T is the transverse component of the proton momentum, F_p (F_d) is the proton

(deuteron) form factor, \hat{t}_p (\hat{t}_d) is the momentum transfer to the proton (deuteron) and f is an unknown function of the c.m. angle that must be determined from experimental data. The overall normalization is unknown, and ideally should be determined from data at asymptotically large momentum transfer. Figure 5.4 shows the RNA prediction normalized to our highest energy data point as a dashed line. It should be noted that deuteron photodisintegration follows the dimensional scaling better than it follows the RNA prediction.

If the reaction dynamics is dominated by rescattering, it appears that hard pn rescattering is more likely than hard pp rescattering – which is known to be the case due to cancellations in the pp amplitude [66]. The hard pd rescattering is also suppressed, presumably due to the likelihood of breaking up the deuteron in a hard scattering and the small probability of a pickup reaction that create a deuteron from a scattered proton or neutron. Calculation of the cross section in the framework of the Hard Rescattering Model (HRM) [36] using elastic pd scattering data is in preparation [88].

The momentum transfer to the deuteron and the transverse momentum, at which we observe the onset of scaling in the 90° cross sections, is $|t| > 0.64 \text{ (GeV}/c)^2$ and $p_\perp > 0.95 \text{ GeV}/c$, respectively. For other processes, such as deuteron photodisintegration, the onset of scaling has been observed at $p_\perp > 1.1 \text{ GeV}/c$. The deuteron form factor show scaling at $|t| > 1 \text{ (GeV}/c)^2$. This comparison suggests that non-perturbative interpretation of our data may be more appropriate. Such interpretation in the framework of AdS/CFT means that the observed scaling is due to the near constancy of the effective QCD coupling at low Q (“conformal window” [89]) and the data are in the non-perturbative regime of QCD. A further test of this interpretation would require data for this process over a higher-energy range where the transition from non-perturbative to perturbative dynamics would manifest itself in breaking the quark-counting scaling. The latter would be observed

again at asymptotically large invariants when pQCD sets in.

APPENDIX A

Reconstructed photon energy resolution

The following Mathematica code describes the uncertainty propagation for the photon energy reconstruction (Eq. 3.2). The HRSs resolutions are taken from [46] to be: $\frac{dp}{p} = 2 \cdot 10^{-4}$ and $\frac{d\theta}{\theta} = 0.033$.

(* Calculate total energy from momentum and mass *)

$T[p_, m_] := \text{Sqrt}[p^2 + m^2];$

(* Kinematic settings for the data points *)

$Ee[0] = 0.8; p[0] = 0.9433; th[0] = \text{Pi} * 65.32/180.0;$

$Ee[1] = 1.1; p[1] = 1.01; th[1] = \text{Pi} * 62.62/180.0;$

$Ee[2] = 1.7; p[2] = 1.4530; th[2] = \text{Pi} * 57.00/180.0;$

$Ee[3] = 2.1; p[3] = 1.7109; th[3] = \text{Pi} * 53.69/180.0;$

$Ee[4] = 2.5; p[4] = 1.9133; th[4] = \text{Pi} * 51.43/180.0;$

$Ee[5] = 3.1; p[5] = 2.2746; th[5] = \text{Pi} * 47.98/180.0;$

$Ee[6] = 4.1; p[6] = 2.781; th[6] = \text{Pi} * 44.11/180.0;$

$Ee[7] = 4.7; p[7] = 3.1238; th[7] = \text{Pi} * 41.94/180.0;$

$dp = 0.0002;$

$dth = 0.033;$

(* Define gamma energy function *)

$eGamma[vP1_, vP2_, vth1_, vth2_] :=$

$(1/2)*$

$(M3He * M3He$

$- 2 * M3He * (T[vP1, Mp] + T[vP2, Mp]) + 2 * Mp * Mp + 2 * T[vP1, Mp] * T[vP2, Mp] -$

```

2 * (vP1 * vP2) * Cos[vth1 + vth2] - Mn * Mn)
/(T[vP1, Mp] + T[vP2, Mp] - vP1 * Cos[vth1] - vP2 * Cos[vth2] - M3He);
(* Propagate *)
eGammaErr[vP1_, vP2_, vth1_, vth2_] := Sqrt[
(D[eGamma[vP1, vP2, vth1, vth2], vP1] * dP1)^2 +
(D[eGamma[vP1, vP2, vth1, vth2], vP2] * dP2)^2 +
(D[eGamma[vP1, vP2, vth1, vth2], vth1] * dth1)^2 +
(D[eGamma[vP1, vP2, vth1, vth2], vth2] * dth2)^2
]
(* Relative uncertainty *)
eGammaErr[vP1, vP2, vth1, vth1]/eGamma[vP1, vP2, vth1, vth1];
(* Substitute *)
%/ .M3He -> 2.813882/.Mp -> 0.938272 /.Mn -> 0.939565;
For[i = 0, i < 8, i++,
Print["Ee=", Ee[i], " GeV, ΔEγ/Eγ=",
%/ .vP1 -> p[i]
/.vP2 -> p[i]
/.vth1 -> th[i]
/.vth2 -> th[i]
/.dP1 -> p[i] * dp
/.dP2 -> p[i] * dp
/.dth1 -> th[i] * dth
/.dth2 -> th[i] * dth]]
Ee=0.8 GeV, ΔEγ/Eγ=0.000276681
Ee=1.1 GeV, ΔEγ/Eγ=0.00473882
Ee=1.7 GeV, ΔEγ/Eγ=0.000274584
Ee=2.1 GeV, ΔEγ/Eγ=0.000245869

```

$E_e=2.5 \text{ GeV}, \Delta E_\gamma/E_\gamma=0.000228988$

$E_e=3.1 \text{ GeV}, \Delta E_\gamma/E_\gamma=0.000207792$

$E_e=4.1 \text{ GeV}, \Delta E_\gamma/E_\gamma=0.000203337$

$E_e=4.7 \text{ GeV}, \Delta E_\gamma/E_\gamma=0.000191126$

BIBLIOGRAPHY

- [1] Stanley J. Brodsky and Glennys R. Farrar. Scaling Laws at Large Transverse Momentum. *Phys. Rev. Lett.*, 31:1153–1156, 1973.
- [2] V. A. Matveev, R. M. Muradian, and A. N. Tavkhelidze. Automodellism in the large - angle elastic scattering and structure of hadrons. *Nuovo Cim. Lett.*, 7:719–723, 1973.
- [3] Archibald W. Hendry. Evidence for coherent effects in large-angle hadron-hadron scattering. *Phys. Rev. D*, 10(7):2300–2303, Oct 1974.
- [4] K. A. Jenkins et al. Measurement of wide-angle elastic scattering of pions and protons off protons. *Phys. Rev.*, D21(9):2445–2496, 1980.
- [5] A. Danagoulian et al. Compton-scattering cross section on the proton at high momentum transfer. *Phys. Rev. Lett.*, 98(15):152001, Apr 2007.
- [6] M. Battaglieri et al. Photoproduction of the ρ^0 Meson on the Proton at Large Momentum Transfer. *Phys. Rev. Lett.*, 87(17):172002, 2001.
- [7] Gerald A. Miller. Handling the handbag diagram in compton scattering on the proton. *Phys. Rev. C*, 69(5):052201, May 2004.
- [8] L. Y. Zhu et al. Cross-section measurement of charged-pion photoproduction from hydrogen and deuterium. *Phys. Rev. Lett.*, 91(2):022003, 2003.
- [9] J. Napolitano et al. Measurement of the differential cross-section for the reaction $H-2(\gamma, p)n$ at high photon energies and θ (c.m.)= 90-degrees. *Phys. Rev. Lett.*, 61:2530–2533, 1988.
- [10] S. J. Freedman et al. Two-body disintegration of the deuteron with 0.8-GeV to 1.8-GeV photons. *Phys. Rev.*, C48:1864–1878, 1993.
- [11] J. E. Belz et al. Two body photodisintegration of the deuteron up to 2.8- GeV. *Phys. Rev. Lett.*, 74:646–649, 1995.
- [12] C. Bochna et al. Measurements of deuteron photodisintegration up to 4.0- GeV. *Phys. Rev. Lett.*, 81:4576–4579, 1998.

- [13] E. C. Schulte et al. Measurement of the high energy two-body deuteron photodisintegration differential cross-section. *Phys. Rev. Lett.*, 87:102302, 2001.
- [14] E. C. Schulte et al. High energy angular distribution measurements of the exclusive deuteron photodisintegration reaction. *Phys. Rev.*, C66:042201, 2002.
- [15] M. Mirazita et al. Complete angular distribution measurements of two-body deuteron photodisintegration between 0.5-GeV and 3-GeV. *Phys. Rev.*, C70:014005, 2004.
- [16] P. Rossi et al. Onset of asymptotic scaling in deuteron photodisintegration. *Phys. Rev. Lett.*, 94:012301, 2005.
- [17] I. Pomerantz et al. Hard photodisintegration of a proton pair. *Physics Letters B*, 684(2-3):106–109, 2010.
- [18] I. Pomerantz et al. Two-body hard photodisintegration of ${}^3\text{he} \rightarrow pd$. *To be submitted for publication*.
- [19] Nathan Isgur and C. H. Llewellyn Smith. Perturbative qcd in exclusive processes. *Physics Letters B*, 217(4):535 – 538, 1989.
- [20] Nathan Isgur and C. H. Llewellyn Smith. Asymptotic q^2 for exclusive processes in quantum chromodynamics. *Phys. Rev. Lett.*, 52(13):1080–1083, Mar 1984.
- [21] A. V. Radyushkin. Sum rules and exclusive processes in QCD. *Acta Phys. Polon.*, B15:403–417, 1984.
- [22] Huleihel K. Zhang H. Farrar, G.R. Deuteron form factor. *Physical Review Letters*, 74(5):650–653, 1995. cited By (since 1996) 23.
- [23] Huleihel K. Zhang H. Farrar, G.R. Perturbative qcd predictions for large momentum transfer photoproduction. *Nuclear Physics B*, 349(3):655–674, 1991. cited By (since 1996) 30.
- [24] Dixon L. Brooks, T. Recalculation of proton compton scattering in perturbative qcd. *Physical Review D - Particles, Fields, Gravitation and Cosmology*, 62(11):1–9, 2000. cited By (since 1996) 0.
- [25] K. Wijesooriya et al. Polarization measurements in high-energy deuteron photodisintegration. *Phys. Rev. Lett.*, 86:2975–2979, 2001.
- [26] G. Peter Lepage and Stanley J. Brodsky. Exclusive Processes in Perturbative Quantum Chromodynamics. *Phys. Rev.*, D22:2157, 1980.

- [27] Joseph Polchinski and Matthew J. Strassler. Hard scattering and gauge / string duality. *Phys. Rev. Lett.*, 88:031601, 2002.
- [28] Ronald Gilman and Franz Gross. Electromagnetic structure of the deuteron. *J. Phys.*, G28:R37–R116, 2002.
- [29] S. J. Brodsky et al. Hard photodisintegration of a proton pair in He-3. *Phys. Lett.*, B578:69–77, 2004.
- [30] Stanley J. Brodsky and John R. Hiller. Reduced nuclear amplitudes in quantum chromodynamics. *Phys. Rev.*, C28:475, 1983.
- [31] Hiller J.R. Holt R.J. Carlson, C.E. Relativistic qcd view of the deuteron. *Annual Review of Nuclear and Particle Science*, 47(1):395–428, 1997. cited By (since 1996) 24.
- [32] Andivahis L. Lung A. Stuart L.M. Alster J. Arnold R.G. Chang C.C. Dietrich F.S. Dodge W. Gearhart R. Gomez J. Griffioen K.A. Hicks R.S. Hyde-Wright C.E. Keppel C. Kuhn S.E. Lichtenstadt J. Miskimen R.A. Peterson G.A. Petratos G.G. Rock S.E. Rokni S. Sakumoto W.K. Spengos M. Swartz K. Szalata Z. Tao L.H. Bosted, P.E. Measurements of the electric and magnetic form factors of the proton from $q^2=1.75$ to 8.83 (gev/c)². *Physical Review Letters*, 68(26):3841–3844, 1992. cited By (since 1996) 32.
- [33] A. Nogga, H. Kamada, and Walter Gloeckle. Solution of the Faddeev-Yakubovsky equations using realistic NN and 3N interaction. *Nucl. Phys.*, A689:357–360, 2001.
- [34] J. L. Forest et al. Femtometer Toroidal Structures in Nuclei. *Phys. Rev.*, C54:646–667, 1996.
- [35] V. Yu. Grishina et al. Deuteron photodisintegration within the quark gluon strings model and QCD motivated nonlinear Regge trajectories. *Eur. Phys. J.*, A10:355–364, 2001.
- [36] Leonid L. Frankfurt, Gerald A. Miller, Misak M. Sargsian, and Mark I. Strikman. QCD rescattering and high energy two-body photodisintegration of the deuteron. *Phys. Rev. Lett.*, 84:3045–3048, 2000.
- [37] Misak M. Sargsian. Polarization Observables in Hard Rescattering Mechanism of Deuteron Photodisintegration. *Phys. Lett.*, B587:41–51, 2004.

- [38] MK Carter, PDB Collins, and M. Whalley. Compilation of nucleon-nucleon and nucleon-antinucleon elastic scattering data, Rutheford Lab. preprint. Technical report, RAL-86-002, 1986.
- [39] Polkinghorne J.C. Landshoff, P.V. pp elastic scattering at large momentum transfer. *Physics Letters B*, 44(3):293–295, 1973. cited By (since 1996) 7.
- [40] Bernard Pire and John P. Ralston. Fixed angle elastic scattering and the chromo-coulomb phase shift. *Physics Letters B*, 117(3-4):233–237, 1982.
- [41] P. V. Landshoff. Model for elastic scattering at wide angle. *Phys. Rev. D*, 10(3):1024–1030, Aug 1974.
- [42] De Teramond G.F. Brodsky, S.J. Spin correlations, qed color transparency, and heavy-quark thresholds in proton-proton scattering. *Physical Review Letters*, 60(19):1924–1927, 1988. cited By (since 1996) 57.
- [43] Brodsky S.J. Blankenbecler R. Sivers, D. Large transverse momentum processes. *Physics Reports*, 23(1):1–121, 1976. cited By (since 1996) 36.
- [44] Adams G.S. Audit G. Baghaei H. Caracappa A. Clayton W.B. D’Angelo A. Duval M.A. Giordano G. Hoblit S. Kistner O.C. Laget J.M. Lindgren R. Matone-G. Miceli L. Mize W.K. Moinester M. Ruth C. Sandorfi A. Schaerf C. Sealock R.M. Smith L.C. Stoler P. Teng P.K. Thorn C.E. Thornton S.T. Vaziri K. Whisnant C.S. Winhold E.J. Tedeschi, D.J. Exclusive photodisintegration of he3 with polarized photons. *Physical Review Letters*, 73(3):408–411, 1994. cited By (since 1996) 18.
- [45] C.W. Leemann, D.R. Douglas, and G.A. Krafft. The continuous electron beam accelerator facility: CEBAF at the Jefferson Laboratory. *Annual Review of Nuclear and Particle Science*, 51(1):413–450, 2001.
- [46] J. Alcorn et al. Basic Instrumentation for Hall A at Jefferson Lab. *Nucl. Instrum. Meth.*, A522:294–346, 2004.
- [47] X. Zheng. Ph.d thesis, massachusetts institute of technology, (2002);
- [48] A. Saha. <http://http://www.jlab.org/~saha/beamline/>.
- [49] M. Jones, report on bcms callibration at hall a (unpublished). <http://http://www.jlab.org/~jones/e91011/>.
- [50] R. Gilman, hall a bremsstrahlung radiator (unpublished). <http://www.jlab.org/~gilman/gammap99/hallarad2001.html>.

- [51] L. Zhu. Ph.d thesis, massachusetts institute of technology, (2004);
- [52] Hall a high resolution spectrometers general characteristics. http://halloweb.jlab.org/equipment/high_resol.html.
- [53] Coda, jefferson lab data acquisition group. <http://coda.jlab.org/>.
- [54] Root/c++ analyzer for hall a. <http://halloweb.jlab.org/podd/>.
- [55] R. Brun and F. Rademakers. ROOT—An object oriented data analysis framework. *Nuclear Instruments and Methods in Physics Research Section A: Accelerators, Spectrometers, Detectors and Associated Equipment*, 389(1-2):81–86, 1997.
- [56] J. L. Matthews and R. O. Owens. Accurate formulae for the calculation of high energy electron bremsstrahlung spectra. *Nucl. Instrum. Meth.*, 111:157–168, 1973.
- [57] P. E. Ulmer. Mceep: Monte carlo for electro-nuclear coincidence experiments. 1991. CEBAF-TN-91-101.
- [58] L. Zhu. Exclusive Photoproduction of Charged Pions in Hydrogen and Deuterium from 1 to 6 GeV. Technical report, Thomas Jefferson National Accelerator Facility, Newport News, VA, 2004.
- [59] R. Schiavilla, Robert B. Wiringa, Steven C. Pieper, and J. Carlson. Tensor Forces and the Ground-State Structure of Nuclei. *Phys. Rev. Lett.*, 98:132501, 2007.
- [60] D. G. Mekkins. Ph.d thesis, college of william and mary, (1998);
- [61] E. Schulte. High Energy Measurement of the Deuteron Photodisintegration Differential Cross Section. Technical report, Thomas Jefferson National Accelerator Facility, Newport News, VA (US), 2002.
- [62] S. Niccolai et al. Complete measurement of three-body photodisintegration of He-3 for photon energies between 0.35-GeV and 1.55-GeV. *Phys. Rev.*, C70:064003, 2004.
- [63] RM Gibbons and DI Nathan. *Technical report AFML-TR-67-173, AFSC, Wright-Patterson Air Force Base, Ohio*, October, 1967.
- [64] B. A. Mecking et al. The CEBAF Large Acceptance Spectrometer (CLAS). *Nucl. Instrum. Meth.*, A503:513–553, 2003.

- [65] S. Strauch. private communication.
- [66] Misak M. Sargsian and Carlos Granados. Hard Break-Up of Two-Nucleons from the ^3He Nucleus. *Phys. Rev.*, C80:014612, 2009.
- [67] G. Audit et al. The Two and three-body photodisintegration of ^3He . Presented at 6th Workshop on Perspectives in Nuclear Physics at Intermediate Energies, Trieste, Italy, 3-7 May 1993.
- [68] JM Laget. Many body effects in deep inelastic electron scattering on ^3He . *Physics Letters*, B151(5-6):325–329, 1985.
- [69] J. M. Laget. Many body effects in deep inelastic electron scattering on ^3He . *Phys. Lett.*, B151:325, 1985.
- [70] H. J. Besch, F. Krautschneider, K. P. Sternemann, and W. Vollrath. Photo-production of charged pions from deuterium at gamma energies from 900-MeV to 1800-MeV and pion angles between 65-degrees and 125-degrees. *Z. Phys.*, C16:1–6, 1982.
- [71] P. Benz et al. Measurement of the reaction $\gamma d \rightarrow \pi^- p p$, and determination of cross-sections for the reaction $\gamma n \rightarrow \pi^- p$, at photon energies between 0.2-GeV and 2.0- GeV. *Nucl. Phys.*, B65:158–209, 1973.
- [72] L. Y. Zhu et al. Cross section measurements of charged pion photoproduction in hydrogen and deuterium from 1.1-GeV to 5.5-GeV. *Phys. Rev.*, C71:044603, 2005.
- [73] J. M. Laget. private communication.
- [74] V. Yu. Grishina et al. Polarization observables in high-energy deuteron photodisintegration within the quark gluon strings model. *Eur. Phys. J.*, A18:207–209, 2003.
- [75] M. M. Sargsian, T. V. Abrahamyan, M. I. Strikman, and L. L. Frankfurt. Exclusive electro-disintegration of ^3He at high Q^{*2} . II: Decay function formalism. *Phys. Rev.*, C71:044615, 2005.
- [76] M. Alvioli, C. Ciofi degli Atti, and H. Morita. Proton-neutron and proton-proton correlations in medium- weight nuclei and the role of the tensor force. *Phys. Rev. Lett.*, 100:162503, 2008.

- [77] E. Piasetzky, M. Sargsian, L. Frankfurt, M. Strikman, and J. W. Watson. Evidence for the Strong Dominance of Proton-Neutron Correlations in Nuclei. *Phys. Rev. Lett.*, 97:162504, 2006.
- [78] R. Shneur et al. Investigation of Proton-Proton Short-Range Correlations via the $^{12}\text{C}(e,e'pp)$ Reaction. *Phys. Rev. Lett.*, 99:072501, 2007.
- [79] R. Subedi et al. Probing Cold Dense Nuclear Matter. *Science*, 320:1476–1478, 2008.
- [80] I. Pomerantz et. al. Jefferson lab, proposal no. 12-11-104;.
- [81] D. I. Sober, Hall Crannell, Alberto Longhi, S. K. Matthews, J. T. O'Brien, B. L. Berman, W. J. Briscoe, Philip L. Cole, J. P. Connelly, W. R. Dodge, L. Y. Murphy, S. A. Philips, M. K. Dugger, D. Lawrence, B. G. Ritchie, E. S. Smith, James M. Lambert, E. Anciant, G. Audit, T. Auger, C. Marchand, M. Klusman, J. Napolitano, M. A. Khandaker, C. W. Salgado, and A. J. Sarty. The bremsstrahlung tagged photon beam in hall b at jlab. *Nuclear Instruments and Methods in Physics Research Section A: Accelerators, Spectrometers, Detectors and Associated Equipment*, 440(2):263–284, 2000.
- [82] Y. Ilieva. Two-body photodisintegration of ^3He . 2011. CLAS Note.
- [83] CLAS. Gsim. 1997. CLAS Simulation Software.
- [84] J. Ball and E. Pasyuk. Photon flux determination through sampling of "out-of-time" hits with the hall b photon tagger. 2005. CLAS Note 2005-002.
- [85] Y. Ilieva et al. Evidence for a backward peak in the $\gamma d \rightarrow \pi^0 d$ cross section near the η threshold. *Eur. Phys. J.*, A43:261–267, 2010.
- [86] R. Nasseripour et al. Photodisintegration of ^4He into p+t. *Phys. Rev.*, C80:044603–044603–11, 2009.
- [87] V. Isbert et al. Two-body photodisintegration of He-3 between 200-MeV and 800-MeV. *Nucl. Phys.*, A578:525–541, 1994.
- [88] M. Sargsian. private communication.
- [89] Stanley J. Brodsky and Guy F. de Téramond. Light-front dynamics and ads/qcd correspondence: The pion form factor in the space- and time-like regions. *Phys. Rev.*, D77(5):056007, 2008.